Exploring Nuclear Magnetic Resonance at the Highest Pressures
-
Closing the Pseudogap under Pressure in a High Temperature Superconductor

Von der Fakultät für Physik und Geowissenschaften
der Universität Leipzig
genehmigte

DISSERTATION

zur Erlangung des akademischen Grades

doctor rerum naturalium

Dr. rer. nat.

vorgelegt von

Dipl.-Phys. Thomas Meißner

geboren am 3. April 1983 in Rostock

Gutachter: Prof. Dr. Jürgen Haase, Universität Leipzig
Prof. Dr. Hugo Keller, Universität Zürich

Tag der Verleihung 13. Mai 2013

Contents

List of Abbreviations

BeCu	beryllium copper
DAC	diamond anvil cell
DOS	density of states
EFG	electric field gradient
fcc	face-centered-cubic
FID	free induction decay
FS	Fermi surface
FT	Fourier transformation
FWHM	full width at half maximum
GAC	gem anvil cell
hf	hyperfine
LDA	local density approximation
MAC	moissanite anvil cell
NMR	nuclear magnetic resonance
NQR	nuclear quadrupole resonance
rf	radio frequency
RT	room temperature
SNR	signal-to-noise ratio
Y1236:x	$YBa_2Cu_3O_{6+x}$
Y1248	$YBa_2Cu_4O_8$

1 Introduction

The physical properties of materials are fundamentally influenced by temperature, applied magnetic fields and pressure. In particular pressure is capable of modifying the ground state of matter [1].

To gain new insight into materials, it is therefore of considerable interest to carry out experiments under varied pressure conditions. In the case of condensed matter systems like high temperature superconductors or simple metals, significant changes occur at relatively high pressures on the order of 10 kbar (10000 times the atmospheric pressure) or higher. Such extreme conditions are often only achievable in so called gem anvil cells that squeeze a tiny sample, confined by a metallic gasket, between the tips of two extremely hard gem anvils.

Nuclear magnetic resonance (NMR) is a powerful analytical tool that is widely used to probe the electronic and chemical properties of materials on an atomic scale by observing transitions between nuclear spin states [2]. Over the past 25 years a variety of experimental designs have been developed for the observation of NMR in gem anvil cells [3–7]. However, due to their insufficient sensitivity they have been scarcely used in the investigation of high pressure effects in condensed matter systems.

In the present work, a novel approach to high sensitivity NMR in gem anvil cells is pursued which extends earlier work during my diploma thesis [8]. By placing a small microcoil as the detection coil in the high pressure region of a gem anvil cell, a tremendous increase of sensitivity is achieved. Using this setup, NMR experiments are successfully carried out up to 101 kbar, the second highest pressure at which NMR has been observed thus far.

One set of experiments presented here explores the effect of pressure on the electronic density of states in the metal aluminum. In these measurements a decrease of the density of states under pressure is revealed that is inconsistent with a free electron behavior. Based on numerical calculations, a pressure induced Lifshitz-transition is identified as the origin of this decrease.

In the second set of experiments presented, the effect of pressure on the enigmatic pseudogap in the high temperature superconductor $YBa_2Cu_4O_8$ is investigated. This peculiar electronic gap was discovered early on in the research on the superconducting cuprates [9, 10] and has been extensively studied at ambient and lower pressure in particular via NMR. Yet, its origin and relation to superconductivity remain unclear. Due to a prior lack of suitable electronic probes, little was known about its response to high pressure [11]. In the new experiments presented here, the pressure range of previous comparable experiments [12–14] is significantly extended and evidence for the closing of the pseudogap in $YBa_2Cu_4O_8$ at high pressure is found.

2 Basics

In this chapter some essential information on nuclear magnetic resonance (NMR), the design of an NMR probehead and the generation of high pressure in gem anvil cells will be presented. At the end of the chapter, the state of the art in gem anvil cell NMR will be reviewed.

2.1 Nuclear magnetic resonance

This section covers the basic principles of NMR relevant for the experiments performed during this thesis. Unless stated otherwise, the information presented here is based on the NMR textbooks by Abragam [15] and Slichter [2].

Many atomic nuclei have a non-zero spin angular momentum $\boldsymbol{I}$ in their ground state. In quantum mechanics $\boldsymbol{I}$ is treated as an operator. Its components $I_{x,y,z}$ do not commute among one another but it is possible to orthogonalize one component, e.g. I_z with the operator $\boldsymbol{I}^2$. Hence a common set of eigenvectors $|Im\rangle$ exists and the eigenvalues are defined by

$$\begin{aligned} \boldsymbol{I}^2|Im\rangle &= I(I+1)|Im\rangle & (2.1)\\ I_z|Im\rangle &= m|Im\rangle & (2.2) \end{aligned}$$

where I takes values of $I = 0, 1/2, 1, 3/2, \ldots$ and $m = -I, -I+1, \ldots, I-1, I$. Associated with $\boldsymbol{I}$ is a magnetic moment

$$\boldsymbol{\mu} = \hbar\gamma\boldsymbol{I} \qquad (2.3)$$

with γ denoting the gyromagnetic ratio that is specific for each type of nucleus. If a nuclear magnetic moment $\boldsymbol{\mu}$ is exposed to an external magnetic field $\boldsymbol{B}$ it will interact with it due to the Zeeman interaction, its Hamiltonian $\mathscr{H}_Z$ given by

$$\begin{aligned} \mathscr{H}_Z &= -\boldsymbol{\mu}.\boldsymbol{B} \\ &= -\hbar\gamma\boldsymbol{I}.\boldsymbol{B}. & (2.4) \end{aligned}$$

It is conventional to assume that a static magnetic field $\boldsymbol{B} = (0, 0, B_0)$ is applied along the z-direction. In this case the Hamiltonian of eqn. (2.4) can be simplified to $\mathscr{H}_Z = -\hbar\gamma B_0 I_z$ and its eigenvalues are then

$$E_m = -m\hbar\gamma B_0. \qquad (2.5)$$

The degeneracy of the ground state is broken by applying an external static magnetic field B_0 and the energy difference between adjacent levels is $\Delta E = \hbar\gamma B_0$. A Boltzmann distribution describes the population probabilities of the energy levels, i.e. $p_m \propto \exp\{-E_m/k_BT\}$. Thus an assembly of spins exposed to a static magnetic field B_0 will, after a characteristic time, populate the energy levels according to

$$\frac{p_{m+1}}{p_m} = \exp\left\{\frac{\gamma\hbar B_0}{k_BT}\right\}. \tag{2.6}$$

As a result, a net magnetization $\langle M_z\rangle$ along the axis of B_0 establishes due to the population difference in thermal equilibrium. In the high temperature limit, usually realized since $\gamma\hbar B_0/k_BT$ is small[a], $\langle M_z\rangle$ is given by

$$\langle M_z\rangle = \frac{N}{V}\frac{\gamma^2\hbar^2 I(I+1)}{3k_BT}B_0, \tag{2.7}$$

where N/V denotes the spin density. It should be noted that $\langle M_z\rangle$ from nuclear spins is very small, as the ratio of population of the different levels p_{m+1}/p_m is on the order of unity[b]. This is the origin of the intrinsic low sensitivity in NMR experiments.

The $\pi/2$ and π-pulse

In pulsed NMR experiments one takes advantage of the fact that the equilibrium magnetization $\langle M_z\rangle$ can be manipulated by a high frequency magnetic field B_{rf}

$$B_{\mathrm{rf}} = 2B_1\cos\omega t \tag{2.8}$$

perpendicular to B_0, if the resonance condition

$$\omega = 2\pi\nu_L = \gamma B_0 \tag{2.9}$$

is met. The resonance frequency ν_L is called Larmor frequency and is typically on the order of $10\ldots1000$ MHz and therefore in the radio-frequency (rf) range. In most cases, B_{rf} is generated by a rf-coil.

The amplitude of $2B_1$ in eqn. (2.8) originates from the fact that the linearly polarized B_{rf}-field can be decomposed into two components with magnitude B_1 that rotate clockwise and counter-clockwise at $\pm\omega$ in the xy-plane, respectively. One of these components however is irrelevant for the analysis here and is generally neglected.

Depending on the duration τ of the perturbation, the initial magnetization $\langle M_z\rangle$ is flipped by an angle $\alpha = \gamma B_1\tau$ around an axis of the coordinate system rotating at ω around the direction

[a] For example for aluminum nuclei at room temperature (300 K) in a magnetic field of $B_0 = 11.7$ T, $\gamma\hbar B_0/k_BT = 2.085\times10^{-5}$.

[b] For the aluminum example ($B_0 = 11.7$ T, $T = 300$ K) $p_{m+1}/p_m \approx 1 + 1/50000$. Therefore for every $5\times10^4+1$ spins in the $m = 1/2$ state there are 5×10^4 spins in the $m = -1/2$ state to almost completely cancel out with, leaving only that 1 extra spin to contribute to $\langle M_z\rangle$.

of B_0.

Of particular interest for experiments are the durations $\tau_{\pi/2}$ and τ_π for the so-called $\pi/2$-pulse and π-pulse. They are defined through the conditions $\gamma B_1 \tau_{\pi/2} = \pi/2$ and $\gamma B_1 \tau_\pi = \pi$. Following a $\pi/2$-pulse the magnetization perpendicular to B_0 is maximized as the initial magnetization $\langle M_z(0)\rangle$ is turned completely into the laboratory xy-plane. It then precesses at ω around B_0 and can be detected by Faraday induction in the same rf-coil. After a duration of τ_π on the other hand the initial magnetization is inverted, i.e. $\langle M_z(\tau_\pi)\rangle = -\langle M_z(0)\rangle$. After such perturbations, the spin system will relax back to its equilibrium state given by eqn. (2.7) by processes described in sec. 2.1.2.

2.1.1 Perturbation of the Hamiltonian $\mathscr{H}_Z$

The general interest in NMR, especially in condensed matter physics, is based on the fact that the nuclear spin does not only interact with the external magnetic field but also with other nuclei and electrons in its vicinity. These interactions are in most cases small compared to the Zeeman Hamiltonian and can therefore be treated by perturbation theory. As they affect the energy of the spin system, these interactions can be detected by a change of the resonance frequency ν_0 in comparison to the Larmor-frequency ν_L and/or by their influence on relaxation processes. Below, the relevant interactions will be briefly mentioned.

Dipolar coupling

Two nuclear spins interact with each other due to the dipolar coupling of their magnetic moments $\boldsymbol{\mu}_1 = \gamma_1 \hbar \boldsymbol{I}_1$ and $\boldsymbol{\mu}_2 = \gamma_2 \hbar \boldsymbol{I}_2$. With $\boldsymbol{r}$ as their displacement, the interaction Hamiltonian is given by

$$\mathscr{H}_D = \gamma_1 \gamma_2 \hbar^2 \boldsymbol{I}_1 . \left[\frac{\boldsymbol{I}_2}{r^3} - 3 \frac{\boldsymbol{r}\,(\boldsymbol{I}_2 . \boldsymbol{r})}{r^5} \right] . \tag{2.10}$$

In absence of rapid motion of the magnetic moments relative to one another, which is the case in the rigid lattice of a solid, the dipolar coupling causes a B_0-independent broadening of the resonance frequency which can be quite complex even in simple systems [16].

Hyperfine coupling

The different magnetic interactions of the nuclear spin with the surrounding electrons are comprehensively called hyperfine interactions. Taking into account their different contributions, the hyperfine interaction Hamiltonian is given by

$$\mathscr{H}_{HF} = 2\gamma \hbar \mu_B \boldsymbol{I} . \left[\frac{\boldsymbol{l}}{r^3} - \frac{\boldsymbol{s}}{r^3} + 3 \frac{\boldsymbol{r}\,(\boldsymbol{s} . \boldsymbol{r})}{r^5} + \frac{8}{3} \pi \boldsymbol{s} \delta(\boldsymbol{r}) \right] , \tag{2.11}$$

where μ_B denotes the Bohr magneton and $\boldsymbol{l}$ and $\boldsymbol{s}$ are the orbital and spin angular momentum operators of the electron. Eqn. (2.11) contains three distinct interaction terms, namely an orbital

interaction (1st term), a dipolar interaction similar to eqn. (2.10) (2nd and 3rd term) and a so-called s- or Fermi-contact interaction (4th term). These interactions can typically be detected by a shift in resonance frequency ν_0 as they affect the local magnetic field at the nucleus. In general, the contribution of the different interactions to the change in local field and therefore the shift of ν_0 is of the form

$$K = \frac{\Delta B}{B_0} = \frac{\nu_0 - \nu_\mathrm{L}}{\nu_\mathrm{L}} = A_\mathrm{hf}\chi, \tag{2.12}$$

where χ is a susceptibility that is attributable to the different terms in eqn. (2.11) and A_hf is called a hyperfine coupling constant.

Quadrupole coupling

Due to the fact that atomic nuclei have finite dimensions, their electrical charge cannot be described by a point charge. Nuclei with spin $I \geq 1$ posses a quadrupole moment Q and will interact with an electrical field gradient (EFG) eq caused by electrons in the vicinity of the nucleus. Taking X, Y, Z to denote the principle axes of the tensor V_{ij} describing the EFG[c], this quadrupole interaction Hamiltonian is given by

$$\mathscr{H}_Q = \frac{e^2qQ}{4I(2I-1)}\left[3I_Z^2 - \boldsymbol{I}^2 + \frac{1}{2}\eta(I_+^2 + I_-^2)\right], \tag{2.13}$$

where $\eta = (V_{XX} - V_{YY})/V_{ZZ}$ is the asymmetry parameter which can take values of $0 \ldots 1$ and $I_\pm = I_x \pm iI_y$. It should be noted that the quadrupole interaction can be quite large compared to the Zeeman interaction[d]. The following discussion will restrict itself to the case of $\mathscr{H}_Q \ll \mathscr{H}_Z$ and cylindrical symmetry of the EFG ($\eta = 0$). Furthermore only half-integer spins will be considered as the observed nuclei ^{17}O, ^{27}Al and ^{63,65}Cu have spins of 5/2, 5/2 and 3/2 respectively.

If θ denotes the angle between B_0 and the EFG and ν_Q is

$$\nu_Q = \frac{3e^2qQ}{h2I(2I-1)}, \tag{2.14}$$

the frequencies of the transitions $(m-1) \leftrightarrow m$ are shifted in 1st order by

$$\delta\nu_m^{(1)} = -\nu_Q\left(m - \frac{1}{2}\right)\frac{3\cos^2\theta - 1}{2}. \tag{2.15}$$

From eqn. (2.15) it is clear that in first order the central transition $-1/2 \leftrightarrow 1/2$ is not affected by the quadrupolar interaction. The frequencies of the other transitions $(m-1) \leftrightarrow m$ however are shifted, which manifests itself in the presence of additional satellite lines in an NMR spectrum, see fig. 2.1 for illustration. The intensities of the transitions are proportional to $|\langle m|I_x|m-1\rangle|^2$

[c] It is assumed that the coordinate system describing the EFG tensor V_{ij} is chosen, so that $|V_{ZZ}| \geq |V_{YY}| \geq |V_{XX}|$.
[d] This fact is utilized in the observation of nuclear quadrupole resonance (NQR).

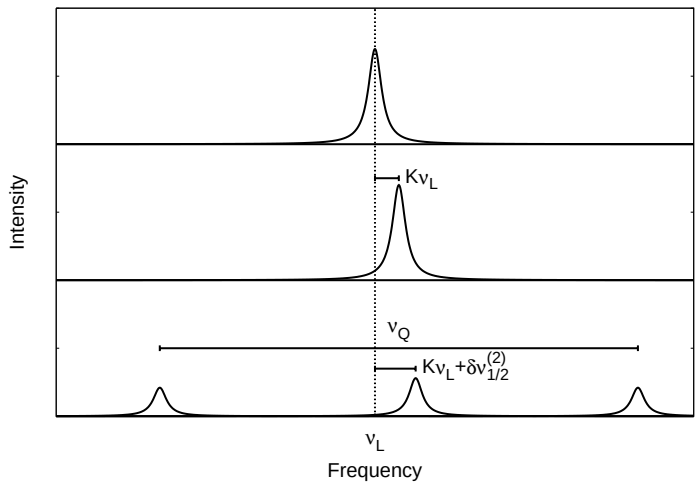

Figure 2.1: Illustration of the effects of the different interactions. (Top) The Zeeman interaction causes a resonance at a frequency ν_L that is broadened by the dipolar interaction of nuclei among each other. (Middle) An additional hyperfine interaction of the nuclear spins with electrons in their environment gives rise to a shift of the resonance frequency by $K\nu_L$. (Bottom) The effect of quadrupole interactions for the case of a spin-3/2 system assuming B_0 is applied perpendicular to the EFG: In first order perturbation, the single transition line is split into three lines with intensities $3:4:3$. The satellite transitions $-3/2 \leftrightarrow -1/2$ and $1/2 \leftrightarrow 3/2$ are observable at $(1+K)\nu_L \pm \nu_Q/2$. In second order, the central transition $-1/2 \leftrightarrow 1/2$ is shifted by $\delta\nu^{(2)}_{1/2} \propto \nu_Q^2/\nu_L$ while the satellites are unaffected.

and hence have the ratios $3{:}4{:}3$ for spin $3/2$ and $5{:}8{:}9{:}8{:}5$ for spin $5/2$.

For 2nd order, only the change of the central transition $-1/2 \leftrightarrow 1/2$ shall be considered here as the $-3/2 \leftrightarrow -1/2$ and $1/2 \leftrightarrow 3/2$ transitions are unaffected and other transitions are of minor interest. The second order frequency shift of the central transition is given by

$$\delta\nu^{(2)}_{\frac{1}{2}} = -\frac{\nu_Q^2}{16\nu_L}\left[I(I+1) - \frac{3}{4}\right]\sin^2\theta\left(9\cos^2\theta - 1\right). \tag{2.16}$$

It is inversely proportional to ν_L and therefore can be determined by field-dependent measurements even if ν_Q and/or the orientation of the EFG is unknown.

Fig. 2.1 illustrates the effects of the different interactions on the energy levels of the spin system as observed experimentally in NMR by the resonance frequency ν_0.

2.1.2 NMR pulse sequences and relaxation processes

Assuming the equilibrium magnetization $\langle M_z(0)\rangle$ is established, the simplest NMR experiment is performed by applying a $\pi/2$-pulse. The equilibrium magnetization $\langle M_z(0)\rangle$ will then precess in the xy-plane of the laboratory frame and induce a signal voltage in the rf-coil. However, with time the magnetization both dephases in the xy-plane, e.g. due to a distribution of the resonance frequencies, and relaxes back to its equilibrium value in the z-direction. Consequently,

the signal in the rf-coil decays and it is therefore called free induction decay (FID).

The return of the z-component of the magnetization to its equilibrium value is described by the characteristic time constant T_1, called spin-lattice relaxation time. Yet, the detectable signal in the coil often decays on a much shorter time scale due to the dephasing of the xy-component of the magnetization. This process is characterized by the spin-spin relaxation time T_2. Both effects may be different in nature and yield information on the effective interactions.

T_2-relaxation

T_2-relaxation processes are usually not related to an energy exchange with a lattice and can therefore be faster than T_1-processes. For example, a dephasing of the xy-magnetization occurs because of the dipolar-interaction of the nuclei among each other. In the case of a rigid lattice, it was shown by van Vleck [17] that the FID at short times then has a Gaussian shape

$$I(t) = I_0 \exp\left\{-\frac{t^2}{2T_2^2}\right\}. \tag{2.17}$$

However, it is worth mentioning that the long time behavior of the FID may be very different for this dipolar interaction induced signal decay [16].

A large distribution of resonance frequencies, e.g. due to anisotropy of the hyperfine coupling constant A_{hf}, also affects the dephasing of the xy-magnetization and may cause the FID following a $\pi/2$-pulse to decay too quickly to be detectable because of the inherent dead-time of an NMR-spectrometer. In this case, the signal can often be refocussed with the spin-echo sequence $\pi/2 - \tau - \pi$. The echo will then refocus at the time 2τ after the initial $\pi/2$-pulse. It should be noted though, that a dipolar decay cannot be refocussed with this kind of echo sequence.

T_1-relaxation

T_1-relaxation processes on the other hand are associated with an energy transfer to a lattice. This is due to the fact that an energy transfer between the nuclear spins and a reservoir, commonly referred to as the "lattice", is required in order to align the spins along B_0 initially. The same processes are responsible for the relaxation back to the equilibrium state following a perturbation by rf-pulses.

Generally, multiple interactions contribute to the spin-lattice relaxation. However, in the systems of interest the spin-lattice relaxation is dominated by the spin part of the hyperfine interaction. In that case, the relaxation rate is given by [18]

$$\frac{1}{T_{1,\alpha}} = \frac{\gamma k_B T}{\mu_B^2} \sum_{\boldsymbol{q}} \sum_{\xi} A_{\xi}\left(\boldsymbol{q}\right)^2 \frac{\chi''\left(\boldsymbol{q}, \omega_0\right)}{\omega_0}, \tag{2.18}$$

where α indicates the direction of B_0 with respect to the crystal axis, ξ the directions normal to it and summations are performed over $\boldsymbol{q}$-space and the two directions of ξ. In eqn. (2.18),

$A_\xi(\boldsymbol{q})$ denotes the $\boldsymbol{q}$- and ξ-dependent hyperfine coupling constant, $\chi''(\boldsymbol{q},\omega_0)=\mathrm{Im}\{\chi(\boldsymbol{q},\omega_0)\}$ the isotropic, $\boldsymbol{q}$-dependent dynamic spin susceptibility and $\omega_0 = 2\pi\nu_0$ the NMR observation frequency.

Experimentally, T_1 can be determined using the inversion recovery sequence $\pi-t-\pi/2$ or the inversion recovery echo sequence $\pi-t-\pi/2-\tau-\pi$ in the case of a quickly decaying FID. The initial π-pulse inverts the magnetization and the system is then left to relax for the time t before the signal is recorded with the $\pi/2$-pulse or echo-sequence.

The intensity of the signal then depends on wether all transitions are excited by the rf-pulses or not. In the case of non-selective excitation, i.e. if all transitions are excited, the intensity is given by

$$I(t) = I_0\left[1-\Gamma\exp\left\{-\frac{t}{T_1}\right\}\right], \tag{2.19}$$

where I_0 denotes the equilibrium intensity at $t \gg T_1$ and Γ represents the quality of inversion and should be close to 2.

2.2 NMR-signal detection with a resonance circuit

So far, the essential laboratory equipment for performing NMR experiments, i.e. a magnet to supply the static magnetic field B_0, an NMR spectrometer to generate defined rf-pulses and record small signal voltages and the NMR probehead have not been described. While the magnet and spectrometer are crucial components, they shall be treated as black boxes here. In this section however, the generic design of an NMR probehead will be described and its relevant properties discussed. Basically, the probehead is a resonant LC-circuit with the coil placed in the center of the static magnetic field produced by the magnet. For experiments in high pressure cells, such as the gem anvil cell, it is a non-trivial task to construct this LC-circuit which was an important task of my work.

2.2.1 Solenoidal coil

The centerpiece of any NMR probehead is a radio frequency coil containing the sample. It is used to generate the perturbation $B_{\mathrm{rf}}=2B_1\cos\omega t$, necessary to manipulate the equilibrium magnetization $\langle M_z(0)\rangle$, and to detect the precession of the magnetization in the xy-plane. Furthermore, while the pre-amplifier of the spectrometer also plays an important role, the sensitivity in NMR experiments depends predominantly on the rf-coil design. It should be mentioned here that the rf-coil has to be aligned so that B_{rf} is perpendicular to B_0 in order to be able to perturbate the spin system and detect the signal with high efficiency.

In the experiments to be discussed, solenoidal microcoils were used as they are simple to prepare, offer a good homogeneity of B_{rf} and superior sensitivity for volume limited samples [19, 20]. The relevant properties of these solenoids will be characterized below.

Inductance

The inductance L of a coil relates the current flow i through it to the energy stored in the resulting magnetic field B_{rf}; its value affects the resonance frequency and the quality factor Q (eqn. (2.29)) of the resonant circuit. For a finite empty solenoid, L is given to a good approximation by [21]

$$L\,[\mathrm{nH}] = \frac{21.8N^2D}{1 + 2.2\left(\frac{l}{D}\right)} \tag{2.20}$$

where N, D [cm] and l [cm] denote the number of turns, the diameter and the length of the coil respectively. If the coil is filled with a sample, its inductance is modified due to the magnetic susceptibility χ_{m} of the material, i.e. $L_\eta = L(1+\eta\chi_{\mathrm{m}})$, where η denotes the filling factor (ratio of filled coil volume to total coil volume). In the case of non magnetic materials, i.e. the typical NMR sample, $\chi_{\mathrm{m}} \approx 0$. However superconducting materials display perfect diamagnetism, i.e. χ_{m} = -1, below their critical temperature. This can be used to detect the superconducting transition of materials by changes in L as discussed in sec. 3.3.

Sensitivity

Because of Faraday induction

$$U_{\mathrm{ind}} = -\frac{d\Phi}{dt} \tag{2.21}$$

with $\Phi = \int \boldsymbol{B}.d\boldsymbol{A}$, a magnetization precessing in the xy-plane, such as that produced by the rotating spins after a $\pi/2$-pulse, will induce a voltage in a coil that can be detected at its terminals. In general, thermal noise generated by the coil and the sample will overlay the signal voltage however. Therefore the quantity defining the sensitivity of the rf-coil is the signal-to-noise ratio (SNR)

$$\mathrm{SNR} = \frac{U_{\mathrm{ind}}}{U_{\mathrm{n}}}. \tag{2.22}$$

The noise voltage U_{n} is given by $U_{\mathrm{n}} = \sqrt{4k_BTr_n\Delta f}$ [21], where r_n is used to represent the generic combined losses and the noise is measured over a defined spectral bandwidth Δf. Experimentally, it can be determined by analyzing a recorded FID. Assuming sufficient signal, the induced voltage U_{ind} can be estimated from the amplitude of the signal following the $\pi/2$-pulse directly. U_{n} on the other hand can be determined from the root-mean-square value of the signal at times much longer than T_2 as the fluctuations at long times are caused by thermal noise only.

Hoult and Richards [22] showed, based on the principle of reciprocity, that the SNR following a $\pi/2$-pulse is given by

$$\mathrm{SNR} = \frac{K(B_1/i)V_s\omega_0\langle M_z\rangle}{\sqrt{8k_BTr_n\Delta f}}, \tag{2.23}$$

where V_s denotes the sample volume and K is a scaling constant to account for inhomogeneities of B_1. The factor (B_1/i) is the effective field over the sample volume produced by a unit current flowing through the coil and is given for a solenoid ($N \gg 1$) by [22]

$$\frac{B_1}{i} = \frac{\mu_0 N}{D\sqrt{1+(l/D)^2}}, \tag{2.24}$$

where l and D are the length and diameter of the coil. Eqn. (2.24) in conjunction with eqn. (2.23) already indicates that smaller coils may be advantageous in the case of volume limited samples.

In the case of solenoidal microcoils of fixed coil geometry, it was demonstrated that sensitivity per unit volume increases with decreasing coil diameter with a factor between $1/\sqrt{D}$ and $1/D$ depending on the ratio of the coil wire diameter and skin depth at the operation frequency [19]. Thus, in terms of sensitivity, one should use the smallest rf-coil possible that can actually contain the sample, in the case of size limited samples. This on the other hand implies a filling factor of the coil of $\eta \approx 1$.

It is however necessary to consider the potential sources of noise. In the case of microcoils, it is predominantly the resistance r of the coil wire whose dc-value is given by (assuming a circular cross section)

$$r = \frac{4\rho\ l_w}{\pi d^2}, \tag{2.25}$$

where ρ is the specific resistivity of the wire material and l_w and d denote the length and diameter of the wire. Decreasing the coil dimension eventually leads to an increase of the coil resistance, and hence noise, as the wire diameter has to be reduced at some point. Furthermore it is pointed out that the legs of the microcoil cannot be arbitrarily downscaled as they must have a minimum length in order to be able to electrically contact the microcoil. Their contribution to the coil resistance therefore becomes increasingly important if the microcoil is very small.

For phase sensitive signal detection, the SNR can be further improved in an experiment by accumulation of the signal. Sensitivity then increases with the square root of the number of accumulations[e]. Nonetheless, it is necessary to wait about $3 \ldots 5 \times T_1$ in order to ensure recovering of the equilibrium magnetization $\langle M_z(0) \rangle$. As an increase in the number of accumulations by a factor of 100 improves the SNR only by a factor 10, time quickly becomes the limiting factor.

Duration of the $\pi/2$-pulse

In sec. 2.1 the $\pi/2$- and π-pulses have already been introduced. The flip angle of the magnetization, given by $\alpha = \gamma B_1 \tau$, for a given nucleus depends only on the amplitude of B_1 produced by the coil and the duration of the rf-pulse τ. One therefore expects to be able to predict $\tau_{\pi/2}$ and τ_π based on knowledge of the coil parameters. It can be shown in fact that (see app. 9.2), under

[e] The signal voltage increases with the number of accumulations while the thermal noise only increases with square root of the number of accumulations.

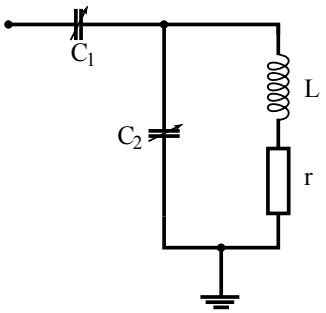

Figure 2.2: Circuit diagram of a capacitively coupled resonant circuit, containing a coil and two capacitors, commonly used in NMR experiments. A coil of inductance L and resistance r is used to manipulate the magnetization of the sample (inside the coil) and detect the NMR signal. The two variable capacitor C_1 and C_2, are used to match (C_2) the resonant circuit to the 50 Ω of the NMR-spectrometer and tune (C_1) the resonance frequency of the circuit.

the assumption that all the energy of the pulse is stored in the magnetic field of the rf-coil of volume V_c, $\tau_{\pi/2}$ is given by

$$\tau_{\pi/2} = \sqrt{\frac{\pi^2 r V_\mathrm{c}}{2\mu_0\gamma^2 L P}}, \tag{2.26}$$

where γ denotes the gyromagnetic ratio of the nucleus investigated and P is the power of the rf-pulse. For a given coil, the parameters r, V_c and L are fixed. It is clear that the flip angle α can be varied changing τ (fixed P) or, from eqn. (2.26), by adjusting P (fixed τ). Varying P has the benefit that the spectral excitation width is kept constant[f]. One should keep in mind however that any additional source of inductance stores energy in its magnetic field and $\tau_{\pi/2}$ therefore usually is somewhat longer.

2.2.2 Resonant circuit

By integrating the rf-coil into a capacitively coupled resonance circuit, a circuit commonly used in NMR experiments and shown in fig. 2.2, it can be matched to the input impedance of 50 Ω of the NMR equipment and at the same time be operated at a desired resonance frequency f_0. The resonant circuit itself is typically not directly connected to the NMR spectrometer but via a 50 Ω coaxial cable.

The properties of the resonant circuit are determined by the inductance L and resistance r of the coil and the capacities C_1, C_2 of the two variable capacitors. As shown in app. 9.1, the

[f]The spectral excitation range is inversely proportional to τ, i.e. $\Delta f \propto 1/\tau$.

resonance frequency of the capacitively coupled resonant circuit in fig. 2.2 is given by[g]

$$f_0 \approx \frac{1}{2\pi\sqrt{L(C_1 + C_2)}}. \tag{2.27}$$

The input impedance, i.e. $Z_w = Re\{\underline{Z}\}$, in resonance is (app. 9.1)

$$Z_w \approx r\left(\frac{C_1 + C_2}{C_1}\right)^2. \tag{2.28}$$

The resonant circuit has to be impedance-matched to 50 Ω in order to optimize the power transfer from/to the spectrometer. From eqn. (2.28) it is obvious that the variable capacitor C_1 is primarily used to match the impedance, while C_2 allows the tuning of the resonance frequency of the resonant circuit, since the inductance L is fixed.

Experimentally, L and especially r are not well accessible. While the dc-resistance r can be easily measured externally, i.e. $B_0 = 0$ and at room temperature, its value can be affected by the magnetic field and cooling. Furthermore, L might change dramatically if the sample becomes superconducting. However, the quality factor Q, defined as $Q = 2\pi E/\Delta E$, where E and ΔE denote the energy stored in the resonant circuit and the energy dissipated in it during one period, can be used to determine r instead. Q can be measured with a reflection bridge as $Q = f_0/\Delta f$ where Δf is the bandwidth at which the reflected power is 7 dB below the incident power [23]. In the case of a matched and tuned capacitively coupled resonant circuit, Q is given by [24]

$$Q = \frac{1}{r} L\omega_0 \tag{2.29}$$

and therefore offers information on L and r. Losses in the sample, for example by eddy currents, can further influence the value of Q.

While in the case of microcoils the ohmic resistance r in the resonant circuit is completely dominated by the wire of the rf-coil, other parts of the resonant circuit may contribute to the total inductance L as well and therefore store energy in their respective magnetic fields, increasing the measured Q. In this respect, in particular wires and the leads of the coil can contribute.

2.3 Generation of high pressure: the gem anvil cell

A variety of different techniques is available for the generation of high pressure [25]. Static pressures above about 30 kbar however are usually not easily accessible in large volume pressure cells like the clamp cell and are most commonly generated using gem anvil cells (GAC) which shall be described in this section.

[g]The circuit shown in fig. 2.2 is in resonance if the imaginary part of its impedance $\underline{Z}$ vanishes, i.e. $Im\{\underline{Z}\} = 0$. Additionally, the real part of $\underline{Z}$ has to be matched to the input impedance of the NMR-equipment, hence $Re\{\underline{Z}\} = 50\ \Omega$. For further details see app. 9.1.

To be able to achieve very high pressures, one has to use extremely hard materials that are able to sustain such pressures. It is a natural choice then to use the hardest materials available, i.e. diamond or similar gems. The highest static pressures can be achieved in diamond anvil cells (DAC) which are capable of generating pressures above 4 Mbar [26, 27], exceeding the pressure at the center of the earth. Other GACs using cubic-zirconia, sapphire or moissanite anvils can generate pressures close to 170, 260 and 600 kbar respectively [28, 29].

The basic principle underlying all high pressure vessels is the generation of pressure p by applying a force F on an area A

$$p = \frac{F}{A}. \tag{2.30}$$

In order to achieve very high pressures one is thus interested in applying a very large force over an area as small as possible. This already points to the fact that one has to reduce sample size for high pressure experiments. For the purpose of illustration, it shall be mentioned here that a pressure of 100 kbar corresponds to a weight of 1000 kg applied to an area of 1 mm^2. Such conditions are not easily generated.

GACs are a powerful tool as they can be used to investigate materials under extreme conditions otherwise not accessible. However, this is achieved at the cost of sample size. While a variety of techniques are frequently used at high pressure [30, 31], NMR in GACs is not well established as discussed in sec. 2.3.2.

2.3.1 Principle of a gem anvil cell

The principle of a GAC shall be explained on the basis of the piston-cylinder DAC shown in fig. 2.3. The information presented here is based on reviews by Jayaraman [30, 31] and Dunstan and Spain [32, 33].

In a very simple manner, a GAC generates high pressure by squeezing the sample between the culets[h] of two gem stones while confining it by a gasket as shown in fig. 2.3. By filling up the sample space with a pressure transmitting medium, e.g. helium or glycerin, the uniaxial force applied is converted into a hydrostatic or quasi-hydrostatic pressure.

Typically brilliant cut or Drukker[i] design gem stones are used as anvils with culet diameters d of about 1.0 mm or less. The ultimate pressure limit $p_{\max}$ of a GAC is determined by the culet diameter. Empirically, $p_{\max}$ is found to be inversely proportional to d^2. In the case of diamond anvils, $p_{\max}$ is given by [32]

$$p_{\max}[\text{kbar}] = \frac{125}{(d[\text{mm}])^2}. \tag{2.31}$$

Exceeding this value will likely cause failure of the anvil and a DAC should be operated well below this value. For other gem stones similar relations apply, albeit with smaller numerators.

[h] Culet: Flat face of a gem stone.
[i] This is a special gem cut invented for high pressure experiments, refer to [31] for details.

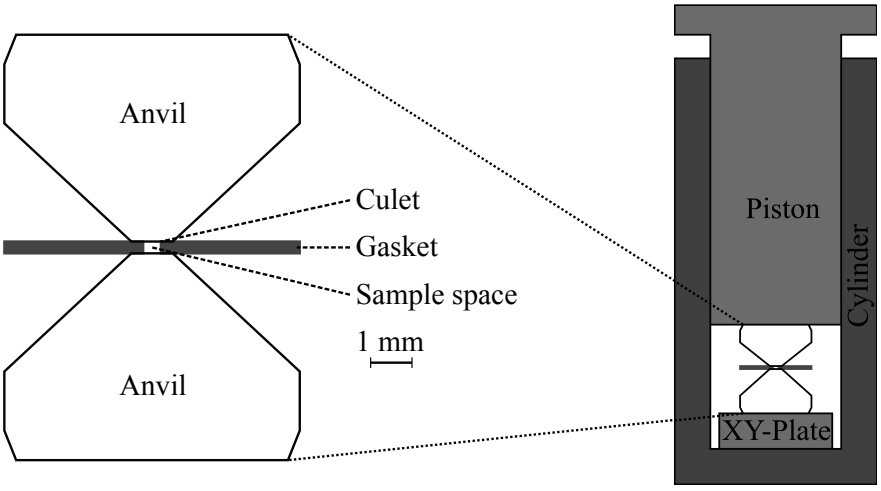

Figure 2.3: Left: schematic diagram of the two diamonds and the gasket in a DAC. Pressure is generated by squeezing the sample between the culets of the diamond anvils while the gasket prevents its extrusion. Often a pressure transmitting medium is used to achieve (quasi) hydrostatic conditions. Right: in a piston-cylinder DAC the force on the anvils is applied by pushing the piston through an external drive. The parallel alignement of the culets is fixed by the piston-cylinder assembly while the xy-alignement can be achieved by moving the xy-plate.

The gasket is usually made from a high strength metal sheet, e.g. stainless steel or rhenium, with a hole of diameter of less than $d/2$. Its initial thickness should be about 1/6th of d or less[j] and will reduce further under pressure. Therefore, the available sample volume decreases significantly for increasing pressures. A metallic gasket has the benefit that it can flow while pressure is applied, sealing the sample chamber and preventing the pressure medium to leak. However, soft metals like copper are unsuitable as the gasket thickness will decrease rapidly with increasing pressure.

To prevent damage to the anvils it is necessary to align the culets of the two diamond anvils very precisely. In the piston-cylinder DAC shown in fig. 2.3, the piston fits tightly into the cylinder preventing a tilt of the anvil in order to guarantee parallelism of the culets. The xy-plate on the other hand is used to align the tips of the anvils. Pressure is generated by pushing the piston down with an external drive. Both, the piston and the xy-plate have to be sufficiently hard to support the diamond anvils to prevent misalignement and successive failure of the anvils. One usually uses very hard backing plates for the direct support of the anvils. If a gem anvil cell is operated correctly, either the hardness of the backing plate or the culet dimensions determine the pressure limit of the cell.

Unfortunately, unlike the anvils, many materials commonly used for the construction of the cell body or as gaskets are not suitable for the use in NMR experiments as they are magnetic. It is possible to build non-magnetic DACs from high strength beryllium-copper (BeCu) and the

[j] Usually the gasket is pre-indented to the desired thickness. Depending on the initial thickness of the gasket, the hole diameter will increase, stay or decrease upon application of pressure. High pressure work should be performed only under the latter condition. For further details see [32, 33].

titanium alloy Ti-6Al-4V. These materials are not as hard as materials conventionally used, e.g. stainless steel or tungsten carbide, however. This is a problem in particular for the backing plates of the anvils as they might fail because of overloading. As gasket material, BeCu and rhenium are in principle suitable unless a high spectral resolution is required (see sec. 2.3.2).

Pressure determination

For the purpose of pressure calibration Ruby fluorescence is commonly applied in gem anvil cells as the anvils are transparent to visible light. A small ruby chip ($10 \ldots 20$ µm diameter) is placed in addition to the sample inside the high pressure region. Its fluorescence can be excited by irradiation with a green laser. The fluorescence wavelength of the R-lines (R_1 and R_2 at 6927 Å and 6942 Å at ambient pressure [31]) is pressure dependent and well calibrated. Using the R_2 line, the pressure can be determined via [31]

$$p\,[\text{Mbar}] = 3.808 \left[\left(\frac{\triangle\lambda}{6942\ \text{Å}} + 1 \right)^5 - 1 \right], \tag{2.32}$$

where $\Delta\lambda$ [Å] denotes the observed change in wavelength. It should be noted that the wavelength is also temperature dependent and splits in the presence of magnetic fields.

2.3.2 State of the art of GAC-NMR

Already in 1987, the first GAC-NMR designs were introduced by Lee et al. [34] and many more were introduced since [4–7, 35–37]. In this section the previously used designs will be briefly reviewed and discussed in respect to the pressure achieved and sensitivity. It should be noted that diamonds have been used exclusively as anvil material previously as other suitable gem stones became available only more recently [28, 29]. The choice of anvil material does not affect a design however.

Due to the low intrinsic sensitivity of NMR and the limited sample space of usually less than $0.5 \times 0.5 \times 0.2$ mm^3 NMR is difficult to observe in GACs. Additionally, the setup of the anvil cells constricts the placement of the rf-coil. Therefore, a variety of different designs have been developed over the last 25 years to detect NMR signals in GACs, including the gasket resonator [34], the split pair coil design [5, 34], the hairpin resonator [4, 37], the split gasket resonator [6] and the single solenoid design [7]. With the exception of the gasket resonator, which uses the gasket itself as the coil, previous designs place the coil outside the high pressure region. Therefore the sample makes up only a small fraction of the rf-coil volume causing a poor sensitivity. An additional problem of such an external coil arrangement is that it is also sensitive to spurious signal from outside the pressure volume [38].

Furthermore, the fact that metallic gaskets have to be used complicates things substantially. A metallic gasket shields the gasket hole because of the skin-effect if the high frequency B_{rf}-field is applied perpendicular to the gasket. Experimentally, this is usually avoided by applying the

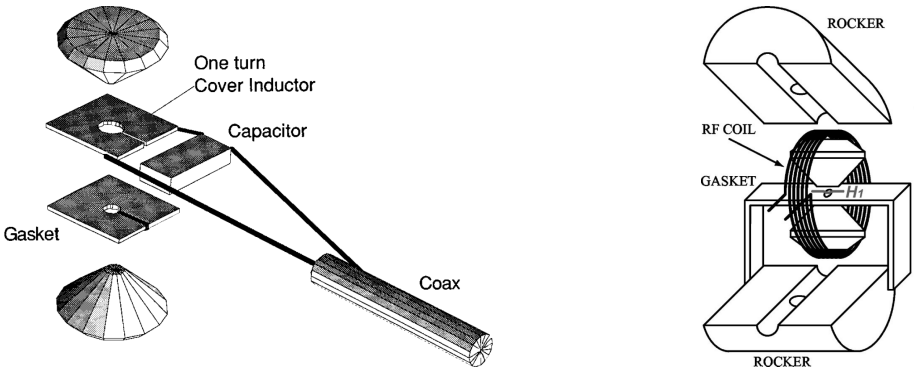

(a) Split gasket resonator (b) Single solenoid

Figure 2.4: (a) Split gasket resonator by Pravica and Silvera (figure taken from [6]). The rf-field generated by the one-turn cover inductor can enter the sample space through the slit of the gasket. A non-magnetic chip capacitor is soldered to the cover inductor to fix the resonance frequency. Fine-tuning and matching is performed outside the magnet via conventional variable capacitors. (b) Single solenoid design by Okuchi et al. (figure taken from [7]). The coil is wound around both anvils and only a fraction of $\eta = 3\times10^{-4}$ is filled with the sample.

B_{rf}-field parallel to the gasket and having it "dip" into the hole [4, 5, 7, 34, 37].

Certainly, sensitivity is the most important attribute of a GAC-NMR design. The highest reported sensitivity is achieved in the design by Okuchi et al. [7] shown in fig. 2.4(b). Here the coil is wound around both anvils resulting in a large inductance of $L = 350$ nH. Using this setup, a SNR of ~ 2 for a single scan in ^{1}H-NMR has been achieved at 27 kbar on a sample of 20 nl methanol (CH_3OH) in a magnetic field of 4.7 T using a 10 kHz filter[k]. This is remarkable given the low filling factor of $\eta = 3\times10^{-4}$.

Another key attribute of GAC-NMR designs is the pressure that can be achieved while data acquisition is possible. In this regard, the split gasket resonator by Pravica and Silvera, shown in Fig. 2.4(a), is of particular interest since the highest pressure NMR-datum was recorded using this setup. It is an interesting approach as the slit in the gasket enables the B_{rf}-field of the cover inductor ($L = 1.8$ nH) to enter the gasket hole. The slit itself is sealed by a mixture of diamond and sodium chloride powder, confining the sample and preventing the gap to close upon application of pressure. It was shown that the split gasket can be pressurized at least up to 260 kbar [6] and NMR data was acquired up to 128 kbar [39]. For comparison, the second highest pressure achieved is about 80 kbar [40, 41] using the split pair coil design [5].

Application of before-mentioned GAC-NMR designs at higher pressure however is limited by the requirement to further reduce the sample space accompanied by a smaller filling factor of the coil resulting in an insufficient sensitivity. Nonetheless, it was feasible to perform ^{1}H-NMR experiments[l] up to 128 kbar on materials such as solid and liquid H_2 [3, 39, 42], organic

[k] Unfortunately, no statement about the temperature was made. However, it is safe to assume that the experiment was performed at room temperature as the methanol would be solid at lower temperatures.

[l] Protons yield a strong NMR signal because of their large gyromagnetic ratio γ and almost 100% natural abundance.

liquids [35–37, 43] or hydrogen hydrates [44, 45]. It should be noted that a common problem encountered in ^{1}H-NMR in GACs is that spurious ^{1}H-signals from the environment can be picked up, hampering an interpretation of the data.

Another noteworthy problem is that the magnetic susceptibilities of the different GAC components, in particular the gasket, often do not match the susceptibility of the sample causing undesired line-broadening making it difficult to resolve functional groups [34]. Using a gasket made out of a high conductivity beryllium-copper alloy rather than the conventional high strength beryllium copper, Okuchi et al. achieved a spectral resolution as good as 0.8 ppm in methanol [46].

In other GAC-NMR experiments by Bertani et al. [40] and Kluthe et al. [41] alkaline metals such as lithium and sodium were investigated up to ~ 80 kbar. Although these metals have smaller gyromagnetic ratios, the short T_1 in metals allows for a faster data accumulation.

It is worth mentioning that a lot of progress has been made recently in the development of high pressure cells for NMR/NQR experiments that offer a larger volume compared to GACs [47–50]. However, their design and fabrication is far more complex in comparison to GACs. One also has to keep in mind that their size has to be considerably larger in order to sustain the pressure which can make their operation in conventional magnets impossible. Furthermore, while the pressures achieved in NMR and NQR experiments using such large volume pressure cells match those in previous GAC-NMR experiments, their ultimate pressure range is far inferior compared to GACs.

As we intended to perform high-sensitivity NMR experiments under such extreme pressure conditions, these circumstances made it necessary for us to develop a novel approach to GAC-NMR that will be described in chap. 3.

3 Microcoil approach to gem anvil cell NMR

An insufficient sensitivity of previous GAC-NMR designs has rendered their application unfeasible in the investigation of condensed matter systems, such as high temperature superconductors, at high pressure. As discussed in sec. 2.3.2 the low sensitivity is a result of the tiny sample size available in these GACs in conjunction with the small filling factor of the rf-coil.

One can therefore pursue two approaches to increase the sensitivity of NMR experiments at high pressure: (a) increase the available sample space by using large volume pressure cells that have a lower pressure limit compared to GACs [47–50] or (b) increase the filling factor of the rf-coil in a GAC-NMR design. The latter is possible by placing the rf-coil inside the high pressure region of the GAC.

This approach was pursuit in the present thesis by using a microcoil inside the high pressure volume as the rf-coil [51, 52]. In this chapter, the necessary steps for preparation of the experimental setup will be discussed and based on first experiments on a zeolite at ambient pressure and metallic aluminum at 42 kbar, it will be demonstrated that the microcoil setup indeed results in a tremendous increase of sensitivity compared to previously developed designs. Furthermore, it will be explained how the setup can be used to determine the superconducting transition temperature T_c of high temperature superconductors under high pressure conditions.

3.1 The novel design

The novel setup was developed in collaboration with Dr. Swee K. Goh from the Shoenberg-Laboratory for Quantum Matter at the Cavendish Laboratory, University of Cambridge. As displayed in fig. 3.1, a small 10-turn microcoil is placed as the rf-coil inside the gasket hole, the high pressure region of a GAC. This microcoil is incorporated into a resonant circuit for tuning and matching by grounding one end on a nearby gasket pin and soldering the other end to an insulated wire that is threaded through the cell body. In this section, the different parts of the experimental setup, i.e. the high pressure cell, the gasket, the microcoil and the NMR probehead, will be described and their preparation explained.

3.1.1 High pressure cell

For all experiments discussed, moissanite anvil cells (MAC) provided and prepared by Dr. Goh were used. During the course of this thesis, similar high pressure cells were also build in Leipzig. They are described in detail in app. 9.3 and have already been employed in NMR experiments

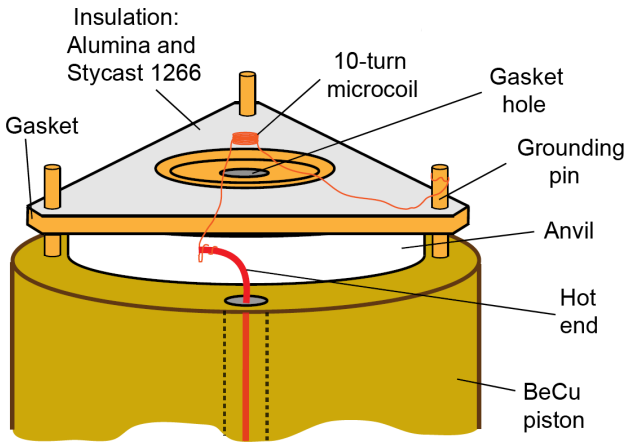

Figure 3.1: Conceptual sketch of the microcoil setup for high pressure NMR experiments in a gem anvil cell. A small 10-turn microcoil placed inside the gasket hole, the high pressure region of the pressure cell, and loaded with the sample is used as the rf-coil. One lead of the microcoil is electrically grounded on a gasket pin (the cell body is electrically grounded itself) while the other is soldered to a wire that is threaded through the pressure cell. The surface of the gasket is insulated by a mixture of stycast 1266 and alumina.

up to 97 kbar [53].

The MACs used are made of non-magnetic high-strength beryllium copper (BeCu)[a] and are based on a GAC design by Dunstan and Spain [32]. They operate on the principle of the piston-cylinder DAC described in sec. 2.3. The force required to generate the pressure is applied by a hydraulic press and can then be clamped by tightening two clamping screws. With a length of 40 mm and a diameter of 18 mm the MACs have a very compact size. A closed cell, an anvil on a piston and a gasket are shown in fig. 3.2.

Anvils

Moissanite anvils were used during this thesis as they are a cost-effective substitute for diamond anvils and are equally suitable from an NMR point of view. Their culets were bevelled to reduce the risk of damaging the leads of the microcoil under pressure. For experiments up to 40 kbar anvils with a culet diameter of 1.0 mm were used. At higher pressures anvils with smaller culets of 0.8 mm diameter were used instead. The anvils are fixed on the piston and the xy-plate with Stycast 1266.

Piston

The piston of the MAC has a few features essential for the setup. It has a total of 7 holes. One 1.2 mm diameter hole in the center to allow optical access of the inner part of the cell for the purpose of pressure measurement via the ruby fluorescence method. Then there are three holes

[a]The beryllium copper alloy C 17200 used contains $\sim$1.8% beryllium, $\sim$0.2% nickel and cobalt and copper as balance.

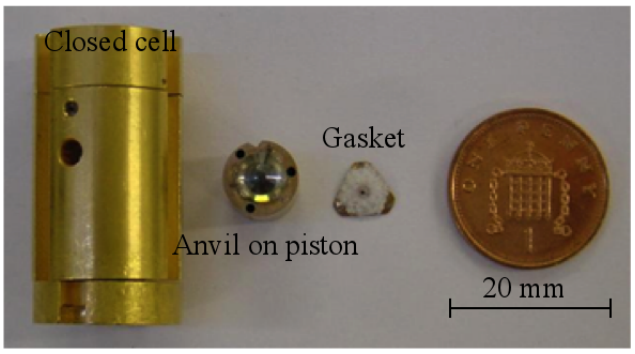

Figure 3.2: A photograph showing a closed moissanite anvil cell, an anvil on a piston and a gasket. The penny is shown for size comparison.

on the outer rim of the piston that are used to fix the three gasket pins which in turn are used to fix the position of the gasket. These gasket pins can be seen in fig. 3.3.

The other three holes of 0.7 mm diameter on the outer rim can be used as feedthroughs (see fig. 3.3). A copper wire of 2 cm length and 0.48 mm diameter, insulated by a polyethylene capsule, is threaded through one of these feedthrough holes. The wire is later used to contact the hot end of the microcoil from the exterior of the cell as depicted in fig. 3.1. The benefit of this arrangement is that the inductance of the hot wire is reduced by the cell body, which is electrically grounded. This is due to the fact that the wire in the feedthrough essentially acts as a coaxial cable. Its properties, i.e. inductance L and capacity C are given by [21]

$$L = \frac{\mu_0 \mu_r}{2\pi} l \ln\left(\frac{D}{d}\right) = 1.5 \text{ nH} \tag{3.1}$$

$$C = \frac{2\pi\epsilon_0\epsilon_r}{\ln\left(\frac{D}{d}\right)} l = 7.1 \text{ pF} \tag{3.2}$$

where l, d and D are the length, diameter of the inner conductor and diameter of the outer conductor, respectively while ϵ_0 and ϵ_r denote the vacuum and relative permittivity. Note that the inductance of 1.5 nH is small compared to that of the microcoil (see below) and that the feedthrough therefore basically acts as a capacitor.

It should be mentioned that the piston can easily be removed from the MAC which is convenient for the purpose of gasket preparation, microcoil placement and sample loading.

3.1.2 Gasket and microcoil preparation, loading of the cell

Next, the steps necessary for preparation of the gasket and microcoil will be described and the loading and pressurization outlined.

Gasket preparation

Gaskets of ca. 9 mm diameter are cut from a 0.5 mm thick sheet of annealed BeCu. Three holes of 600 µm diameter are drilled on the outer rim of the gasket for the gasket pins. A gasket

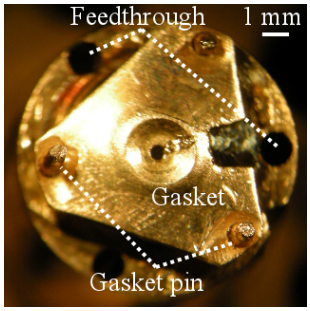

Figure 3.3: Top view, along the axis of the microcoil (not present) of a gasket residing on the anvil of the piston. The gasket, fixed on the anvil by three gasket pins, was pre-indented to a thickness of about 160 µm. A hole of 0.5 mm was then drilled at the center of the gasket to accomodate the microcoil and sample. The gasket was cut into a triangular shape so that one end of the microcoil could later be soldered to the hot wire going through one of the feedthroughs on the outer rim of the piston. The square cutout on the right of the gasket makes it possible to bring the hot wire closer to the gasket reducing the required length of the lead of the microcoil.

is then fixed on the anvil of the piston and pre-indented to a thickness of about 160 µm for experiments up to 40 kbar and 140 µm for higher pressures by applying load on the pressure cell via the hydraulic press.

Load is then released and the gasket removed from the piston. At the center of the pre-indented area, a hole of half the culet diameter, e.g. 0.5 mm for 1.0 mm culets, is drilled to later accomodate the microcoil and sample. Any chippings, remaining from the drilling process, are removed with a scalpel.

Two channels for the leads of the microcoil are then carved into the pre-indented area with a scalpel and rounded off with the tip of a needle. These channels serve as a guide for the leads of the microcoil and reduce the risk of rupture of the wire and failure of the insulation of the leads during application of pressure [33]. In order to be able to contact one lead of the microcoil with the hot wire coming through the piston, the gasket is cut into a triangular shape and an additional square piece is removed where the hot wire is intended to contact the microcoil (see fig. 3.4(a)). This way the hot wire can be brought closer to the microcoil reducing the required length of the microcoil wire. A gasket at this stage in the preparation process is shown in fig. 3.3. It is then fully hardened by heating to 350°C for 30 min and subsequently, its surface is electrically insulated with a mixture of alumina and stycast 1266.

Microcoil preparation

While the use of microcoils offers a significant improvement in sensitivity for NMR measurements in the case of volume limited samples, their preparation is considerably more challenging compared to conventional solenoids.

The microcoils are hand wound from 12 µm diameter copper wire with an insulation thickness

of 2 µm. The wire was bought from Polyfil[b]. In principle, one would be interested in using a thinner wire to increase B_1/i in order to increase the SNR (c.f. eqn. (2.23)). However, to the best of my knowledge this is the thinnest insulated wire commercially available. Furthermore, winding these coils is a very delicate process and becomes considerably more difficult for thinner diameters as one might easily break the wire.

The actual winding is done under a microscope on a rod of a suitable diameter that can be easily rotated about its axis by a turning wheel. First a thin film of lubricant, e.g. teflon spray, is applied on the rod to reduce friction and to prevent damage to the insulation of the wire. Then one end of the wire is fixed on the wheel while the other end is held with tension between two fingers. Special care has to be taken to not rip apart the wire. By rotating the wheel, a microcoil of desired number of turns can be wound. In this state, the wire reacts to a release of tension like a spring by unwinding. Therefore, a small drop of GE varnish, diluted by ethanol, is applied to the microcoil while still under tension to prevent this from happening. After drying of the varnish, it can then be carefully removed from the rod.

Up to 40 kbar microcoils with 10 turns and an inner diameter of 300 µm (coil type A) are used. In order to achieve higher pressures without risking failure of the coil during pressurization, the coil dimensions have to be reduced as the available sample space shrinks at higher pressure. The smallest coils used had about 9 turns and a diameter of 200 µm (coil type B). Expected properties for these microcoils are summarized in tab. 3.1. It is worth mentioning that the use of diamond anvils and rhenium gaskets will enable one to extend the use of the 300 µm microcoils up to considerably higher pressures therefore allowing considerably larger samples.

At this point the microcoil can be placed inside the gasket hole as illustrated in fig. 3.1. Its leads are placed in the two channels and fixed with an insulating mixture of stycast 1266 and alumina as is necessary in the case of metallic gaskets [33].

After the epoxy dried, the leads of the microcoil are cut to a length of about 4 to 5 mm to reduce the resistance. As depicted in fig. 3.1, one end of the microcoil is electrically grounded

[b]Polyfil AG: www.polyfil.ch

Property	coil type A	coil type B
Turns n	10	9
Diameter d [µm]	300	200
Height h [µm]	150	140
Volume V [nl]	10.6	4.4
Inductance L [nH]	31	14
dc-resistance r at RT [Ω]	2.6	2.1

Table 3.1: Calculated properties of microcoils used for experiments. The dc-resistance r takes into account the contribution of the leads of the coil. It is assumed that they have a total length of 8 mm and therefore add 1.2 Ω. The quantity r is a good indicator of the health of the coil as significantly lower values of r imply a short circuit of turns. The inductance L is calculated using eqn. (2.20) and does not include contributions from leads.

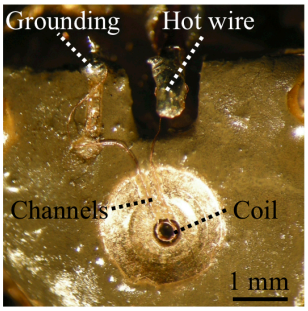

(a) Empty microcoil

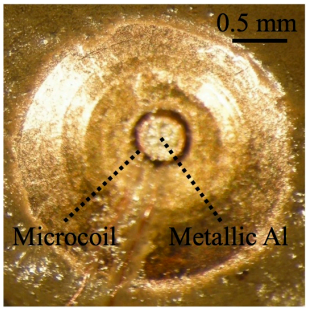

(b) Filled microcoil

Figure 3.4: Top view on the gasket (along the axis the microcoil). (a) A 300 µm diameter microcoil placed inside the gasket hole. The leads are fixed inside the channels with stycast 1266. One end is soldered to the hot wire while the other end is grounded on the gasket. (b) Microcoil filled with a powder of metallic aluminum as the sample.

on a nearby gasket pin while the other end is soldered to the 0.48 mm wire coming though the feedthrough in the piston. Fig. 3.4(a) shows the completed gasket and microcoil setup.

Loading of the sample and application of pressure

The microcoil can then be loaded with the sample. Additionally, a small ruby chip is placed inside the microcoil which serves as a pressure gauge via the ruby fluorescent method [54].

Afterwards, the gasket hole is flooded with a pressure transmitting medium such as glycerin or daphne 7373. These oils were found to be simple to load as they are highly viscous and do not evaporate quickly. Glycerin in particular is suitable as it ensures nearly hydrostatic conditions up to 70 kbar [55]. It is worth mentioning that in principle condensed gases like N_2 and He or a 4:1 mixture of methanol:ethanol are more suitable as pressure transmitting medium as they offer nearly hydrostatic conditions up to well above 100 kbar [30]. However, in most cases powder samples were used which are difficult to load under cryogenic conditions (He and N_2). The use of the methanol:ethanol mixture was tested but terminated after multiple failed loading attempts due to the quick evaporation of the liquid which eventually lead to the breaking of an anvil.

The pressure cell can now be closed by inserting the piston into the MAC. Pressure is then carefully applied with a hydraulic press and clamped by tightening the two clamping screws[c]. The resistance of the microcoil is now checked with a multimeter to verify its functionality. Pressure is measured via the ruby fluorescence method[d]. If necessary, the pressure is further increased by using the hydraulic press. A cell is then left to relax for a few hours and pressure is checked again. In the case of the pressure cells prepared, a drop of about 2 kbar was then typically observed during this time. However, the pressure then decreased no further even over

[c]Unfortunately no direct gauge of the applied load is available for the hydraulic press used and thus experience guides the pressurizing process. The pressure-load relation however can be non-linear [32] and may vary from experiment to experiment.

[d]A homebuilt fluorescence spectrometer at the Quantum Matter group in Cambridge was used for that during the experiments described here.

a time of several months in which the pressure cell was often exposed to multiple cooling cycles down to low temperatures.

It should be noted that in some cases the microcoils can be distorted considerably during application of pressure as their height is only slightly less than the thickness of the pre-indented gasket. Sometimes even, a microcoil is damaged or destroyed completely upon application of pressure. To evaluate the health of a microcoil, in particular the comparison of the measured and calculated dc-resistance of a microcoil proved to be useful, as an observation of a considerably lower value of implies a short circuit of coil turns. If the measurement of the resistance indicates that the coil is heavily damaged or even destroyed (i.e. very high values of the resistance on the order of MΩ), the cell has to be opened again and the preparation process must be started over again.

3.1.3 NMR setup

In the closed condition, the pressure cell is simple to handle. The next task is to incorporate the microcoil into a resonant circuit similar to the one shown in fig. 2.2. For that purpose, the MAC is mounted on a homebuilt NMR probehead that uses two variable capacitors for tuning and matching. Its position on it is fixed with a cable tie. This way, the end of the microcoil soldered to the gasket pin is electrically grounded as the whole cell body itself is grounded on the probehead. By soldering the 0.48 mm hot wire coming out of the MAC to the capacitive current divider of the probehead, the resonant circuit is completed. Fig. 3.5(a) shows a MAC mounted on a probehead. It should be noted that the orientation of the pressure cell is dictated by the requirement for B_{rf} to be perpendicular to the static field B_0. The homebuilt NMR-probeheads are equipped with Cernox temperature sensors (for monitoring the sample temperature) and fit into the 5 cm diameter, bottom loading cryostats of the available magnets (2.35, 7.04, 11.74 and 17.6 T). They therefore easily allow temperature dependent measurements down to 4 K.

In contrast to most of the previous GAC-NMR designs discussed in sec. 2.3.2, this setup is very flexible as it can be operated in the frequency range from ∼100 MHz up to 300 MHz without any modifications using the two variable capacitors of the current divider with $C = 1 \ldots 10$ pF or $1 \ldots 20$ pF. For lower frequencies, chip capacitors can be added in parallel to the variable capacitors as required and the setup has been used successfully down to 30 MHz. Fig. 3.5(b) shows an example resonance curve of a 200 µm microcoil at 42 kbar containing a single crystal of $YBa_2Cu_4O_8$ and tuned and matched at ∼134.5 MHz recorded with a spectrum analyzer.

3.2 Performance of the microcoil setup

Based on first tests at ambient pressure on a powder of zeolite A and on a powder of metallic aluminum at 42 kbar, the performance of the microcoil approach will be demonstrated. It will be shown that sensitivity is improved by about two orders of magnitude compared to previous GAC-NMR designs and that ultimately high sensitivity NMR experiments at high pressure are

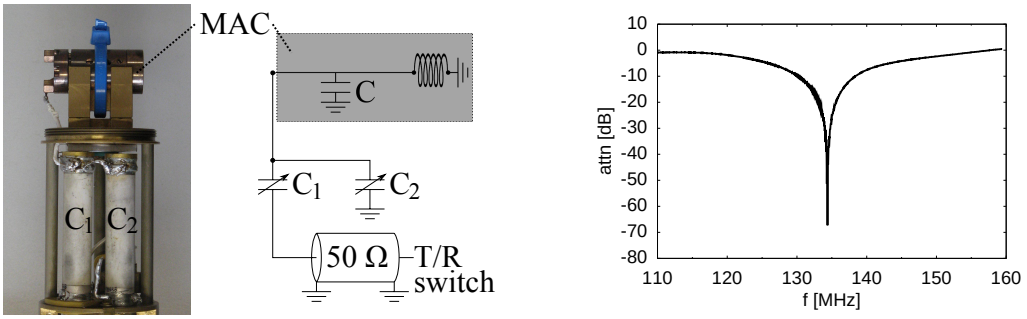

(a) Probehead and schematic wiring

(b) Resonance curve

Figure 3.5: (a) The photograph shows a closed MAC mounted on a probehead with the cell body electrically grounded. The hot wire coming out of the cell is connected to the two variable capacitors (1 . . . 20 pF) that are used for matching (C_1) and tuning (C_2). In the block diagram to the right, the schematic wiring of the resonant circuit is depicted. It is connected to the T/R switch of the NMR-spectrometer via a 50 Ω coaxial cable. Note that the feedthrough arrangement of the hot wire adds a capacity of about $C = 7$ pF in parallel to C_2. (b) Resonance curve of a 200 µm microcoil at 42 kbar tuned and matched at 134.5 MHz. The resonance circuit had a quality factor of $Q = 12$.

feasible with the microcoil setup.

3.2.1 Zeolite A

The proof of concept of the novel GAC-NMR setup was performed by ^{23}Na and ^{27}Al NMR on a linde type A zeolite with the chemical composition $Na_{12}((AlO_2)_{12}(SiO_2)_{12})$*$27H_2O$ at room temperature in a magnetic field of 11.74 T [51]. Both nuclei have a natural abundance of 100% and have a nuclear spin of 3/2 (^{23}Na) and 5/2 (^{27}Al). The zeolite has a unit cell volume of 1693.24 Å^3 and a density of 2.5 g/cm^3 [56]. The low density of the ^{23}Na and ^{27}Al in the zeolite offered a good opportunity to test the limit of sensitivity of the setup.

At 11.74 T both nuclei have a resonance frequency of about 130 MHz. Preliminary tests were carried out with a regular NMR setup. A resonance frequency of $\nu_0 = 130.320$ MHz, a spectral full width at half maximum (FWHM) of $\Delta\nu = 1.8$ kHz and a relaxation time of $T_1 = 1.4$ ms was found for ^{27}Al while $\nu_0 = 132.288$ MHz, $\Delta\nu = 0.8$ kHz and $T_1 = 0.8$ ms were measured for ^{23}Na. The small values of T_1 are ideal for short repetition times while searching for signal.

The pressure cell was prepared as described in sec. 3.1, only difference being that the insulation of the feedthrough wire was not further improved by the polyethylene capsule. A microcoil of type A, i.e. 10 turns and 300 µm diameter, with a dc-resistance of $r = 3.0$ Ω was used and filled with the zeolite powder as shown in fig. 3.6(a). Unfortunately, it was not possible to weigh the content of the microcoil but the zeolite was not packed densely to prevent damage to the coil. Assuming a filling of 50% and taking into account the volume of the microcoil of 10.6 nl, it is estimated that the coil contained ~ 5 µg of the zeolite powder. With the given density and unit cell volume, this corresponds to a total of 1.7×10^{16} Na and Al nuclei. It should be noted that

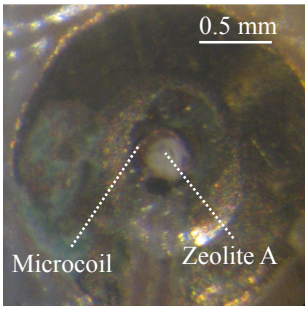

(a) Zeolite A, 1 bar

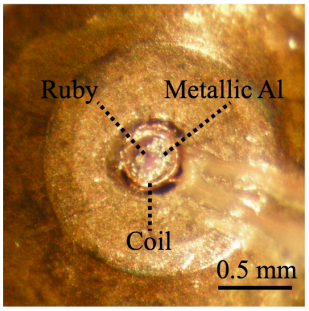

(b) Metallic Al, 42 kbar

Figure 3.6: Top view, along the axis of the microcoil, showing the pre-indented region of the gasket of the MACs. For tests at ambient pressure one cell was loaded with zeolite A (a). A cell used for experiments at 42 kbar on metallic aluminum is shown in (c). It contained a fine powder of metallic aluminum and a ruby chip. In both cases, the microcoils had 10 turns and a 300 µm diameter.

this is a rather crude and conservative estimate and it is well possible that the coil contained even less of the sample. No pressure transmitting medium was used and the cell was closed without applying pressure.

The closed cell was mounted on a homebuilt probehead and connected to its two variable capacitors (1 . . . 10 pF) as described earlier. An additional 10 pF chip capacitor had to be soldered in parallel to the variable tuning capacitor in order to reach the desired frequencies. The resonant circuit was tuned and matched to 130.320 MHz for ^{27}Al and 132.288 MHz for ^{23}Na as determined earlier and its quality factor Q was measured at the probe terminal from the return loss recorded with a GW INSTEK GSP-830 spectrum analyzer. Signal was recorded by accumulating 10000 scans following a 1 W rf-pulse of defined duration τ with a dwell time of 2 µs and a recycle delay of 50 ms. The average power of the rf-pulse was determined and monitored with a calibrated directional coupler. To determine the $\pi/2$-pulse length, τ was varied from 1 . . . 6 µs in a nutation experiment.

Results and discussion

First, the properties of the resonant circuit will be discussed. At 130 MHz, the resonance circuit had a quality factor of $Q \approx 12$. With a skin depth in copper at 130 MHz of [21]

$$\delta = \sqrt{\frac{\rho}{\mu_0 \mu_r \pi f}} = 5.7 \text{ µm}, \tag{3.3}$$

the resistance r is essentially unchanged compared to its dc-value of 3 Ω. Furthermore, it is reasonable to assume that Q is determined by the properties of the microcoil only as no significant energy losses are expected to be caused by the sample and high-Q capacitors ($Q > 2000$ at 100 MHz) were used. Using eqn. (2.27 - 2.29) it can then be concluded that the total inductance was $L = 44$ nH, with matching and tuning capacities of $C_1 = 8$ pF and $C_2 = 25$ pF. This is in

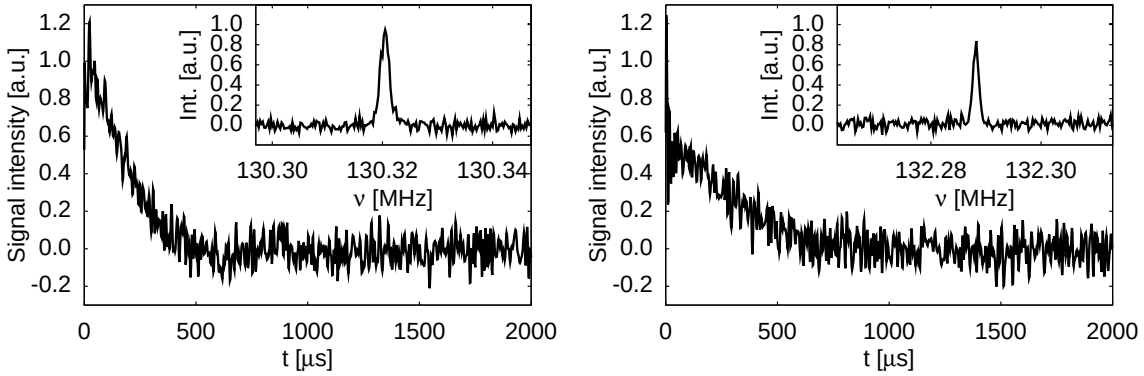

(a) ^{27}Al FID and spectrum

(b) ^{23}Na FID and spectrum

Figure 3.7: Real part of the recorded FIDs (main panel) and spectra (inset) of aluminum (a) and sodium (b) nuclei in zeolite A after 10000 scans following a single rf-pulse of 1 W and a duration $\tau = 2$ µs with a repetition time of 50 ms and a spectral bandwidth of $\Delta\nu = 200$ kHz. The signal intensities of both FIDs have been normalized to that of ^{27}Al at $t = 0$ µs.

reasonable agreement with expected values. The somewhat larger value of $L = 44$ nH compared to the calculated value of ~ 30 nH (c.f. tab. 3.1) can be explained by considering the additional contributions from the legs of the microcoil. Their inductance is given by [21]

$$L\,[\mathrm{nH}] = 2l\left(\ln\frac{4l}{d} + \mu_r K - 1\right) \tag{3.4}$$

where l [cm] and d [cm] denote the length and diameter of the leads, $\mu_\mathrm{r} = 1$ (copper) is the relative permeability and $K = 0.25$ is a correction term taking into account the frequency dependence. With an estimated length of 5 mm, the two leads are expected to contribute 15 nH.

Next, the results of the ^{27}Al and ^{23}Na NMR experiments will be discussed. Signal was successfully recorded and fig. 3.7 shows sample FIDs and spectra for a rf-pulse duration of $\tau = 2$ µs. Experimentally, the intensity of the ^{27}Al was about 1.5 times higher than that of ^{23}Na. Taking into account the different spin factor $I(I+1)$ and the slightly different γ-values of the nuclei ^{27}Al ($I = 5/2$) and ^{23}Na ($I = 3/2$), one would expect a 2.2-fold higher intensity of the aluminum signal based on eqn. (2.23). However, it is reasonable to assume that the intensity is only given by the central transition $-1/2 \leftrightarrow 1/2$ for the case of non-selective excitation of all transitions in which case the intensity ratio of ^{27}Al to ^{23}Na drops to about 1.4 [57]. This is what is found within experimental error.

The spectra reveal that no changes in the resonance frequencies of 130.320 MHz for ^{27}Al and 132.288 MHz for ^{23}Na occur in the high pressure setup. However, the linewidths of $\Delta\nu = 2.0$ kHz for ^{27}Al and $\Delta\nu = 1.3$ kHz for ^{23}Na are somewhat larger than $\Delta\nu = 1.8$ kHz and $\Delta\nu = 0.8$ kHz determined with the regular setup. If the increase in linewidth was only due to field inhomogeneities caused by the setup, one would expect a similar relative increase in $\Delta\nu$ for both nuclei which is clearly not the case. Instead, it is concluded here that the increase in linewidth in

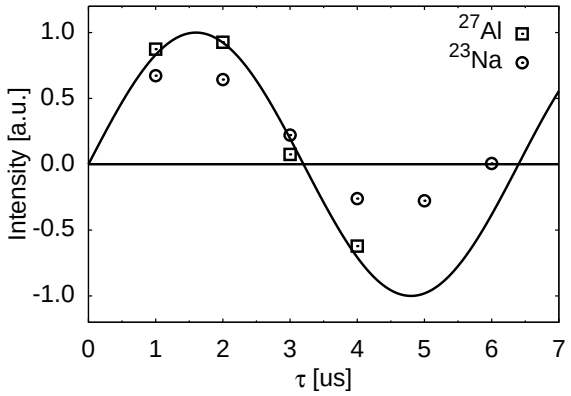

Figure 3.8: The characteristic nutation curve of the ^{27}Al and ^{23}Na signals of the zeolite A recorded in the MAC. A $\pi/2$-pulse of about 1.6 µs is found experimentally. The solid line is a fit of a sinus to the ^{27}Al data and intended as a guide to the eye.

particular for ^{23}Na was caused at least partially by a dehydration of the powder of zeolite A over the course of the experiments, which is not related to the setup. Nonetheless, a resolution of at least 1.3 kHz at $\sim$130 MHz, or 10 ppm, can be achieved using this setup. As this is by far sufficient for studying the condensed matter systems of interest, the resolution limit of the setup was not investigated further.

In fig. 3.8 the result of the nutation experiment is shown by plotting the integral of the FID signal as a function of the rf-pulse duration τ. From the data, a $\pi/2$-pulse duration of about 1.6 µs can be estimated which is on the order of 0.8 µs calculated using eqn. (2.26). The fact that a larger value of $\tau_{\pi/2}$ was observed experimentally is not unexpected as the energy of the magnetic field B_1 is not only stored in the volume of the coil as was assumed in the derivation of eqn. (2.26).

The SNR can be estimated from the data recorded with a rf-pulse duration of $\tau = 2$ µs shown in fig. 3.7. After 10000 scans with a filter width of $\Delta f = 200$ kHz a SNR of ~ 18 and ~ 10 was acquired for ^{27}Al and ^{23}Na. This corresponds to a SNR for a single scan of 0.18 and 0.10, respectively. From eqn. (2.23) and eqn. (2.24) a maximum ($K = 1$) single scan SNR of 1.65 and 0.73 for ^{27}Al and ^{23}Na is calculated. Taking into account that in the case of non-selective excitation the intensity of the central transition is only a fraction of 9/35 (^{27}Al) and 2/5 (^{23}Na) of that [57], a maximum single scan SNR of 0.42 and 0.29 is expected. That is only a factor of two to three higher than measured experimentally. Due to the inductance in the coil's legs and a non-perfect homogeneity of the B_1-field ($K < 1$), the experimental values are expected to be somewhat lower.

To evaluate the performance of the setup, the SNR is compared to the previously highest SNR reported by Okuchi et al. [7] according to eqn. (2.23). Taking into account the different values of γ, B_0, Δf, number of spins and intensity ratio of 9/35 (^{27}Al) the novel microcoil setup increases sensitivity by a factor of more than 70. Under similar experimental conditions, this means a reduction in measurement time by a factor of $\sim$5000.

3.2.2 Metallic aluminum at 42 kbar

The first experiments at high pressure were performed on a powder of metallic aluminum [52,58], their results are discussed in detail in chap. 4. This section focuses on the performance of the setup under such high pressure conditions using the measurements on aluminum at 42 kbar as an example. It will be demonstrated that the setup works well even under such extreme conditions.

As the sample, a 99.97% pure aluminum powder of less than 44 μm diameter particle size (-325 mesh) purchased from Alfa Aesar was used. Aluminum has a density of 2.7 g/cm^3 and a face-centered-cubic lattice with a unit cell volume of 66.43 Å^3. In preliminary tests at ambient pressure in a MAC, a resonance frequency of $\nu_0 = 130.523$ MHz, a FWHM of $\Delta\nu = 11$ kHz and a spin-lattice relaxation time of $T_1 = 6.3$ ms were found for the ^{27}Al nuclei in the metallic aluminum.

A 10-turn, 300 μm diameter microcoil, shown after sample loading in fig. 3.6(b), was used. About 20% of the volume of the microcoil was occupied by the ruby chip. As the aluminum powder was not densely packed, it is reasonable to assume that the filling factor of the powder in the available space is less than 50% corresponding to a loading of 10 μg at most. Taking into account that the skin-depth in aluminum is ~ 7.4 μm at 130 MHz and that the particle size was less than 44 μm an estimated 40% of the aluminum nuclei contributed to the signal. This corresponds to about 1×10^{17} nuclei. Again, this is a rather conservative estimate.

Daphne 7373 was used as the pressure transmitting medium. After closing and pressurization to 42 kbar, the dc-resistance of the microcoil was measured to be 2.3 Ω and the resonant circuit had a quality factor of $Q = 18$ at 130 MHz. These NMR measurements were done at room temperature (297 K) in a magnetic field of 11.74 T [58]. Similar to the tests on the zeolite powder, signal was recorded by accumulating 1024 scans following a 1 W rf-pulse of defined duration τ with a dwell time of 2 μs and a recycle delay of 50 ms. The $\pi/2$-pulse duration was determined by variation of the pulse length τ in a nutation experiment.

Results and discussion

Signal was observed successfully and a sample FID and spectrum recorded with a pulse duration of 2 μs is shown in fig. 3.9(a). As will be discussed in more detail in chap. 4, a decrease of the resonance frequency and a slight increase of the FWHM was observed.

The result of the nutation experiment is shown in fig. 3.9(b). Up to 4.5 μs the datum fits well to a sinusoidal shape while for longer pulse durations the datum deviates considerably. This is not unexpected taking into account that the amplitude of the magnetic rf-field is not uniform over the sample space due to the small ratio of coil height to coil diameter. Furthermore one has to consider the decay of that amplitude in the sample because of the skin-effect. From fig. 3.9(b) it can be inferred that the pulse duration of maximum signal was $\tau_{\pi/2} = 1.9$ μs. The value compares well to that of 2.0 μs found at ambient pressure in a similar cell under the same experimental conditions (not shown). Both values are somewhat larger than that found for ^{27}Al in the zeolite likely because of the skin-effect in the metallic sample.

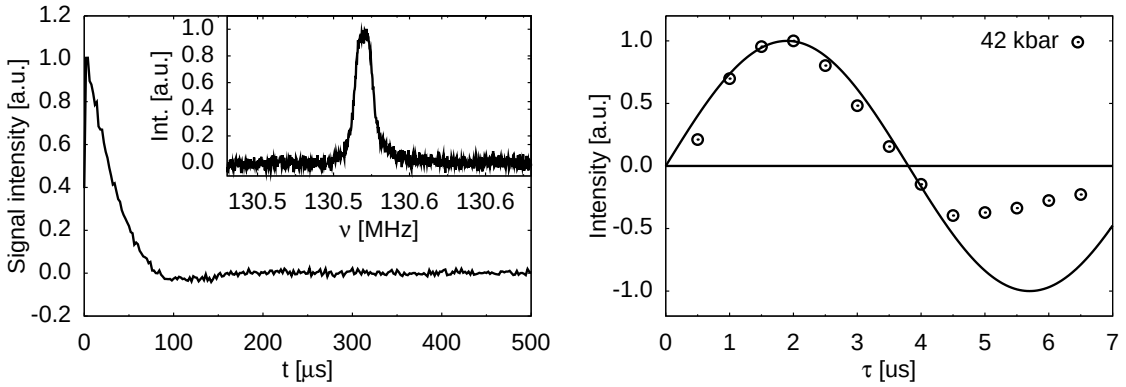

(a) FID and spectrum

(b) Nutation experiment

Figure 3.9: Metallic aluminum at 42 kbar: (a) Real part of the FID (main panel) and spectrum (inset) after 1024 scans following a single 1 W rf-pulse of 2 µs duration with a repetition time of 50 ms and a filter width of $\Delta f = 500$ kHz. (b) Result of the nutation experiment. A $\pi/2$-pulse duration of $\tau_{\pi/2} = 1.9$ µs is found experimentally. The solid sinusoidal line is a guide to the eye.

The maximum single scan SNR of 6 was recorded for a pulse duration of $\tau = 2$ µs which is only slightly less than the theoretical maximum SNR of 11 calculated using eqn. (2.23) and eqn. (2.24). Again compared to the SNR reported by Okuchi et al. [7], this indicates a 165-fold increase in sensitivity. This is about twice the factor estimated for the experiments on the zeolite. The disparity between these factors is likely due to the uncertainty in the sample amount.

3.2.3 Conclusions from the first tests

Based on experiments performed at ambient pressure on a powder of zeolite A and at 42 kbar on metallic aluminum it has been shown that a tremendous increase in sensitivity by about *two orders of magnitude* is possible with this novel design compared to previous GAC-NMR setups.

Within the resolution of the experiments, the setup does not influence the observed resonance frequency. Furthermore, a spectral resolution of at least 10 ppm at 130 MHz is achieved. However, it is likely that this value does not represent the lower limit of the spectral resolution and further experiments would be required to determine it. Nonetheless, for the systems of interest in this thesis, i.e. metallic aluminum and the high temperature superconductor $YBa_2Cu_4O_8$, this is by far sufficient and allows precise measurements of the shift in resonance frequency.

It is also worth pointing out that the properties of the setup, especially with regard to the microcoil and its sensitivity, are well understood by the theory described in sec. 2.2. This enables the estimate of experimentally important quantities such as duration of the $\pi/2$-pulse.

3.3 Measurement of T_c

In the case of the ^{17}O exchanged powder of the high temperature superconductor $YBa_2Cu_4O_8$ (see sec. 6 for details), the GAC-NMR design was also used to determine the superconducting

transition temperature T_c in zero field. This has the benefit that the NMR and T_c-measurements can be performed on the same sample and under the very same pressure conditions.

The method is based on the fact that the inductance L of the microcoil depends on the magnetic susceptibility χ_m of the sample it encloses. It has been used to determine T_c of a material in a similar fashion in large volume high pressure cells by other groups [14, 59] . If η denotes the filling factor of the sample in the coil, L is given by

$$L = L_0 \left(1 + \eta \chi_m\right), \tag{3.5}$$

where L_0 is the vacuum inductance given by eqn. (2.20). In the normal state of a superconductor χ_m vanishes and to a good approximation L is given by its vacuum value L_0. The superconducting state of a material however is characterized by perfect diamagnetism, i.e. $\chi_m = -1$ in which case the inductance of the coil is reduced to $L = L\,(1-\eta)$. Recalling that the resonance frequency of the resonance circuit f_0

$$f_0 = \frac{1}{2\pi\sqrt{L\left(C_1 + C_2\right)}} \tag{3.6}$$

depends inversely on $\sqrt{L}$, one expects to be able to observe such changes by monitoring the temperature dependence of f_0 around T_c.

The measuring procedure will be described next. It should be noted however that the method is not suitable for searching for T_c over a large temperature range for reasons that will be discussed below. It nonetheless proved well suitable as an estimate of T_c at a specific pressure was inferred from values found in the literature.

For a specific pressure point, the probehead was initially cooled down to a temperature about 5 to 10 K above the expected superconducting transition. The resonance circuit was then tuned and matched at the lowest resonance frequency possible, usually about 100 MHz (the relative change in L is more pronounced at lower frequency due to skin-depths effects). No further tuning and matching was done afterwards. To determine the resonance frequency f_0, the resonance curve of the resonance circuit was recorded with a GW INSTEK GSP-830 spectrum analyzer. The probehead was then cooled down slowly at a rate of $\sim$20 K per hour to a temperature 20 K below the initial starting point. During the cooling down, the temperature and the resonance curve (which was later used to determine $f_0(T)$) were recorded every 30 s. To rule out a lagging of the sample temperature, the process was then repeated while heating up. T_c was then extracted graphically from the plot of $-\Delta f = -(f_0(T) - f_0(T_{max}))$ vs. T as a characteristic drop and change in slope occurs at T_c[e]. After the proof of concept, this procedure was incorporated into a python program by Jonas Kohlrautz [60] for the purpose of automatization. Fig. 3.10 shows a sample curve of $-\Delta f$ vs. T recorded at 30 kbar while cooling down.

It is necessary to make a few remarks regarding the applicability of this method. First of

[e]The plot of $-\Delta f$ vs. T is chosen here as it is similar in appearance to plots of χ_m vs. T from measurements of the magnetic susceptibility which are often used to determine T_c.

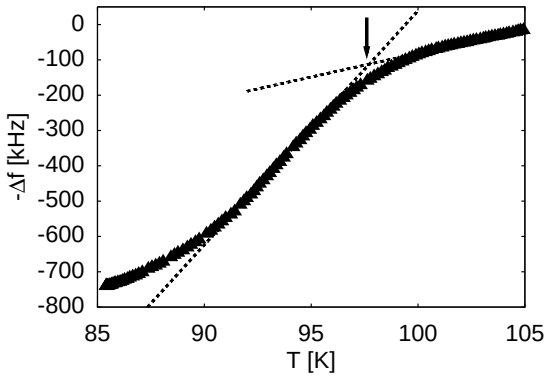

Figure 3.10: Sample plot of $-\Delta f$ vs. T recorded at 30 kbar to illustrate the determination of T_c via the drop in $-\Delta f$. The kink in slope at 97.5 K (indicated by the arrow) is caused by the superconducting transition and was used to determine T_c. The dashed lines are a guide to the eye.

all, from fig. 3.10 it is obvious that f_0 changes not only due to the superconducting transition but appears to drift with temperature. Wether this is caused by changes in other parts of the resonant circuit, e.g. due to a temperature drift of the tuning and matching capacitors, or represents changes of the sample is unclear. The technique is therefore only applicable, if the drop in L below T_c is large compared to the effects of the thermal drift. Furthermore, this technique can be applied only in a limited temperature range as the matching of the resonance circuit changes with temperature making a precise determination of f_0 difficult. Within the 20 K range used, the de-matching of the resonance circuit is small however.

4 Metallic aluminum

We decided to first apply the novel GAC-NMR design to investigate a supposedly simple and NMR friendly system, metallic aluminum, under high pressure conditions of up to 101 kbar. Surprisingly, these experiments revealed an unexpected decrease of the pressure-dependent electronic density of states (DOS) that violates a free electron behavior [52, 58].

This chapter will start with a brief introduction to the DOS in metals and its role for the Knight-shift K and the spin-lattice relaxation time T_1. Then, the results of the high pressure NMR experiments will be discussed that include a characteristic beat pattern in the FID up to 54 kbar, an unexpected increase in the linewidth above 42 kbar and changes of K and T_1 that cannot be understood in terms of the free electron model. Finally, based on numerical band structure calculations, it will be concluded that the pressure dependence of K and T_1 indicate a pressure induced Lifshitz-transition.

4.1 Introduction

This section covers the theoretical background of the density of states at the Fermi level E_F and how it affects K and T_1 in metallic aluminum. Previous pressure studies of the Fermi surface of aluminum will also be reviewed.

4.1.1 Electrons in metals

The behavior of electrons in solids is a many-body problem [61] and the Hamiltonian describing them contains interactions with nuclei and other electrons. For simplicity, it is assumed that the nuclei reside on a rigid lattice (adiabatic approximation). Furthermore, it shall be assumed that the electron-electron interactions can be well approximated by including them in an effective one-electron potential $U(\boldsymbol{r})$ that is periodic in the lattice, i.e. $U(\boldsymbol{r}+\boldsymbol{R})=U(\boldsymbol{r})$, where $\boldsymbol{R}$ is a vector of the Bravais lattice of the crystal. A single electron in the solid is then described by the simplified one-electron Schrödinger equation

$$\mathscr{H}\psi = \left[-\frac{\hbar^2}{2m}\nabla^2 + U(\boldsymbol{r})\right]\psi = E\psi. \tag{4.1}$$

Solutions to eqn. (4.1) are Bloch-wave functions ψ of the form

$$\psi_{n\boldsymbol{k}}(\boldsymbol{r}) = e^{i\boldsymbol{k}.\boldsymbol{r}}\phi_{n\boldsymbol{k}}(\boldsymbol{r}), \tag{4.2}$$

where $\boldsymbol{k}$ indicates the wave vector, n the electron band index[a] and the condition $\phi_{n\boldsymbol{k}}(\boldsymbol{r}+\boldsymbol{R})=\phi_{n\boldsymbol{k}}(\boldsymbol{r})$ must be satisfied for all vectors $\boldsymbol{R}$. Note that the wave functions $\psi_{n\boldsymbol{k}}$ can be described using atomic wave functions as the basis. This allows one to determine to what extent $\psi_{n\boldsymbol{k}}$ is of s-, p-, d- or even f-character[b].

Obviously, the energy E of a Bloch-electron depends on $\boldsymbol{k}$. For example in the theoretical model of a free electron gas, which often quite well describes the physical properties of simple metals, it is assumed that the potential $U(\boldsymbol{r})$ vanishes throughout the crystal. The wave functions are then reduced to plane waves $\psi=e^{i\boldsymbol{k}.\boldsymbol{r}}$ and $E_n(\boldsymbol{k})=E(\boldsymbol{k})$ is simply given by

$$E(\boldsymbol{k}) = \frac{\hbar\boldsymbol{k}^2}{2m}. \tag{4.3}$$

Density of states and the Fermi surface

The density of states (per unit cell of volume V) $N(E)$, that is the number of allowed wave vectors $\boldsymbol{k}$ in the energy range from E to $E+dE$, is given by the summation over all bands n [61]

$$N(E) = \sum_n N_n(E) \tag{4.4}$$

$$= 2\times\sum_n \frac{V}{8\pi^3}\int_{S_n(E)}\frac{dS}{|\nabla_{\boldsymbol{k}}E_n(\boldsymbol{k})|}, \tag{4.5}$$

where the factor 2 accounts for the spin-degeneracy and the integrations are carried out over the surfaces $S_n(E)$ of constant energy. The ground state of a system that contains N Bloch-electrons per unit cell is then constructed by populating all one-electron levels $\boldsymbol{k}$ with an energy $E_n(\boldsymbol{k})$ less than E_F, where the Fermi energy E_F is defined by

$$N = \int_{-\infty}^{E_\mathrm{F}} N(E)dE. \tag{4.6}$$

In metals, a number of electronic bands may be filled only partially and E_F is then within the energy range of these bands. For each such band there is a surface in $\boldsymbol{k}$-space that separates the occupied and unoccupied energy states. The set of these surfaces is called Fermi surface (FS). Many physical properties of metals like conductivity, specific heat or the superconducting transition temperature depend on the topology of the FS and the density of states at the Fermi level $N(E_\mathrm{F})$.

Van Hove-singularities and Lifshitz-transitions

Critical points in $N(E)$ at which $\nabla_{\boldsymbol{k}}E_n(\boldsymbol{k})$ vanishes are called van Hove-singularities and influence the physical properties of materials profoundly, especially if close to E_F. The position of

[a] The band index n occurs as for a given $\boldsymbol{k}$ there are multiple Eigenstates.

[b] The different atomic wave functions are labeled with indexes s, p, d and f according to their angular quantum number. In general, the wave functions $\psi_{n\boldsymbol{k}}$ will be a mixture of s-, p-, d- and f-orbitals. Only at specific symmetry points in $\boldsymbol{k}$-space the character of $\psi_{n\boldsymbol{k}}$ may be described by a distinct orbital.

these singularities in E can be affected by parameters like chemical doping [62], magnetic field [63] or pressure [1]. If a van Hove-singularity passes through the Fermi level, the metal undergoes a so-called electronic topological transition that is associated with a change in topology of the FS [64]. In honor of I. M. Lifshitz, these transition are also referred to as Lifshitz-transitions.

Qualitative theories like the free electron model, in which case $N(E) \propto \sqrt{E}$, often describe the density of states with analytic functions. However, such analytic functions cannot describe $N(E)$ near van Hove-singularities as it behaves non-analytic in their vicinity. In fact, in many materials a realistic description of $N(E)$ is only possible via numerical calculations that, for example, apply density functional theory [65]. Experimentally, theories and numerical calculations can be tested by varying the before-mentioned parameters like pressure as they influence $N(E)$ and the position of van Hove-singularities.

Previous pressure studies of the Fermi surface of aluminum

First of all it, should be noted that aluminum remains in a face-centered-cubic (fcc) lattice structure up to 2.2 Mbar [66][c]. Therefore changes of the FS under pressure cannot be induced by structural changes of the lattice. Application of a pressure of 100 kbar decreases the unit cell volume by 10% (bulk modulus of $B = 727 \pm 30$ kbar and pressure derivative of $B' = dB/dp = 4.3 \pm 0.8$ [67]) which should affect the FS significantly[d].

Early ambient pressure studies suggested that the FS is well described by the free electron model [68] (it is worth mentioning that the FS is entirely contained in the second and third Brillouin zone [61]). De Haas-van Alphen experiments at moderate pressures of up to 7 kbar however hinted at deviations from the free electron model [69] while Fermi-momenta measurements up to 100 kbar on the other hand were in agreement with a free electron interpretation [70] (note that the error bars associated with the reported data in [70] are sizable). Magneto-thermopower measurements carried out under *uniaxial* pressure conditions of up to 12 kbar indicated a Lifshitz-transition at $\sim$5 kbar [71]. To the best of my knowledge, a Lifshitz-transition under hydrostatic pressure conditions has not been observed previously.

It is also pointed out that NMR experiments up to 8 kbar were carried out by Kushida and Murphy in the early 1970's [72]. They observed a linear increase of the NMR frequency shift by about +2 ppm/kbar in this pressure range. This observation will be addressed in more detail later.

4.1.2 Probing $N(E_F)$ of aluminum with NMR

In this section it will be reviewed how $N(E_F)$ of metallic aluminum can be probed via NMR. As already pointed out in sec. 2.1, nuclei with a spin $\boldsymbol{I}$ couple magnetically to electrons in their

[c] The first Brillouin zone, the smallest Wigner-Seitz-cell in $\boldsymbol{k}$-space, of a fcc-lattice is a truncated octahedron.
[d] The 10% decrease in the unit cell volume corresponds to a 10% increase in the Brillouin zone volume which will affect the Fermi surface.

environment via the hyperfine interaction

$$\mathscr{H}_{HF} = 2\gamma\hbar\mu_B \boldsymbol{I}.\left[\frac{\boldsymbol{l}}{r^3} - \frac{\boldsymbol{s}}{r^3} + 3\frac{\boldsymbol{r}\,(\boldsymbol{s}.\boldsymbol{r})}{r^5} + \frac{8}{3}\pi\boldsymbol{s}\delta(\boldsymbol{r})\right]. \tag{4.7}$$

In the case of metallic aluminum, the orbital term (1st term in eqn. (4.7)) is expected to be small as ^{27}Al is a light atom while the dipolar term (2nd and 3rd term) vanishes due to the cubic symmetry of the lattice[e]. Thus, only the s-contact interaction (4th term) has to be considered, which arises due to the coupling of the ^{27}Al nuclei to the electrons at E_F.

Knight-shift K

This coupling is most notably detected by a shift in the resonance frequency ν_0 with respect to the Larmor frequency ν_L. This shift is on the order of a fraction of a percent and can be expressed by

$$\nu_0 = (1+K)\nu_L. \tag{4.8}$$

A distinct shift in resonance frequency in a metal (copper) was first noticed by W. D. Knight [73] and K is commonly referred to as Knight-shift. If the shift originates only from the s-contact interaction, it is given by [15]

$$K = \frac{8\pi}{3}\mu_B^2\langle|\phi_{\boldsymbol{k}}(0)|^2\rangle_\mathrm{FS}N(E_\mathrm{F}), \tag{4.9}$$

where $\langle|\phi_{\boldsymbol{k}}(0)|^2\rangle_\mathrm{FS}$ is the probability of finding a conduction electron at the nucleus[f]. Note that $\chi_p = \mu_B^2 N(E_\mathrm{F})/V$ is the Pauli-susceptibility and that $\frac{8\pi}{3}\langle|\phi_{\boldsymbol{k}}(0)|^2\rangle_\mathrm{FS}V$ is referred to as a hyperfine coupling constant. Only s-states contribute to this interaction because of the non-vanishing probability to be at the nucleus. The other p-, d- or f-states may nevertheless contribute to the shift K (and T_1) via core polarization, that is significant in particular for transition metals. In the case of metallic aluminum, theoretical calculations however indicate that the effect of core polarization is small [74] and it will thus be neglected here.

Spin-lattice relaxation T_1

The s-contact interaction also greatly enhances the spin-lattice relaxation rate $1/T_1$ in metals. It was shown by Korringa [75] that, if other interactions can be neglected, T_1 and K are related to one another via the Korringa-relation

$$T_1 T K^2 = \frac{\hbar}{4\pi k_B}\frac{\gamma_e^2}{\gamma_n^2}. \tag{4.10}$$

[e] Due to the cubic symmetry of the lattice, the quadrupolar interaction should also vanish. However, at high pressure an increase in the linewidth of the ^{27}Al signal was observed that is ascribed to a small quadrupolar broadening. This will be discussed in more detail in sec. 4.3

[f] $\langle|\phi_{\boldsymbol{k}}(0)|^2\rangle_\mathrm{FS}$ is normalized to the unit cell volume.

Here, γ_e and γ_n denote the gyromagnetic ratios of the electron and the nucleus respectively. The Korringa-relation is particularly useful to examine the nature of the spin-lattice relaxation. A deviation from $T_1TK^2 = \text{const.}$ indicates that further relaxation processes have to be considered.

It should be noted that eqn. (4.10) does not take into account electron-electron interactions that enhance the Pauli-susceptibility [76] and T_1-processes [18]. To include these interactions, the right hand side of eqn. (4.10) has to be multiplied by a constant factor $\mathscr{K}$ that depends on the strength of the electron-electron interactions.

4.2 Experimental conditions

In this section, the experimental conditions of the high pressure NMR experiments will be briefly summarized.

For the experiments at high pressure, a variety of different moissanite anvil cells (MAC) were prepared according to sec. 3.1. The MACs were equipped with anvils of 1.0 mm culet diameter up to 42 kbar and 0.8 mm at higher pressure. Accordingly, up to 42 kbar microcoils with 10 turns and 300 µm diameter were used while for the experiments at higher pressures the dimensions of the microcoils were reduced to 9 turns and 200 µm diameter. Each microcoil was loaded with the same aluminum powder as in sec. 3.2.2 (purchased from Alfa Aesar, 99.97% purity and particle diameter of less than 44 µm) and contained a small chip of ruby for the determination of pressure via the ruby fluorescence method. An open MAC prepared in that way was already shown in fig. 3.6(b) on page 35. Daphne 7373 and Glycerin were employed as pressure transmitting media. Experiments at ambient pressure were carried out on a much larger sample of the aluminum powder mixed with epoxy using a conventional hand-wound coil.

The experiments at 73 kbar and higher pressure were carried out in the same MAC by progressively increasing its pressure up to 101 kbar. A MAC prepared in an earlier attempt to achieve similar pressures failed as its anvils cracked during application of pressure. This was possibly caused by a chemical reaction of the aluminum powder with the glycerin. Therefore, for experiments at 87 and 101 kbar, the MAC was cooled in liquid nitrogen prior to application of pressure in the hope of preventing the potential chemical reaction.

The NMR measurements were conducted at room temperature ($\sim$297 K) in static magnetic fields of 7.0, 11.7 and 17.6 T using homebuilt NMR probeheads. Additionally, ambient pressure datum was also recorded in a 16 T cold bore sweepable magnet. ^{27}Al ($I = 5/2$) spectra were acquired by recording the FIDs following a $\pi/2$-pulse of usually 2 µs duration. The $\pi/2$-pulse condition was determined by varying the pulse power P. Typically, the resonant circuit had a quality factor of $Q \approx 16$ at 130 MHz and maximum signal was found for $P_{\text{opt}} \approx 1$ W. Up to 63 kbar, 1024 scans were accumulated for the spectra. At 73 kbar and higher, the number of scans had to be increased to 1×10^6 because of a low signal-to-noise ratio. The resonance frequencies of these spectra were referenced to that of an aqueous solution of $AlCl_3$. At higher pressure (above 42 kbar) spin-echoes could be recorded using the Hahn-echo sequence $\pi/2$–τ–π.

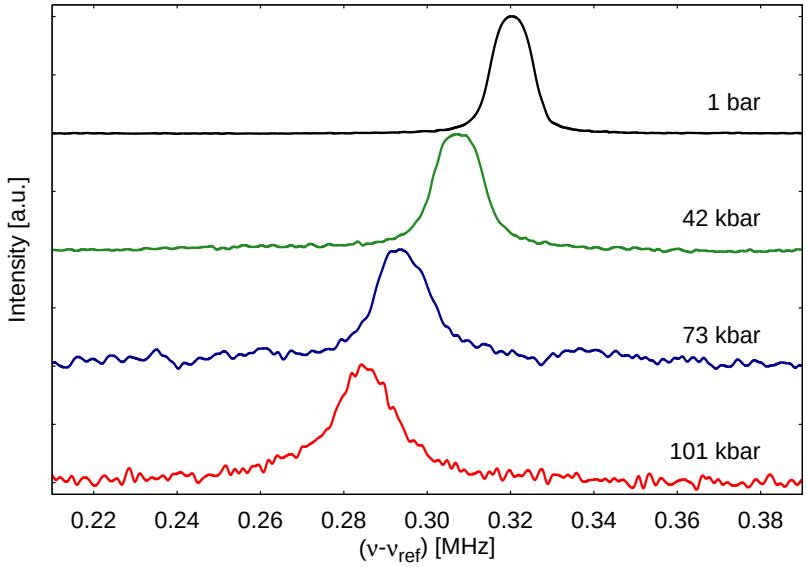

Figure 4.1: Sample spectra of metallic aluminum at selected pressures recorded in a magnetic field of 17.6 T. The spectra are shown in order of increasing pressure from top to bottom and frequencies have been referenced to that of an aqueous solution of $AlCl_3$ ($\nu_{ref} \approx 195.25$ MHz). With increasing pressure, the resonance frequency decreases while the linewidth increases.

The spin-lattice relaxation time T_1 was determined using the inversion recovery pulse sequence $\pi - \tau - \pi/2$ and the dephasing time of the FID T_{2G} was determined by fitting a Gaussian to it. All experiments were carried out with a last delay of 30 ms.

4.3 Results and discussion

Here, the experimental results of the high pressure NMR experiments will first be briefly summarized and then be discussed in more detail. Most notably, it will be shown that the change of the Knight-shift K with pressure cannot be understood in terms of the free electron model.

4.3.1 Sample spectra and FIDs

Signal from metallic aluminum was successfully observed up to a pressure of 101 kbar, exceeding the previously investigated pressure range of Kushida and Murphy [72] by a factor of 14. It should be noted that this is the second highest pressure at which NMR signals have been recorded in a gem anvil cell, surpassed only by Pravica and Silvera [39] who achieved 128 kbar in ^{1}H NMR experiments.

Fig. 4.1 shows a selection of sample spectra recorded at different pressures in a magnetic field of 17.6 T. The spectra clearly indicate that the resonance frequency of the ^{27}Al signal decreases with increasing pressure. This observation will be discussed in sec. 4.3.4 In addition, an increased linewidth is observed at 73 and 101 kbar, which will be addressed in sec. 4.3.3. Furthermore,

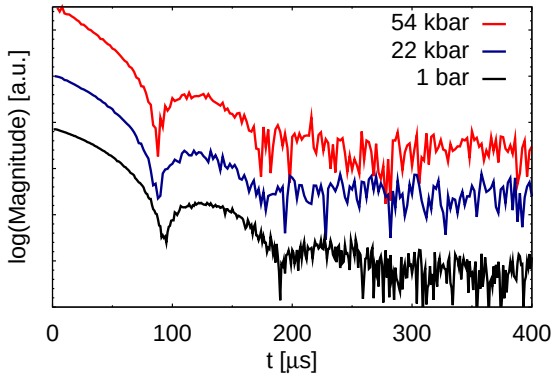

Figure 4.2: Logarithmic magnitude versus time t of selected FIDs recorded at ambient pressure (1 bar) and high pressure (22 kbar and 54 kbar) in a magnetic field of 11.7 T. The onset of beats is evident in the data up to a pressure of 54 kbar.

as shown in fig. 4.2, up to a pressure of 54 kbar the FIDs displayed a beat pattern that will be discussed first.

4.3.2 Beat-shape of FIDs

At ambient pressure, the shape of the FID and therefore the lineshape of metallic aluminum is known to be dominated by the homonuclear dipolar interaction [77, 78]. Note that this interaction affects the resonance frequency ν_0 of the nuclei only in such a way that the resonance line broadens. It is thus not associated with the decrease of ν_0 evident in fig. 4.1.

Characterization of beats

In the main panel of fig. 4.3, the magnitude of an ambient pressure FID (logarithmic scale) is plotted versus time t (it has a better SNR compared to the data shown in fig. 4.2). It was recorded at 99.6 MHz in a field of 9.0 T (sweepable magnet) and 100 K. Within the resolution of the experiments, this FID shape was found to be temperature and field independent. At short times, the FID is well described by a Gaussian decay

$$I(t) = I_0 \exp\left\{\frac{-t^2}{2T_{2\mathrm{G}}^2}\right\} \tag{4.11}$$

as is indicated by the blue dashed line in fig. 4.3. In the inset of fig. 4.3, $\log(I)$ vs. t^2 is plotted for the first 100 µs to emphasize the Gaussian shape of the FID. This behavior is expected for the dipolar interaction [17] and results in a second moment $\langle\Delta\nu^2\rangle$ [15] of

$$\langle\Delta\nu^2\rangle = \frac{1}{4\pi^2 T_{2\mathrm{G}}^2} = 20.26\ \mathrm{kHz}^2 \tag{4.12}$$

in good agreement with values found in the literature (see [77] and references therein).

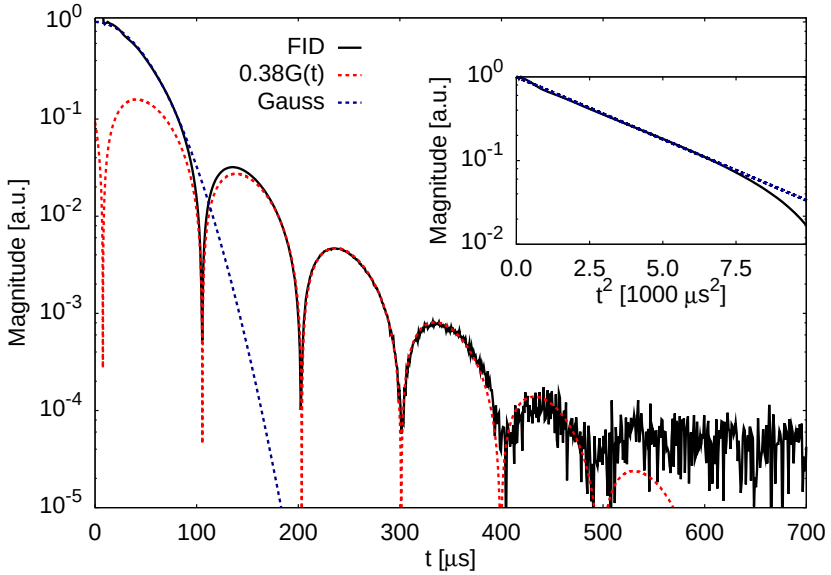

Figure 4.3: Logarithmic magnitude (black) versus t of the 1 bar FID recorded at 99.6 MHz and 100 K. Also shown are the fitted function $G(t)$ (red) and a Gaussian decay according to eqn. (4.11) (blue). (Inset) Logarithmic magnitude versus t^2 of the same FID for times $t \leq 100$ µs to emphasize the Gaussian shape of the FID at short times. For both plots, $t = 0$ corresponds to the center of the $\pi/2$-pulse.

However, the long time behavior of the FID is clearly non-Gaussian and displays characteristic beats. At sufficiently long times, it is described by

$$G(t) = \exp\{-\gamma t\} \cos(\omega t + \Phi) \tag{4.13}$$

as indicated by the red dashed line in fig. 4.3. It should be noted that all atomic sites in metallic aluminum are identical due to the symmetry of the fcc-lattice. The beat shape thus cannot be caused by a shift in resonance frequency of one site. Fitting eqn. (4.13) to the ambient pressure datum for times t: 200 µs $\leq t \leq$ 400 µs yields values of $\gamma = 0.018$ µs^{-1}, $\omega = 0.0321$ radµs^{-1} and $\Phi == \pi/2.375$. The FID in fig. 4.3 has not been corrected for field inhomogeneities and T_1. Correcting for these effects will increase γ slightly.

It is worth mentioning that in order to be able to observe the beat shape, it is necessary to record the FID over multiple orders of magnitude. High pressure data of considerably better SNR would be required to discuss the pressure evolution of these beats which was beyond the scope of this thesis. Nonetheless, the onset of the beats could be observed up to a pressure of 54 kbar as already shown in fig. 4.2. Beyond 54 kbar, no beats were observed which could be due to a lack of the available signal-to-noise or caused by a suppression of the beats at higher pressure.

Comparison to beats in other materials

The existence of beats in the FID of metallic aluminum was already mentioned by Spokas and Slichter [77]. However, they were not further characterized in the before-mentioned article. Very similar beats that are also described by eqn. (4.13), albeit with different factors γ, ω and Φ, can also be observed in the long-time behavior of ^{19}F-NMR in CaF_2 [79] and ^{129}Xe-NMR in hyperpolarized solid xenon [80] for example. In these materials, the shape of the FID is also dominated by the homonuclear dipolar interaction of the nuclear spins that reside on a rigid lattice. As the FIDs in these materials are well described by a Gaussian shape at short times, the beats indicate a transition to a distinct long time behavior.

What makes the observation of beats in metallic aluminum interesting is that, unlike ^{19}F and ^{129}Xe which are spin-1/2 nuclei, ^{27}Al is a spin-5/2 nucleus and therefore subject to potential quadrupole interaction. While such interactions should in principle vanish in metallic aluminum due to the cubic symmetry of the lattice, a small quadrupolar contribution to the signal decay has been found at ambient pressure [77] and, as will be shown below, becomes increasingly important at higher pressure. In fact, it cannot be ruled out that the quadrupolar interaction suppresses the beats at very high pressure (> 54 kbar). Furthermore, the nuclear spins in metallic aluminum are not isolated, as is the case in CaF_2 and solid xenon, but interact with the electrons at E_F through the hyperfine coupling. As a result of this interaction, the spin-lattice relaxation time T_1 is comparably short with a value of 6.3 ms at ambient pressure and room temperature. It is thus a rather surprising result to observe beats in metallic aluminum.

Different theoretical models have been put forward to explain the occurrence of the beats and their shape according to eqn. (4.13) [16, 81]. In the model of Fine [16] that appears favorable because of its agreement with recent experiments on CaF_2 [82], the observed beats correspond to the slowest decaying mode due to the random orientation of the powder. The observation of beats in metallic aluminum in general and under such extreme pressure conditions in particular might put additional constrains on these models. It would certainly be of interest to investigate these beats further but this is beyond the scope of the present thesis.

4.3.3 Pressure evolution of the linewidth

The pressure evolution of the linewidth of the ^{27}Al-spectra will be discussed next. Fig. 4.4(a) shows the pressure dependence of the full width at half maximum (FWHM) of the spectra recorded at 17.6 T (some of them are shown in fig. 4.1). Up to and including 42 kbar, the FWHM remains more or less pressure independent with a value of about 11 kHz but then increases continuously up to 18 kHz at 101 kbar.

Dipolar linewidth

In the case of pure dipolar broadening (DB), the FWHM is given by [15]

$$\mathrm{DB} = 2\sqrt{2\ln 2}\langle \Delta\nu^2 \rangle^{1/2}, \tag{4.14}$$

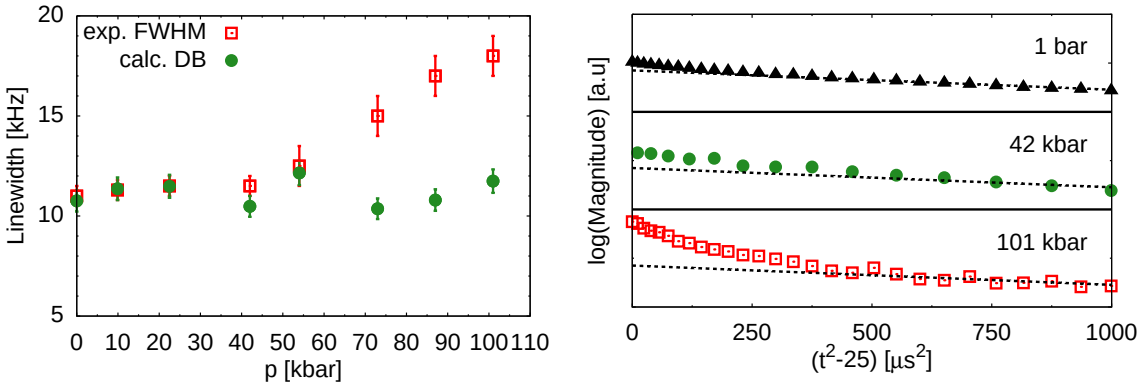

(a) FWHM and dipolar contribution

(b) FIDs at 11.7 T at different pressures

Figure 4.4: (a) Pressure dependence of the experimentally determined FWHM (⊡) and the calculated dipolar broadening (DB) (●) of the metallic aluminum spectra recorded at 17.6 T. (b) Logarithmic magnitude versus t^2 for FIDs recorded at 11.7 T at various pressures ($t^2 = 0$ corresponds to the center of the $\pi/2$-pulse). The y-scale of each FID represents two orders of magnitude. Dashed lines are a guide to the eye and indicate the dipolar decay of Gaussian shape.

where $\langle \Delta\nu^2 \rangle$ is the second moment as defined in eqn. (4.12). At ambient pressure, this yields a value of 10.6 kHz in good agreement with the value found experimentally. Based on the volume change determined by X-ray diffraction experiments [67], one expects an increase of the dipolar linewidth by about 10% up to 101 kbar, since $\mathscr{H}_\mathrm{D} \propto 1/r^3$. This is clearly insufficient to account for the observed increase of the FWHM by 60% at 101 kbar and points to an additional contribution to the lineshape.

In fig. 4.4(b), the logarithmic magnitude of FIDs recorded at various pressures at 11.7 T are plotted versus t^2. It is evident that at short times the FIDs recorded at high pressure deviate from a Gaussian decay that is expected for a purely dipolar broadening. In fact, this is even true at ambient pressure, albeit to a very small degree. The magnitude of the effect increases with pressure. Note that this cannot be caused by coil "ringing" as the ringdown time of the circuit $t_\mathrm{r} = Q/(\pi\nu_0)$ is well below 1 µs.

After $t^2 > 400$ µs^2, the additional decay is negligible and the FID is described by a single Gaussian. This enables one to extract $T_{2\mathrm{G}}$ from eqn. (4.11) and determine the dipolar linewidth via eqn. (4.14). It is compared to the experimental FWHM in fig. 4.4(a) and agrees well with the FWHM up to about 54 kbar. However, at higher pressure the dipolar linewidth remains more or less pressure independent, in agreement with the expected behavior, while the FWHM increases significantly. A pure dipolar broadening is therefore insufficient to explain the increased linewidth at high pressure.

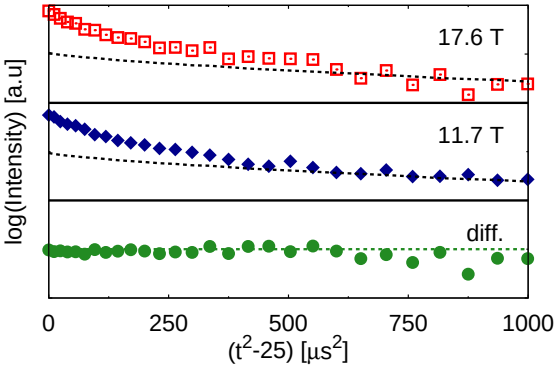

(a) B_0-dependence of FIDs at 101 kbar

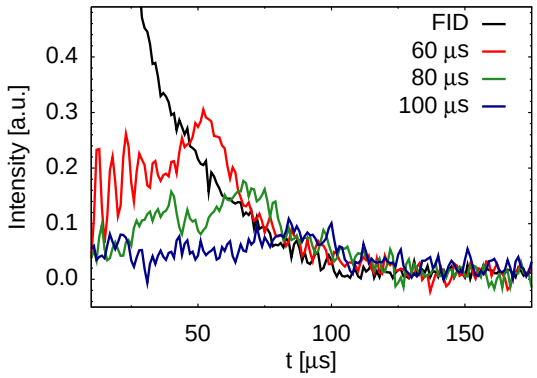

(b) Hahn echo decay at 54 kbar

Figure 4.5: (a) FIDs at 101 kbar (symbols) and for comparison at 1 bar (dashed lines) at 17.6 T (top), 11.7 T (middle) and the difference of both magnetic fields ($t=0$ corresponds to the center of the $\pi/2$-pulse). The y-scale of each FID represents two orders of magnitude. (b) Hahn echo decay observed at 54 kbar in a magnetic field of 11.7 T. The pulse separation τ of the echoes was varied from 60 µs to 100 µs.

Field dependent measurements

To shed some light on the origin of the additional linebroadening, field dependent measurements were carried out. In principle, there are two possible explanations for the increase of the FWHM: it is either (a) a magnetic broadening, i.e. due to a distribution of shifts, or (b) a quadrupolar broadening. In the case of magnetic broadening, the effect would scale with B_0 while for quadrupolar broadening it depends on wether it is a first or second order perturbation effect. If it is a first order effect, i.e. a broadening caused by a small shift in resonance frequency $\delta\nu_m^{(1)}$ of the satellite transitions $(m-1/2) \leftrightarrow m$ $(m \neq 1/2)$, it would be independent of B_0 whereas a second order effect, i.e. a broadening due to a distribution of $\delta\nu_{1/2}^{(2)}$, would scale with $1/B_0$.

As an example for these measurements, the FIDs recorded at 101 kbar (and 1 bar for comparison) in magnetic fields of 11.7 T and 17.6 T are displayed in fig. 4.5(a) in a $\log(I)$ vs. t^2 plot. Within the resolution of the experiments, the FIDs and therefore the shape of the spectra are found to be independent of B_0. It can thus be concluded that the additional broadening must be first order quadrupolar in origin. Note that a second order quadrupole effect would also shift the resonance frequency ν_0 of the ^{27}Al signal. That this is not the case is evident from fig. 4.6 that will be discussed in detail further below.

If the additional broadening is of quadrupolar origin it should also be possible to excite a weak Hahn echo that is absent for pure dipolar coupling [83]. Indeed, Hahn echoes could be observed at high pressure as shown for 54 kbar in fig. 4.5(b) whereas none were found at ambient pressure. This is further proof that the additional broadening is of quadrupolar origin. Under the assumption that quadrupolar (QB) and dipolar broadening (DB) contribute independently

to the FWHM, i.e.

$$\mathrm{FWHM} = \sqrt{\mathrm{DB}^2 + \mathrm{QB}^2} \tag{4.15}$$

it can be estimated that the quadrupolar broadening is about 13.5 kHz at 101 kbar, which is its largest value in the investigated pressure range.

Given the cubic symmetry of the fcc-lattice, in which an electric field gradient is expected to vanish due to the local symmetry, the occurrence of a quadrupolar broadening is rather surprising. One possible explanation is that it is induced by crystal imperfections that can arise from pressure inhomogeneities. Such inhomogeneities are not unexpected as the hydrostatic pressure limits of the pressure transmitting media Daphne 7373 and Glycerin were exceeded and the ruby spectra at 87 kbar and 101 kbar, in fact showed a broadening of the ruby line indicating a pressure distribution. However, as the magnitude of the nuclear quadrupole moment of ^{27}Al is relatively large, one would rather expect a second order quadrupole effect similar to quenched copper metal [84]. Another possible explanation of the quadrupolar broadening is the occurrence of a charge density wave in the vicinity of a Lifshitz-transition [85] which would cause a local electric field gradient at the nucleus.

Further experiments are required to understand the origin of the additional quadrupolar broadening. Nevertheless, the effect is small and its presence does not affect the resonance frequency of the ^{27}Al spectra within the resolution of the experiments.

Reduction of signal intensity at high pressure

It is pointed out here that the data recorded at 73 kbar and higher pressure had a signal-to-noise ratio that was significantly smaller than expected (this is also evident from the noise level of the high pressure data in fig. 4.1). A similar effect was also observed in our very first experiments on metallic aluminum at a pressure of ~ 70 kbar that were published in [52]. In the beforementioned article it was argued that the reduced signal intensity was at least partially caused by a second order quadrupole effect in which case only the central transition would be observed with an intensity of 9/35 of the total signal. However, the preceding analysis shows that this was likely not the case.

Instead, it is possible that at least to some extent the intensity loss is caused by short-circuiting coil turns at high pressure as indicated by the rather low resistance of the microcoil of $r \approx 1\ \Omega$. This can be prevented in the future by reducing the initial number of turns. In addition, it cannot be ruled out that a significant amount of the aluminum powder chemically reacted with the pressure medium during pressurization.

4.3.4 Pressure dependence of K and T_1

In the following discussion, the experimentally observed pressure dependence of the Knight-shift $K = (\nu_0 - \nu_L)/\nu_L$ and the spin-lattice relaxation time T_1 will be discussed. The experimental

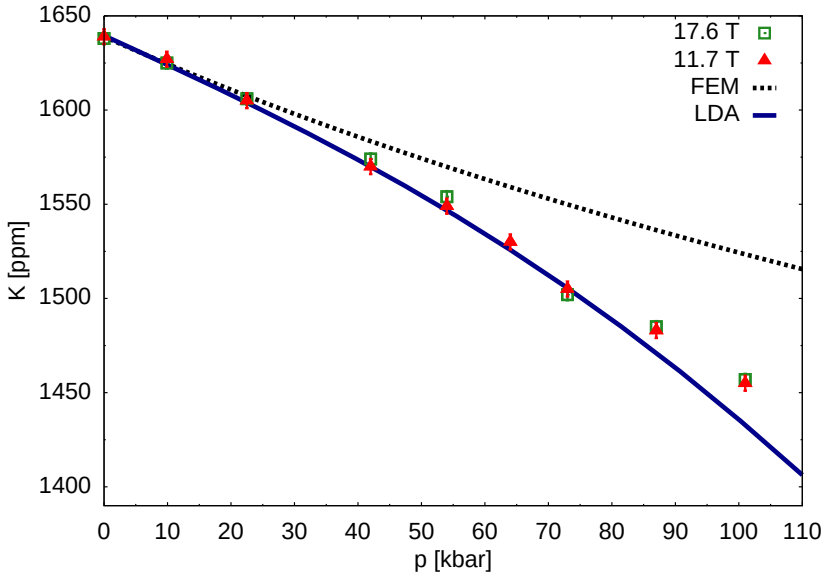

Figure 4.6: Pressure dependence of $K(p)$ measured at 17.6 T (⊡) and 11.7 T (▲). The dashed line (▪▪▪) indicates the expected pressure dependence of $K(p)$ for the free electron model (FEM) under the assumption that the hyperfine coupling, i.e. $\langle|\phi_{\boldsymbol{k}}(0)|^2\rangle_{\mathrm{FS}}$, is pressure independent. The blue line (▬) shows the numerically calculated pressure dependence of $N_{3\mathrm{s}}(E_{\mathrm{F}}, 300\ \mathrm{K})$ normalized to the ambient pressure value of $K(1\ \mathrm{bar}) = 1640$ ppm (see sec. 4.4 for details).

results will be compared to the free electron model.

For a particular pressure and magnetic field strength B_0, the resonance frequency ν_0 of the aluminum spectrum was determined by fitting the Gaussian distribution

$$f(\nu) = A \exp\left\{-\frac{(\nu-\nu_0)^2}{2\sigma^2}\right\} \tag{4.16}$$

to the spectrum in the vicinity of the spectral maximum. This allowed the determination of ν_0 well within an estimated ±0.5 kHz (this value was used for determining the uncertainty of K). The Larmor-frequency ν_L was assumed to be given by the resonance frequency ν_{ref} of the reference, an aqueous solution of $AlCl_3$[g]. At ambient pressure, $K = 1640$ ppm was measured in good agreement with the value found in the literature [78].

The pressure dependence of the Knight-shift K at 11.7 T and 17.6 T is shown in fig. 4.6. $K(p)$ is found to decrease smoothly from 1640 kbar at ambient pressure down to 1455 ppm at 101 kbar which corresponds to a total reduction of K by 11%. At the same time, $K(p)$ has a negative curvature and the rate dK/dp changes from -1.5 ppm/kbar at low pressure to -2.0 ppm/kbar at high pressure. Note that within the precision of the experiments, $K(p)$ is found to be independent of the applied field B_0 which is consistent with the previous conclusion

[g]During the first experiments at high pressure it was observed that the resonance frequency of a sample was slightly affected by the presence of the MAC holder. Thus, to prevent systematic errors, the reference frequency was always measured using the same probehead with the MAC holder mounted on top. Note that, as already pointed out in sec. 3.2, ν_0 is not affected by the presence of the MAC.

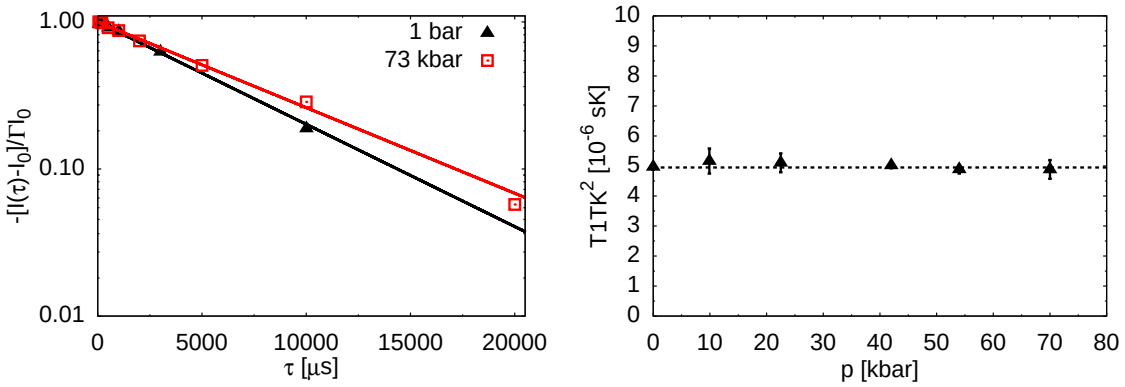

(a) T_1 fit at 1 bar and 73 kbar

(b) T_1TK^2 as a function of pressure

Figure 4.7: (a) $-[I(\tau)–I_0]/\Gamma I_0$ as a function of the pulse separation time τ following the inversion recovery sequence $\pi-\tau-\pi/2$ recorded at ambient pressure (▲) and 73 kbar (⊡). Note that the change in slope from 1 bar to 73 kbar is due to the increase of T_1 with pressure. (b) Korringa factor T_1TK^2 as a function of pressure. The dashed line is a guide to the eye.

that a second order quadrupolar shift can be neglected in the interpretation of the $K(p)$ data.

It is pointed out here that the low pressure rate of –1.5 ppm/kbar is not in agreement with an earlier NMR study by Kushida and Murphy up to 8 kbar [72] where an increase of $K(p)$ at a rate of +2.0 ppm/kbar was observed. Given the general trend of $K(p)$ observed in fig. 4.6, it is unlikely that a drop of 30 ppm occurs between 8 kbar (highest pressure in [72]) and 10 kbar (lowest pressure point of the present study). I am not in a position to speculate why the data of [72] disagrees with the present work. However, our $K(p)$ data is consistent both with the T_1 results (see below) and the numerical calculations discussed in sec. 4.4.

The spin-lattice relaxation time T_1 was also measured at 11.7 T and room temperature (297 K) up to a pressure of 73 kbar. As expected, the T_1-relaxation following the inversion-recovery sequence $\pi-\tau-\pi/2$ was found to be described by a mono-exponential decay (non-selective excitation)

$$I(\tau) = I_0 \left[1 - \Gamma \exp\left\{-\frac{\tau}{T_1}\right\}\right]. \tag{4.17}$$

In fig. 4.7(a), $-[I(\tau)-I_0]/\Gamma I_0$ vs. t recorded at 1 bar and 73 kbar are shown as examples. At ambient pressure, the T_1 value of 6.28 ± 0.05 ms yields $T_1T = 1.85$ sK in good agreement with earlier studies [77][h]. While T_1 increases with pressure, the Korringa relation T_1TK^2 is found to be pressure independent, c.f. fig. 4.7(b). Thus, it can be concluded that the changes of K and T_1 under pressure indeed originate from the coupling to the conduction electrons and no other effects have to be taken into consideration.

[h] This value of T_1T is known to be temperature independent from 1 K up to the melting temperature of aluminum of 930 K [77].

Comparison to the free electron model

Recalling that the Knight-shift K is given by

$$K = \frac{8\pi}{3}\mu_B^2 \langle|\phi_{\boldsymbol{k}}(0)|^2\rangle_{\mathrm{FS}} N(E_{\mathrm{F}}), \tag{4.18}$$

it is clear that the observed pressure dependence of K can only be caused by changes in the density of states $N(E_{\mathrm{F}})$ and/or $\langle|\phi_{\boldsymbol{k}}(0)|^2\rangle_{\mathrm{FS}}$. The latter however is not expected to vary much in the pressure range investigated as it would imply a significant distortion of the wave functions accompanied by a significant change in the energy E of the system[i]. Thus, the observed decrease in $K(p)$ must originate from changes in $N(E_{\mathrm{F}})$.

In the free electron model, the density of states varies with the pressure dependent volume $V(p)$ of the unit cell according to $N(E) \propto V(p)^{2/3}$. Therefore, neglecting small changes in the hyperfine coupling ($\langle|\phi_{\boldsymbol{k}}(0)|^2\rangle_{\mathrm{FS}}$) one expects $K(p)$ to vary with $V(p)^{2/3}$ as well. The experimentally applied pressure can be related to $V(p)$ via the third-order Birch-Murnaghan isothermal equation of state [86]

$$p(v) = \frac{3}{2}B\left(v^{-\frac{7}{3}} - v^{-\frac{5}{3}}\right)\left[1 - \frac{3}{4}\left(4 - B'\right)\left(v^{-\frac{2}{3}} - 1\right)\right], \tag{4.19}$$

where $v = V(p)/V(0)$ denotes the relative change of $V(p)$ compared to its ambient pressure value $V(0)$. The bulk modulus $B = 727 \pm 30$ kbar and its pressure derivative $B' = dB/dp = 4.3 \pm 0.8$ are known from X-ray experiments [67].

In fig. 4.6, the expected pressure dependence of $K(p)$ for the free electron model, under the assumption that $\langle|\phi_{\boldsymbol{k}}(0)|^2\rangle_{\mathrm{FS}} = \text{const.}$, is plotted (the ambient pressure point of $v(p)$ was normalized to $K(1\text{ bar})$). Similar to the experimental data, $K(p)$ in the free electron model decreases with increasing pressure and the agreement is good up to 20 kbar. However, at higher pressure the experimentally determined Knight-shift decreases significantly faster than expected. At 101 kbar, the drop in $K(p)$ is almost three times than what is expected for a free electron behavior. Thus, unless $\langle|\phi_{\boldsymbol{k}}(0)|^2\rangle_{\mathrm{FS}}$ decreases by 7% in the pressure range, which is unlikely as mentioned above, it can be concluded that the high pressure data cannot be understood in terms of the free electron model.

4.4 Numerical calculations

In order to determine the origin of the pressure dependence of $K(p)$, we approached Dr. Helmut Eschrig, Dr. Manuel Richter and Dr. Klaus Koepernik from the Leibniz Institute for Solid State

[i] Expressed in the basis of the atomic wave functions, a distortion of the wave functions $\psi_{n\boldsymbol{k}}$ results in a change of the fraction of the different s-, p-, d- and f-contributions. As the different atomic wave functions vary considerably in energy E, the distortion would imply a significant change in the energy E of $\psi_{n\boldsymbol{k}}$. The numerical calculations discussed in sec. 4.4 indeed show that $\langle|\phi_{\boldsymbol{k}}(0)|^2\rangle_{\mathrm{FS}}$ changes only by 0.4% in the pressure range investigated. It is therefore justified to neglect it.

and Materials Research Dresden. They carried out band structure calculations that revealed that the decrease of $K(p)$ can be understood in terms of a Lifshitz transition at about 75 kbar.

Details of the calculations

The numerical calculations were carried out with the full-potential local-orbital scheme FPLO-9.00-34 [87] using the local density approximation (LDA) Perdew-Wang 92 [88] and a scalar-relativistic mode. The density of states was evaluated by linear-tetrahedron integrations with Blöchl corrections [89] on a mesh of $300 \times 300 \times 300$ points in the full Brillouin zone. This extremely fine mesh of points was necessary to achieve the required accuracy of the DOS close to singularities.

The DOS was calculated for various lattice constants ranging from 3.66 to 4.00 Å at the temperature $T = 0$ K. In order to determine to what extent s-states contribute to $N(E)$, the composition of the wave vector $\boldsymbol{k}$ was analyzed via atomic-like wave functions beyond a minimum basis set. In the present case, the valence basis comprised 2s, 2p, 3s, 3p, 3d, 4s and 4p atomic states. The equation-of-state $p(v)$ was obtained from a standard Birch-Murnaghan fit of the internal energy U resulting in a zero-pressure unit cell volume of 15.831 Å^3 per atom, a bulk modulus of $B = 837$ kbar and a pressure derivative of $B' = 4.4$[j].

4.4.1 Results and discussion

In this section, the results of the numerical calculations will be briefly summarized and discussed in terms of their implications for the pressure evolution of $K(p)$.

Pressure dependence of $N(E)$

Fig. 4.8(a) shows the numerically calculated total electronic density of states $N(E)$ as a function of E at zero LDA-pressure (corresponds to ambient pressure in the experiment). From the band bottom at about $E_{\mathrm{min}} - E_{\mathrm{F}} =$ -11.5 eV to approximately -5 eV, $N(E)$ displays an almost perfect free electron behavior with $N(E) \propto \sqrt{E - E_{\mathrm{min}}}$. However, from -5 eV to about 1.2 eV and therefore close to the Fermi level E_{F}, a number of van Hove-singularities appear.

In fig. 4.8(b), $N(E)$ is displayed at higher resolution in the vicinity of E_{F} at zero LDA-pressure and various LDA-pressures up to 100 kbar (the van Hove-singularities in this range are of interest for the pressure evolution of the Knight-shift discussed in the present thesis). At zero LDA-pressure, two strong singularities are observable in the occupied part of the band at -0.42 eV (labeled 'a' in the figure) and -0.04 eV (labeled 'b'), and a weaker singularity is found in the unoccupied part at about 0.14 eV (labeled 'c'). Upon application of pressure, $N(E)$ decreases for all energies in the interval shown and the positions of the singularities change:

[j] The internal energy U is related to pressure and the volume change via $dU = TdS - pdV$. Assuming that the entropy S is constant, U is then given by $U = U_0 - \int pdV$, where p is assumed to be given by eqn. (4.19). The parameters V_0 (volume at $U = U_0$), B and B' are then varied to optimally fit the $U(V)$-values. Note that the numerically calculated bulk modulus $B = 837$ kbar is somewhat larger than the experimentally found value of 727 kbar.

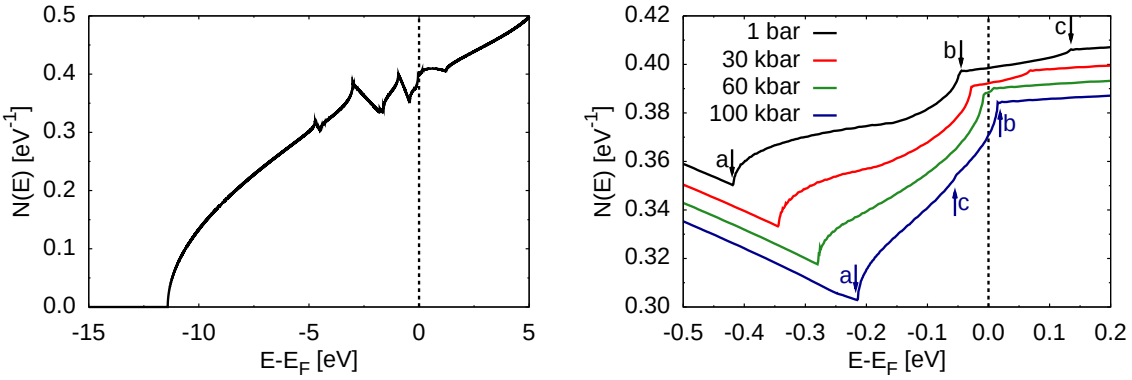

(a) $N(E)$ at 1 bar

(b) $N(E)$ at various pressures

Figure 4.8: (a) The zero LDA-pressure density of states $N(E)$ as a function of energy E. (b) $N(E)$ in the vicinity of E_F at various LDA-pressures up to 100 kbar. The position of the three van Hove-singularities (labeled a, b, c) at zero and 100 kbar LDA-pressure are indicated by arrows. In both figures, the dashed line denotes the Fermi level E_F.

the two singularities 'a' and 'b' move to higher energies while singularity 'c' moves to lower energies. Between 60 and 100 kbar, the singularities 'b' and 'c' cross the Fermi level E_F, each inducing a Lifshitz transition, while the third singularity 'a' crosses E_F not until much higher LDA-pressures of 240 to 260 kbar (not shown).

Pressure dependence of $N_{3s}(E_\mathrm{F})$

The total calculated DOS comprises of s-, p- and d-states whereas the Knight-shift K in aluminum is only susceptible to electrons that are in a s-state due to their non-vanishing probability to be at the nucleus. One is therefore primarily interested in the contribution of s-states to $N(E_\mathrm{F})$. The predominant contribution to $N(E_\mathrm{F})$ arises from 3s-states. Additionally, a small contribution from 4s-states occurs at higher pressure (see text below) whereas semicore 2s and core 1s contributions are found to be negligible.

In fig. 4.9, the pressure dependence of $N_{3s}(E_\mathrm{F})$, i.e. the part of $N(E)$ that is in a 3s-state, is shown up to a LDA-pressure of 300 kbar. Two critical points occur at about 75 kbar and 250 kbar which are related to the two stronger van Hove-singularities 'a' (250 kbar) and 'b' (75 kbar). $N_{3s}(E_\mathrm{F})$ vs. p has a kink at these points and the slope changes significantly. Note that the transition of 'c' is not resolved in this figure: it almost merges with the singularity at 75 kbar from 'b'. Below 75 kbar and above 250 kbar, the pressure dependence of $N_{3s}(E_\mathrm{F})$ is weak, whereas it is considerably stronger in between. In total, $N_{3s}(E_\mathrm{F})$ is found to decrease by almost a factor of 3 from 0.104 states/eV at zero pressure down to 0.036 states/eV at 300 kbar.

When comparing $N_{3s}(E_\mathrm{F})$ with the experimental NMR-data, it is necessary to take into account that the NMR measurements were carried out at room temperature whereas the calculated $N_{3s}(E_\mathrm{F})$ corresponds to $T=0$ K. Therefore, $N_{3s}(E)$ was folded with the magnitude of the first

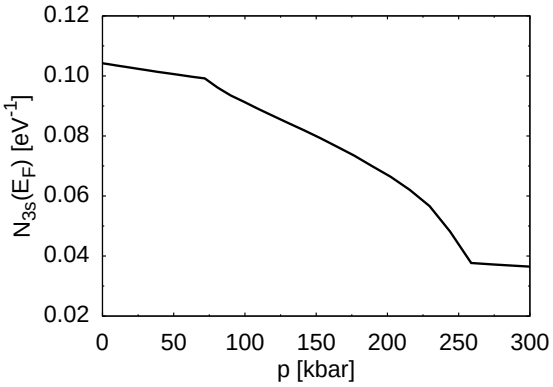

Figure 4.9: Pressure dependence of $N_{3s}(E_F)$. Two kinks in $N_{3s}(E_F)$ occur at about 75 and 250 kbar. They are caused by the Lifshitz-transitions induced by the two stronger van Hove-singularities that are at -0.04 eV and -0.12 eV at zero LDA-pressure. The third singularity is not resolved in this figure (its Lifshitz-transition almost merges with the one at 75 kbar).

derivative of the Fermi-Dirac function

$$\left|\frac{df}{dE}\right| = \frac{1}{k_B T} \frac{\exp\left\{\frac{E-E_F}{k_B T}\right\}}{\left(\exp\left\{\frac{E-E_F}{k_B T}\right\}+1\right)^2} \tag{4.20}$$

for $T = 300$ K, yielding a 300 K-folded $N_{3s}(E_F, 300\text{ K})$. The resulting theoretical pressure dependence is included in fig. 4.6 where the zero pressure point of $N_{3s}(E_F, 300\text{ K})$ was normalized to the experimental value of $K(1\text{ bar}) = 1640$ ppm (changes in the hyperfine coupling, i.e. $\langle|\phi_{\boldsymbol{k}}(0)|^2\rangle_{FS}$, are neglected). At room temperature, the distinct kink in $N_{3s}(E_F)$ vs. p at 75 kbar is smoothed out and the theoretical and experimental data match almost perfectly with only small deviations at very high pressure. Note that, if a 4s contribution is also taken into account, the high-pressure side of the theoretical curve in fig. 4.6 shifts up by about 6 ppm and therefore even closer to the experimental data. This means that $\langle|\phi_{\boldsymbol{k}}(0)|^2\rangle_{FS}$ increases by 0.4% at 100 kbar compared to its zero LDA-pressure value which justifies that it was neglected in the previous discussion.

The excellent agreement between the numerical calculations and the experimental data shows that the observed pressure dependence of $K(p)$ is caused by a shifting of the van Hove-singularities under pressure and that pressure drives the system through a Lifshitz-transition around 75 kbar. This is quite remarkable as such transitions are normally only observable at low temperatures ($K(p)$ should approach the theoretical pressure dependence of $N_{3s}(E_F)$ at lower temperatures[k]). However, the NMR data taken on a large enough pressure interval allow the detection of the

[k]Unfortunately, we became aware of the importance of the van Hove-singularities for $K(p)$ not until after finishing the NMR-experiments and the measurements were thus not carried out at low temperatures. Furthermore, without a suitable pressure gauge at low temperature (note that the ruby line splits into a complicated multiplet in an applied magnetic field, thus hampering pressure determination via ruby fluorescence in static magnetic fields) it was thought to be unfeasible to carry out the experiments at temperatures close to 4.2 K *and* determine the pressure precisely.

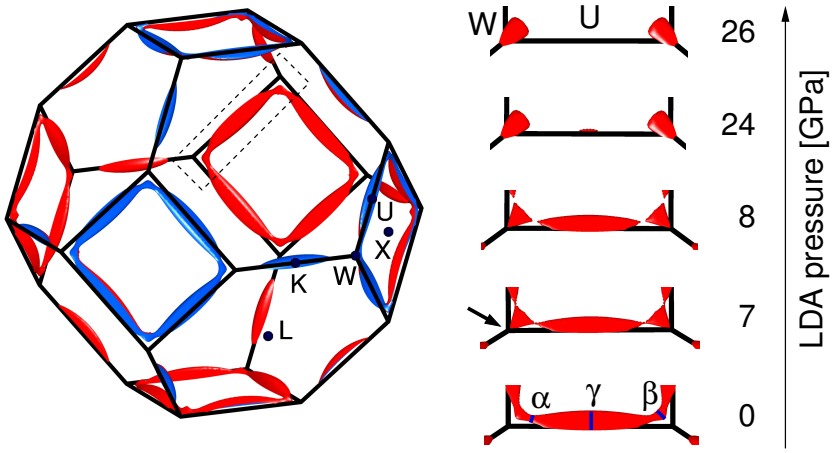

Figure 4.10: Numerically calculated Fermi surface of metallic aluminum (from [58]). Blue and red indicate the occupied and unoccupied side of the FS. (Left) The well-known third-zone surface of metallic aluminum at zero LDA-pressure in a reduced-zone scheme (1st Brillouin zone). (Right) Selected detail of the FS at various LDA-pressures with the pressure indicated on the right-hand side. Note that in this figure, GPa is used as the unit of pressure (1 GPa = 10 kbar). At zero LDA-pressure, the view is identical to the framed part on the left side. Extremal orbits are indicated in the common notation according to [90]. Between 7 and 8 GPa (70 and 80 kbar), the α-orbit vanishes whereas the γ-orbit vanishes between 24 and 26 GPa (240 and 260 kbar).

Lifshitz-transition even at room temperature.

4.4.2 Topology of the Fermi surface

As indicated in sec. 4.1.1, a Lifshitz-transition is related to a change in the topology of the Fermi surface. It is therefore worthwhile to take a look at the shape of the FS under pressure. Fig. 4.10 shows the pressure evolution of the third-zone surface (in a reduced-zone scheme) and illustrates the origin of the Lifshitz-transition (figure taken from [58]). Note that the pressure in the displayed figure is in GPa (1 GPa = 10 kbar).

First of all it is pointed out that the first Brillouin zone of metallic aluminum is a truncated octahedron due to the fcc-lattice structure. The surface of the Brillouin zone is hence constructed by 6 squares (centered around X-points) that are connected via 8 regular hexagons (centered around L-points). At zero LDA-pressure, the FS is a complex structure of narrow tubes that stretch along the sides of the squares and hexagons. The tubes along the squares, which are characterized by three extremal orbits α, β, and γ, are connected and form a "ring" structure.

At about 70 kbar, this ring has developed spikes that touch the W-point (arrow on the right side of fig. 4.10). As another spike touches W from the neighboring Brillouin zone, the FS becomes multiply connected at this Lifshitz-transition [91]. This change in topology is related to the small van Hove-singularity 'c' and creates only a small change in the DOS that is not visible in the Knight-shift. Just slightly above 70 kbar the "ring" structure breaks into parts as the α-orbit vanishes and $N_{3s}(E_F)$ vs. p shows the before-mentioned downward-kink. As already

pointed out above, this Lifshitz-transition is related to the singularity labeled 'b' and causes the observed negative curvature of $K(p)$. A continued increase of the pressure lets the tubes around U shrink further until they vanish in another Lifshitz-transition at about 250 kbar caused by singularity 'a'. This should cause an upward-kink in $N_{3s}(E_F)$ that should manifest itself in a positive curvature of $K(p)$ at $\sim$250 kbar. However, such high pressures could not be reached in our NMR experiments yet.

4.5 Conclusions

To conclude, NMR experiments on metallic aluminum up to a pressure of 101 kbar were performed that extend the pressure range previously investigated by a factor of 14 [72]. Up to 54 kbar, the FID of the NMR signal showed a beat pattern that is characteristic for homonuclear dipolar interactions and that can be explained in terms of properties of chaotic many-body quantum systems [80]. Above about 42 kbar, an increase in the NMR linewidths was observed that is inconsistent with a pure dipolar broadening. Supported by an extensive study of the field dependence of this effect it is concluded that the additional linewidth is independent of B_0 and it is ascribed to a small quadrupole broadening. This weak quadrupole coupling may be caused by strain or a manifestation of a charge density variation that breaks the cubic symmetry; further experiments are necessary to determine the origin of this effect more clearly.

However, most notably a decrease of the Knight-shift by 11% was found in this pressure range. This is almost three times of what is expected for a free electron system. As the pressure dependent shift is magnetic and the Korringa relation does not change with pressure, the observed decrease in $K(p)$ (and increase of $T_1(p)$) is ascribed to changes in the electronic density of states. Based on numerical band structure calculations that are in excellent agreement with the experimental data it is concluded that the pressure dependence of $K(p)$ and $T_1(p)$ is due to a kink in the electronic density of states at a Lifshitz-transition at about 75 kbar. It is predicted that an increase in pressure up to 300 kbar will result in a further drop in the Knight-shift by more than a factor of 2.

5 Pressure and the Pseudogap

After successfully conducting the high pressure NMR experiments on metallic aluminum, we were confident to apply our GAC-NMR design to investigate a more complex system. Motivated by the question: "What happens to the pseudogap of a high temperature superconductor under pressure?", we decided to study the cuprate $YBa_2Cu_4O_8$ (Y1248) at high pressures of up to 63 kbar.

This chapter is intended as a brief introduction to these experiments and will start with a description of the electronic phase diagram of the cuprates. Afterwards, it will be reviewed what informations may be gained from NMR shift measurements and it will be illustrated how the pseudogap manifests in the temperature dependence of the spin shift. Finally, some of the relevant properties of the investigated material Y1248 will be summarized. The actual NMR experiments will be described in detail in chap. 6 and chap. 7.

5.1 Electronic phase diagram of the cuprates

The cuprates are a class of layered copper-oxide materials with a perovskite structure (for an image depicting the unit cell of Y1248, see fig. 5.3). They consist of quasi 2D copper oxide (CuO_2) planes (one copper ion is connected to 4 neighboring oxygen ions) that are separated by additional, interstitial layers. Superconductivity in these materials was first discovered by Bednorz and Müller [92] in 1986 for which they were awarded the Nobel prize the following year.

The label high temperature superconductor gives credit to the fact that in cuprates, superconductivity potentially occurs at comparably high temperatures; for example the current record superconducting transition temperature of $T_c = 164$ K was observed in the cuprate $HgBa_2Ca_2Cu_3O_{8+x}$ (at ~ 300 kbar) [93] which is about 4 times higher than the highest T_c in a conventional superconductor. While there has been significant progress in understanding the cuprates, the mechanism behind superconductivity is still unclear[a].

The crucial physical properties of the cuprates are determined by the CuO_2 planes and can be varied via the charge carrier concentration δ of these planes. Thus, although there are many different cuprates with distinct chemical compositions, they all show a similar behavior depending on δ. Since δ is typically varied by chemical substitution of atoms (with a different valence) in the interstitial layers, it is often called "doping". Based on wether there is an excess of holes or electrons in the CuO_2 plane, one distinguishes between hole doped and electron

[a] Note that recently a second class of iron based high temperature superconductors, called pnictides, was discovered [94]. They are of minor interest for the present work however.

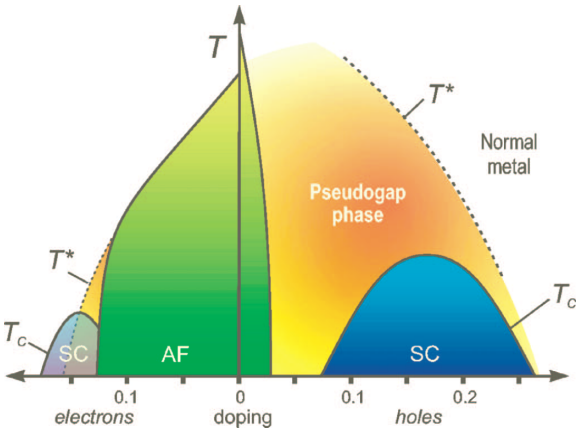

Figure 5.1: Schematic doping dependent electronic phase diagram of the cuprates (figure taken from [95]). Depending on the charge carrier type in the CuO_2 planes one distinguishes between hole doped and electron doped cuprates. At least 4 different phases are encountered: an antiferromagnetic (AF) phase, a superconducting (SC), the pseudogap phase and a "normal" metallic phase. T_c denotes the superconducting transition temperature while T^* indicates the presumed pseudogap transition temperature.

doped cuprates. What makes the cuprates so interesting is the fact that, depending on the charge carrier concentration in the CuO_2 plane, they do not only display superconductivity, but instead multiple peculiar phases are encountered.

In fig. 5.1 a schematic doping dependent electronic phase diagram of the cuprates is shown: the electron doped cuprates are on the left hand side whereas the hole doped cuprates are on the right hand side. For the remainder of this chapter, the focus will be on the hole doped cuprates since the investigated sample Y1248 belongs to this family. At low doping ($\delta \approx 0$), cuprates are antiferromagnetic Mott insulators with the (magnetic) copper in the CuO_2 plane in a $3d^9$ configuration with a hole in the $3d_{x^2-y^2}$. This $3d_{x^2-y^2}$ orbital is hybridized with the $2p_\sigma$ orbitals of the four surrounding $2p^6$ oxygens that have a nearly closed shell. Upon increase of doping, the $2p_\sigma$ orbitals become less filled (increased hole content) and superconductivity occurs below the so-called superconducting dome with the highest T_c at "optimal" doping δ_{opt} (one distinguishes between underdoped and overdoped cuprates depending on wether $\delta < \delta_{opt}$ or $\delta > \delta_{opt}$). Above the superconducting dome, mostly in the underdoped region the pseudogap phase manifests whereas in the overdoped region a "normal" metallic phase is encountered. However, the transition from the pseudogap to the "normal" metallic phase should be understood as a crossover as one cannot, free of doubt, assign a temperature T^* to this phase transition[b].

In the pseudogap phase, cuprates display an electronic behavior that in many ways is characteristic for a metal with an electronic gap (an overview of experimental evidence for this gap can be found in [96] for example). Yet, the origin of this energy gap remains unclear. Furthermore, it is not known how the pseudogap phase is related to the superconducting phase, i.e. wether

[b]The temperature T^* is sometimes assigned to a characteristic change of the spin lattice relaxation rate $1/T_1$ of planar copper. However, the temperature dependence of the magnetic shift $K(T)$ shows the pseudogap behavior already at considerably higher temperatures.

it is a precursor to superconductivity or competes with it. Answering these questions will be essential in solving the mystery of high temperature superconductivity.

The doping dependence of the different electronic phases has been extensively studied previously (for an NMR review, see for example [97, 98]), contributing much to the current understanding of these materials. However, the 2D representation of the phase diagram in fig. 5.1 is not complete as the phases are also affected by parameters like pressure or magnetic field. Thus, additional insight into the cuprates may be gained by varying them.

The effect of high pressure on the superconducting transition temperature T_c has been extensively studied, indicating that T_c of a cuprate can be significantly increased (for a review see [11]). In this regard, it is worth pointing out that to this date, the highest T_c value of 164 K was observed in $HgBa_2Ca_2Cu_3O_{8+x}$ at high pressure conditions of $\sim$300 kbar [93]. This is about 30 K higher than the T_c record at ambient pressure (reported in the same material) and already demonstrates why pressure is an interesting parameter. However, due to a lack of suitable experimental probes of the electronic properties under such conditions, little is known about the effect of pressure on the pseudogap phase (no substantial changes were observed at lower pressure [13, 14]). This was our motivation to carry out temperature dependent shift measurements at high pressure on the pseudogap cuprate Y1248.

5.2 Probing the electronic properties of cuprates via NMR

In this section, it will be reviewed how the electronic properties of cuprates, in particular the electronic spin susceptibility χ_s in the CuO_2 plane, can be probed locally via NMR through shift measurements. Furthermore, it will also be illustrated how the spin part of the magnetic shift K differs if the nucleus is coupled to a single or a two component electronic spin system.

It was already pointed out in sec. 2.1.1 that the resonance frequency ν_0 of a nucleus is influenced by its electronic environment. All experiments that will be presented here were carried out either on ^{17}O or ^{63}Cu and hence quadrupole nuclei ($I > 1/2$). Thus, quadrupole effects have to be considered. Up to second order perturbation theory, ν_0 for the transition $(m-1) \leftrightarrow m$ is then given by

$$\nu_0^m = (1 + {}^nK)\,\nu_L + \delta\nu_m^{(1)} + \delta\nu_m^{(2)}, \tag{5.1}$$

where ${}^nK$ is the magnetic shift, ν_L the Larmor frequency of the investigated nucleus and $\delta\nu_m^{(1)}$ and $\delta\nu_m^{(2)}$ denote the first and second order quadrupole shifts. Note that the superscript 'n' on ${}^nK$ will be used to differentiate between the shifts of ^{17}O ($n=17$) and ^{63}Cu ($n=63$).

The quadrupole shifts $\delta\nu_m^{(1)}$ and $\delta\nu_m^{(2)}$ depend on the electric field gradient present at the nucleus and yield information about the local charge distribution (expressions for $\delta\nu_m^{(1)}$ and $\delta\nu_m^{(2)}$ will be presented as needed). Essentially, they may be used to determine the doping of the CuO_2 plane [99].

The magnetic shift ${}^nK$ on the other hand arises from the hyperfine interaction of a nucleus to

the surrounding electrons and has a T-independent orbital (l) and a T-dependent spin component (s). In the superconducting state, ${}^nK$ is also influenced by the diamagnetic shielding (M). Thus, the temperature dependence of ${}^nK$ is given by

$$ {}^nK(T) = {}^nK_\mathrm{l} + {}^nK_\mathrm{s}(T) + K_\mathrm{M}(T<T_\mathrm{c}). \tag{5.2} $$

It is pointed out that all three terms are orientation dependent. Furthermore, ${}^nK_\mathrm{l}$ and ${}^nK_\mathrm{s}(T)$ vary for individual nuclei due to the different hyperfine couplings and electronic environments.

For the purpose of probing the electronic properties of the CuO_2 plane in the pseudogap phase (see sec. 5.3), one is particularly interested in the spin component ${}^nK_\mathrm{s}$. It arises from the coupling of the nuclear spin $\boldsymbol{I}$ to the electron spin $\boldsymbol{s}$ via the hyperfine interaction

$$ \mathscr{H}_{HF} = \boldsymbol{I}.\overleftrightarrow{A}.\boldsymbol{s}, \tag{5.3} $$

where $\overleftrightarrow{A}$ is the coupling tensor. If the nucleus is coupled only to a single component electronic spin system, this interaction results in a ${}^nK_\mathrm{s}$ given by [98]

$$ {}^nK_s(T) = \frac{A_{zz}}{\gamma_n\gamma_e\hbar^2}\chi_\mathrm{s}(T) = {}^nA_\mathrm{hf}\chi_\mathrm{s}(T), \tag{5.4} $$

with γ_n and γ_e representing the gyromagnetic ratio of the nucleus and the electron while $\chi_\mathrm{s}(T)=\langle s_z(T)\rangle/B_0$ denotes the electronic spin susceptibility (in this notation, the issue of transferred hyperfine couplings [98] is included in the tensor element A_{zz}). The constant ${}^nA_\mathrm{hf}$ is referred to as the hyperfine coupling constant which varies for the different nuclei and orientations.

If, on the other hand, the nucleus is coupled to a two component electronic spin system, ${}^nK_\mathrm{s}(T)$ is given by [100]

$$ {}^nK_\mathrm{s}(T) = \frac{A_{zz}}{\gamma_n\gamma_e\hbar^2}[\chi_\mathrm{s}^\mathrm{A}(T)+\chi_\mathrm{s}^\mathrm{AB}(T)] + \frac{B_{zz}}{\gamma_n\gamma_e\hbar^2}[\chi_\mathrm{s}^\mathrm{B}(T)+\chi_\mathrm{s}^\mathrm{AB}(T)] \tag{5.5} $$

$$ = {}^nA_\mathrm{hf}\chi_\mathrm{s}^\mathrm{A}(T) + ({}^nA_\mathrm{hf} + {}^nB_\mathrm{hf})\chi_\mathrm{s}^\mathrm{AB}(T) + {}^nB_\mathrm{hf}\chi_\mathrm{s}^\mathrm{B}(T), \tag{5.6} $$

where $\chi_\mathrm{s}^\mathrm{A}$ and $\chi_\mathrm{s}^\mathrm{B}$ denote the independent spin susceptibilities of the two components 'A' and 'B' and the term $\chi_\mathrm{s}^\mathrm{AB}=\chi_\mathrm{s}^\mathrm{BA}$ accounts for the coupling of the two components to one another[c].

5.3 Manifestation of the pseudogap in ${}^nK_\mathrm{s}(T)$

NMR measurements of the temperature dependence of the magnetic shift ${}^nK$ [9] and the spin lattice relaxation rate $1/T_1$ [10] were among the first experiments to indicate an unusual electronic

[c]It is pointed out that the hyperfine coupling in eqn. (5.3) also affects the spin lattice relaxation rate $1/T_1$ and hence χ_s may also be probed via $1/T_1$. However, ${}^nK_\mathrm{s}$ measures the static response of the spin susceptibility $\chi_\mathrm{s}(\boldsymbol{q}=0,\omega=0)$ at $\boldsymbol{q}=0$ whereas $1/T_1$ probes a $\boldsymbol{q}$-averaged dynamic response of $\mathrm{Im}\{\chi_\mathrm{s}(\boldsymbol{q},\omega=\omega_0)\}$ (sec. 2.1.2). While such measurements of $1/T_1$ are certainly of interest, they were not carried out in the present thesis since they are considerably more time consuming.

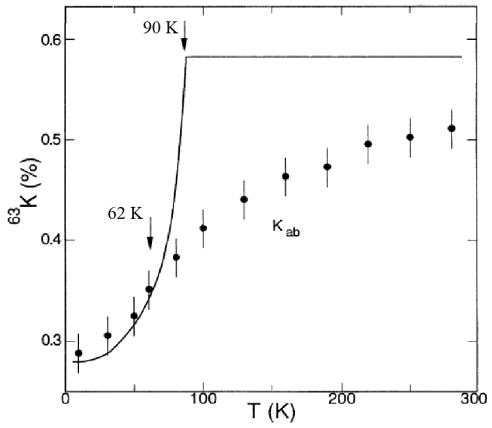

Figure 5.2: Temperature dependence of the ^{63}Cu magnetic shift $^{63}K(T)$ of planar copper in underdoped $YBa_2Cu_3O_{6.63}$ (data points) and optimally doped $YBa_2Cu_3O_{7-\varepsilon}$ (solid line) for $c \perp B_0$. T_c values are indicated by the corresponding arrows. The observed changes with temperature are attributed to the spin shift $^{63}K_{\mathrm{s}}(T)$ only. Reprint of fig. 3 from [102].

behavior in the pseudogap phase. Here, it shall be briefly shown how the pseudogap manifests in the T-dependence of ${}^{n}K_{\mathrm{s}}(T)$. Furthermore, the evidence for single and two component ${}^{n}K_{\mathrm{s}}(T)$ in cuprates will be reviewed.

To illustrate the characteristic T-dependence of the magnetic shift ${}^{n}K$ in the pseudogap phase, fig. 5.2 shows planar copper $^{63}K(T)$ data for $c \perp B_0$ of two different samples of the hallmark cuprate $YBa_2Cu_3O_{6+x}$[d]: an underdoped specimen with $x = 0.63$ ($T_c = 62$ K, displays pseudogap behavior) and an optimally doped specimen with $x \approx 1.0$ ($T_c = 90$ K, no evidence for a pseudogap). Note that for both samples the T-dependence of ^{63}K is dominated by the spin term $^{63}K_{\mathrm{s}}(T)$ since $K_{\mathrm{M}}(T < T_c)$ is comparably small and it is generally assumed that $^{63}K_{\mathrm{s}}$ vanishes approaching $T = 0$ ($^{63}K_{\mathrm{l}} \approx {}^{63}K(T = 0)$).

For the optimally doped sample, $^{63}K_{\mathrm{s}}(T)$ is found to be T-independent above T_c resembling a Fermi liquid and thus metallic behavior. Below T_c a sharp drop in $^{63}K_{\mathrm{s}}(T)$ is observed which can be attributed to the opening of the superconducting gap. A very different T-dependence is encountered for the underdoped sample. Here, $^{63}K_{\mathrm{s}}(T)$ decreases with decreasing T already above T_c and actually continues to decrease smoothly even below (note that there is no sharp drop encountered below T_c). It is pointed out that $^{63}K_{\mathrm{s}}(T)$ in the underdoped sample is expected to become T-independent at higher temperatures.

The fact that $^{63}K_{\mathrm{s}}(T)$ in Y1236:0.63 decreases already above T_c indicates the presence of a spin gap above the superconducting state and is the manifestation of the pseudogap. It is also observed for other nuclei that couple to the spins in the CuO_2 plane, e.g. planar oxygen, or different directions[e]. Furthermore, it occurs in many other cuprates (for a review, see [97]) and hence represents a general behavior of these materials. The extent of the pseudogap feature

[d] In Y1236:x the hole doping is varied via the oxygen content of interlayer CuO chains. It is further noteworthy as the first cuprate with a T_c above the boiling temperature of liquid nitrogen (77 K) [101].

[e] In the particular case of Y1236:x and Y1248, $^{63}K_{\mathrm{s}}(T)$ of planar copper actually vanishes for $c \parallel B_0$ since $A_{zz} \approx 0$. For planar oxygen however, one observes the characteristic T-dependence for any direction.

in the spin shifts ${}^nK_s(T)$, i.e. below what temperature ${}^nK_s(T)$ become T-dependent and how pronounced the T-dependence is, varies with the hole concentration in the CuO_2 plane; in the case of Y1236:x, it initially becomes more pronounced and then weakens again as one goes from $x = 0.63$ (underdoped) to $x = 1.0$ (overdoped) [9]. The latter is typically interpreted as the closing of the pseudogap.

${}^nK_s(T)$: one component or two?

First of all it is pointed out that it is beyond the scope of this thesis to speculate on the validity of different models that would predict the presence of a single component or two component electronic spin system in the CuO_2 plane (for a single component model see for example [103] while a two component model is suggested in [104]). For the work presented here, the phenomenology of the problem is of primary interest.

If a one component scenario is applicable, one expects ${}^nK_s(T)$, measured for different orientations and/or different nuclei, to be proportional to one another since they should only differ in the hyperfine coupling constant ${}^nA_{hf}$. In the case of Y1236:0.63 [102] and Y1248 [105, 106] this was indeed found to be true (although an indication for the failure to explain ${}^{17}O$ shift data of Y1248 by a single component was put forward based on the shift anisotropy [107]).

However, in the case of $La_{1.85}Sr_{0.15}CuO_4$ [108], in agreement with measurements of the uniform spin susceptibility [109, 110], and $HgBa_2CuO_{4+x}$ [111, 112] it was found that a two component scenario applies instead[f]. Interestingly, in the case of $HgBa_2CuO_{4+x}$, ${}^{63}K_s(T)$ of planar copper could be decomposed into a component ${}^{63}A_{hf}\chi_s^1(T)$ which displayed the pseudogap T-dependence and a Fermi liquid like component ${}^{63}B_{hf}\chi_s^2(T)$ similar to that observed in optimally doped Y1236:x, i.e

$$ {}^{63}K_s(T) = {}^{63}A_{hf}\chi_s^1(T) + {}^{63}B_{hf}\chi_s^2(T). \tag{5.7} $$

Yet, wether a two component description of ${}^nK_s(T)$ for other cuprates is mandatory or just a peculiarity of these selected materials is unclear.

5.4 $YBa_2Cu_4O_8$: the test system

Our high pressure NMR experiments were performed on $YBa_2Cu_4O_8$, a high temperature superconductor with $T_c \approx 81$ K [114], for the following two reasons: (a) it displays the pseudogap behavior in ${}^nK_s(T)$ and (b) it is electronically "clean" due to the stoichiometric composition resulting in narrow NMR lines. Both together make it an ideal candidate for the study of the effect of pressure on the pseudogap. In our NMR experiments up to 63 kbar, planar oxygen (chap. 6) and planar copper (chap. 7) were used as the probing nuclei since they couple strongest to the spin system in the CuO_2 plane.

[f] It is further pointed out that Walstedt et al. argued that relaxation data of $La_{1.85}Sr_{0.15}CuO_4$ could not be explained with a single spin component only [113].

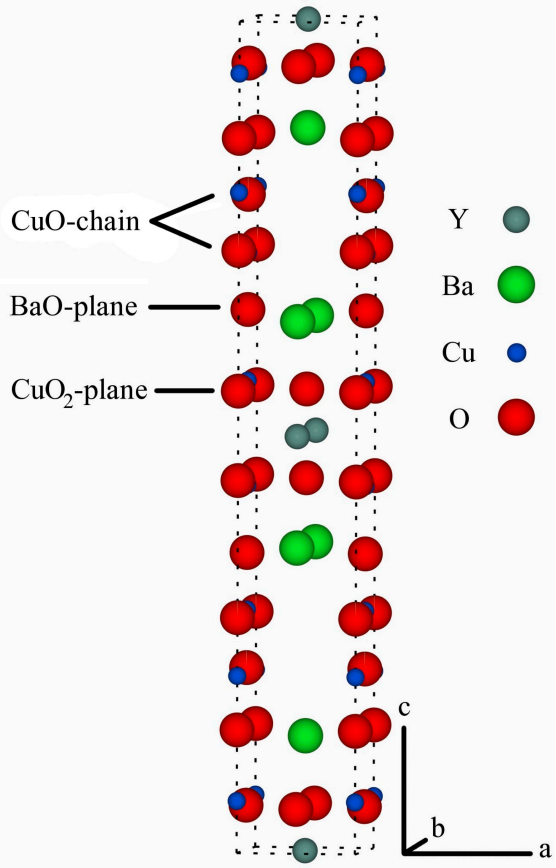

Figure 5.3: Unit cell of $YBa_2Cu_4O_8$. The lattice structure is orthorhombic with lattice constants a=3.871 Å, b=3.840 Å and c=27.25 Å [114].

For the purpose of site assignment in these NMR experiments, the unit cell of Y1248 is shown in fig. 5.3. The lattice structure comprises of CuO_2 planes, separated by a stacking of a BaO plane, a CuO double chain layer and another BaO plane; this structure is additionally mirrored at the plane containing the Y. While this is a very large unit cell containing many nuclei, there are only two electronically distinct copper sites and four electronically distinct oxygen sites. In accordance with [115], they will be labelled as follows:

- Cu(1): copper in CuO chain
- Cu(2): copper in CuO_2 plane
- O(1): oxygen in BaO plane, also referred to as apex oxygen
- O(2): oxygen in CuO_2 plane, in-plane Cu-O-Cu bond axis along a-axis
- O(3): oxygen in CuO_2 plane, in-plane Cu-O-Cu bond axis along b-axis
- O(4): oxygen in CuO chain

6 High pressure ^{17}O NMR on $YBa_2Cu_4O_8$

In this chapter, the ^{17}O NMR shift measurements on a powder of the high temperature superconductor $YBa_2Cu_4O_8$ (Y1248) up to a pressure of 63 kbar will be discussed [116, 117]. These experiments reveal the spin shift $^{17}K_s(T)$ to become increasingly Fermi liquid like at high pressure, indicating the suppression of the pseudogap. Furthermore, it will be illustrated that $^{17}K_s(T)$ displays a scaling behavior under pressure that suggests the presence of a second spin susceptibility in the CuO_2 plane.

6.1 Experimental conditions

In this section, the experimental conditions of the high pressure ^{17}O NMR experiments on the Y1248 powder will be briefly summarized.

The experiments were performed on pieces of a Y1248 powder pellet that was prepared as described in [118]. It was gratefully provided by Dr. Grant V. M. Williams from the MacDiarmid Institute and Industrial Research Limited, Wellington, New Zealand[a]. For this sample, measurement of the dc-magnetization in a field of 2 mT yielded a superconducting transition temperature of $T_c = 81$ K in good agreement with values found in the literature (see for example [119] and references therein). The pellet was ^{17}O ($I = 5/2$) exchanged for 12 hours at 700 °C in 70% enriched O_2 gas[b].

Two MACs were prepared for the experiments at high pressure and loaded with pieces of the ^{17}O-enriched Y1248 powder pellet. One cell (1.0 mm culet diameter, 300 µm diameter microcoil with 10 turns) was initially pressurized to 20 kbar, the other (0.8 mm culet diameter, 200 µm diameter microcoil with 9 turns) to 42 kbar. Their pressure was later increased to 30 kbar and 63 kbar respectively. Glycerin was used as a pressure transmitting medium and pressure was measured via the ruby-fluorescence method. Fig. 6.1 shows the loaded 20 kbar cell before closing. Experiments at ambient pressure were carried out on a larger piece of the powder pellet employing a regular NMR setup. As an alignement was not possible in the high pressure cells, all experiments were performed on unaligned powder. Note that this fact made it unfeasible to carry out copper NMR measurements on the powder sample and that single crystals were used instead for the ^{63}Cu experiments in chap. 7.

[a] Now at the Victoria University of Wellington, New Zealand.

[b] Oxygen has three naturally occurring isotopes, i.e. ^{16}O, ^{17}O and ^{18}O of which only ^{17}O has a spin and therefore is NMR sensitive. As the natural abundance of 0.038% of this isotope is quite low it was necessary to ^{17}O-enrich the sample in order to achieve a feasible SNR.

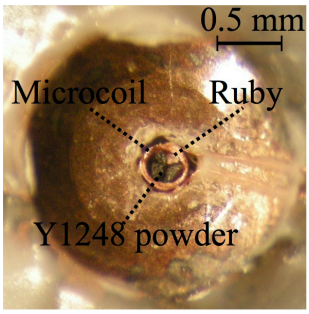

Figure 6.1: Top view along the axis of the microcoil (300 µm diameter), showing the center of the gasket of the opened 20 kbar MAC. The microcoil contains pieces of the Y1248 powder pellet and a small ruby chip for pressure determination.

The ^{17}O NMR measurements were conducted at ambient pressure and under high pressures of 20, 42 and 63 kbar in the temperature range from room temperature (RT $\approx$ 294 K) down to 85 K in a magnetic field of $B_0 = 11.7$ T. Signal was recorded by accumulation of the echo following the Hahn-echo sequence $\pi/2-\tau-\pi$ with a $\pi/2$-pulse duration (π) of 1.7 µs (3.4 µs) and a pulse separation of $\tau = 30$ μs. At a specific pressure, the $\pi/2$- and π-pulse conditions were determined at room temperature by variation of the pulse power P. The resonance circuit in a MAC typically had a quality factor of $Q \approx 12$ at this temperature and the maximum signal was found for about $P_{\rm opt} \approx 1$ W. While cooling, the change in $P_{\rm opt}$ due to the temperature dependence of the coil-resistance r was then inferred from the observed temperature dependence of Q (for example, $Q \approx 20$ at 106 K) via eqn. (2.26) and (2.29). A typical number of scans at 20 kbar and $T = 140$ K is 4×10^5 with a last delay of 130 ms. Spectra were acquired by Fourier-transformation of half of the echo signal. For the purpose of smoothing, the time-domain data was multiplied by an exponential decay $\exp\{-lb\times t\}$ with a linebroadening factor of $lb = 5$ kHz. As a reference for the ^{17}O-shifts, the resonance frequency $\nu_{\rm ref}$ of ^{17}O in tap water was used.

The superconducting transition temperature $T_{\rm c}$ of the Y1248 at high pressure in the MACs was determined in zero field with the technique described in sec. 3.3.

6.2 Results and discussion

In the next section, the experimental results of the high pressure experiments on the ^{17}O exchanged powder shall be presented and discussed in detail. Most notably, it will be demonstrated that the pseudogap feature in $^{17}K_{\rm s}(T)$ of planar oxygen decreases under pressure, indicating the closing of the pseudogap. Furthermore, it will be illustrate why the observed changes of $^{17}K_{\rm s}(T)$ imply a two component picture for Y1248.

6.2.1 Pressure dependence of $T_{\rm c}$

In fig. 6.2, the observed pressure dependence of $T_{\rm c}(p)$ is shown. $T_{\rm c}$ is found to increase rapidly from 81 K at 1 bar to 102 K at 42 kbar with an initial pressure derivative of $dT_{\rm c}/dp \approx 0.56$ K/kbar.

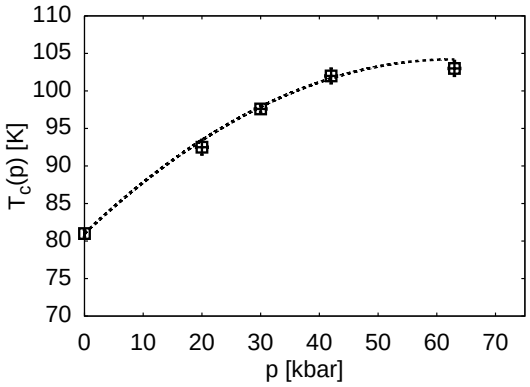

Figure 6.2: Pressure dependence of T_c of the Y1248 powder. Application of pressure increases T_c significantly from 81 K at ambient pressure up to 103 K at 63 kbar. The dashed line is a guide to the eye.

A further increase of pressure up to 63 kbar then raises T_c only slightly to 103 K. All values are in good agreement with those found in the literature [119, 120]. This indicates that pressure in the MACs did not change considerably while cooling down.

It should be noted that application of high pressures up to 120 kbar is capable of increasing T_c up to 108 K [119]. In contrast to that, T_c is raised only up to a maximum of 91 K if the hole content in the CuO_2-plane is varied via Ca-doping in $Y_{1-x}Ca_xBa_2C_4O_8$ for example [121]. This shows that pressure is more effective in increasing T_c in Y1248. The question wether the hole-doping of the CuO_2-plane is influenced by pressure will be addressed in sec. 7.3.2.

6.2.2 Sample spectra

Typical ^{17}O NMR powder spectra recorded at ambient pressure and high pressures of 20, 42 and 63 kbar in a magnetic field of $B_0 = 11.7$ T at a temperature of about 110 K are shown in fig. 6.3. At ambient pressure, three distinct peaks are apparent; they can be assigned to the central transitions of the apex oxygen O(1), plane oxygens O(2,3) and chain oxygen O(4) according to the discussion below. Upon application of pressure, the resonance frequency of the O(2,3) peak strongly increases while that of the O(1) site is nearly unaffected. Unfortunately, the O(4) peak could not be resolved at 42 and 63 kbar due to an insufficient SNR.

To understand the shape of the powder spectra and the observed changes with pressure (and temperature), it is necessary to take quadrupole and hyperfine effects into consideration. In principle, one expects to be able to observe $2I = 5$ lines for each oxygen site because of the quadrupole interaction of the ^{17}O nuclei with the local electric field gradient. For each oxygen site, the resonance frequencies ν_0^m of the satellite transitions $(m-1) \leftrightarrow m$ $(m \neq 1/2)$ up to first order perturbation theory are given by

$$\nu_0^m = \left[1 + {}^{17}K\right] \nu_L + \delta\nu_m^{(1)}, \tag{6.1}$$

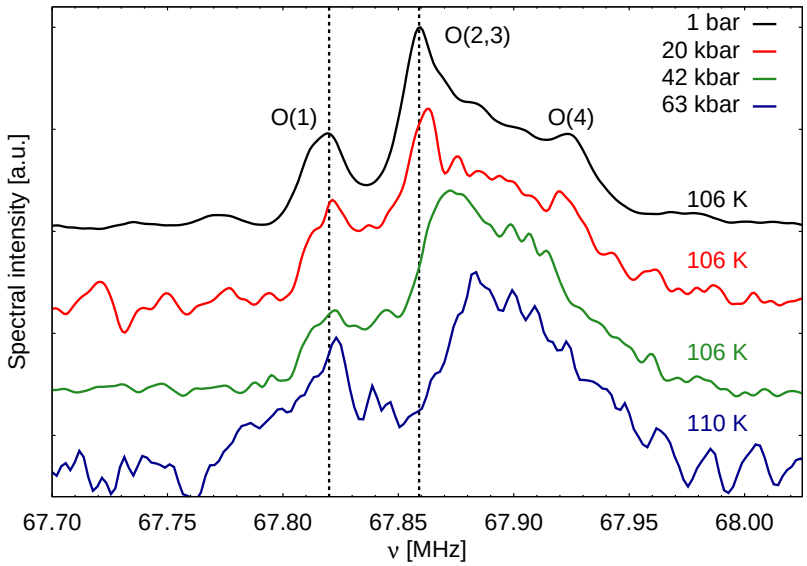

Figure 6.3: Selected ^{17}O NMR powder spectra recorded at ambient pressure (1 bar) and high pressures (20, 42 and 63 kbar), in a magnetic field of $B_0 = 11.7$ T at the temperatures given in the figure. The spectra are shown in order of increasing pressure from top to bottom. The peaks observed at ambient pressure can be assigned to the apex oxygen O(1), plane oxygen O(2,3), and chain oxygen site O(4). No significant changes in resonance frequency are observed for O(1) while the resonance frequency of O(2,3) increases significantly with increasing pressure. Unfortunately, the O(4) peak could not be resolved at 42 and 63 kbar. Dashed lines are a guide to the eye.

where ^{17}K denotes the magnetic shift, $\delta\nu_m^{(1)}$ is the first order quadrupole shift and ν_L is the Larmor frequency that is determined via the resonance frequency $\nu_L \approx \nu_{\mathrm{ref}} = 67.80$ MHz of ^{17}O in tap water. The resonance frequency ν_0 of the central transition -1/2$\leftrightarrow$1/2 is affected by the quadrupole interaction only in second order. Thus,

$$\nu_0 \quad = \quad [1 + {}^{17}K]\nu_L + \delta\nu_{\frac{1}{2}}^{(2)}, \tag{6.2}$$

with $\delta\nu_{1/2}^{(2)}$ denoting the second order quadrupole shift. Since ^{17}K, $\delta\nu_m^{(1)}$ and $\delta\nu_{1/2}^{(2)}$ depend on the orientation of the oxygen site with respect to B_0, so do ν_0 and ν_0^m. This fact profoundly influences the shape of the spectra as an average over all orientations is observed.

Quadrupole shifts $\delta\nu_m^{(1)}$ and $\delta\nu_{1/2}^{(2)}$

The relevance of the quadrupole shifts $\delta\nu_m^{(1)}$ and $\delta\nu_{1/2}^{(2)}$ shall be analyzed first. Ambient pressure values of the quadrupole frequency ν_Q and asymmetry parameter η for the different oxygen sites have been determined earlier by Mangelschots et al. [105]; they are reprinted for convenience in tab. 6.1. Note that the electric field gradient has smaller than axial symmetry, i.e. $\eta \neq 0$, at all 4 oxygen sites.

	O(1)	O(2)	O(3)	O(4)
ν_Q [MHz]	0.98	0.93	0.93	0.91
η	0.25	0.21	0.23	0.87
$^{17}K_{\mathrm{a}}$	-0.006	0.155	0.076	0.098
$^{17}K_{\mathrm{b}}$	0.017	0.076	0.155	0.168
$^{17}K_{\mathrm{c}}$	0.087	0.066	0.066	0.170

Table 6.1: Quadrupole frequency ν_Q, asymmetry parameter η of the quadrupole tensor and magnetic shift tensor ^{17}K-components along the crystal axis a, b, c for the four oxygen sites at ambient pressure and 100 K. The principle axis of the quadrupole tensor is along the c-axis, a-axis, b-axis and b-axis for O(1), O(2), O(3) and O(4) respectively. Data is taken from [105].

The first order quadrupole shift $\delta\nu_m^{(1)}$ for $\eta \neq 0$ is given by [15]

$$\delta\nu_m^{(1)} = -\nu_Q \frac{2m-1}{4} \left[3\cos^2\theta - 1 + \eta \sin^2\theta \cos 2\phi\right], \tag{6.3}$$

where θ and ϕ denote the Euler angles that describe the orientation of the electric field gradient with respect to B_0. In an unaligned powder, an average over all possible angles θ and ϕ is observed. Using the values of ν_Q and η in tab. 6.1 then shows that the $m = $-1/2 and $m = 3/2$ transitions are spread out over $\Delta\nu \sim 1.5$ MHz whereas the $m = $-3/2 and $m = 5/2$ transitions spread out over $\Delta\nu \sim 3.0$ MHz. This is large compared to the spectral window in fig. 6.3 and, as their intensities are too low, the satellite transitions effectively do not contribute to the spectra[c].

Consequently, only the central transitions of the oxygen sites are observed since they are only weakly influenced by $\delta\nu_{1/2}^{(2)}$. The amplitude of $\delta\nu_{1/2}^{(2)}$ shall be estimated from the case of axial symmetry ($\eta = 0$)

$$\delta\nu_{\frac{1}{2}}^{(2)} = -\frac{\nu_Q^2}{16\nu_L} \left[I(I+1) - \frac{3}{4}\right] \sin^2\theta \left(9\cos^2\theta - 1\right), \tag{6.4}$$

where θ indicates the angle between the principle axis of the electric field gradient and B_0. Again, in the unaligned powder an average over all angles θ is observed. For the different oxygen sites, this yields a $\delta\nu_{1/2}^{(2)}$ ranging from -11 kHz ($\theta = 42°$) to +6 kHz ($\theta = 90°$). This is both, small compared to the frequency shift with respect to $\nu_L \approx \nu_{\mathrm{ref}} = 67.80$ MHz and small compared to the width of the spectra shown in fig. 6.3. Furthermore, in absence of a structural phase transition under pressure [122], one expects only small changes of ν_Q due to the reduction of the lattice constants or a variation of the charge distribution [99]. Therefore, $\delta\nu_{1/2}^{(2)}$ will remain almost unchanged at higher pressure and certainly cannot explain the shift to higher frequency of the O(2,3) peak.

[c]The intensities, i.e. area under their curve in a spectrum, of the different transitions $m = $ -3/2, -1/2, 1/2, 3/2 and 5/2 have the ratio 5:8:9:8:5.

Magnetic shift ^{17}K and simulated powder spectrum

Thus, it can be concluded that the magnetic shift ^{17}K in eqn. (6.2) must be the term that dominates the shape of the powder spectra and the shift of the various peaks compared to ν_L. Since the following analysis will restrict itself to temperatures above T_c and only slightly below, the diamagnetic contribution $K_M(T<T_c)$ can be neglected. ^{17}K then contains only the T-independent orbital term (l) and the T-dependent spin term (s) that arises from the coupling of the ^{17}O nuclei to the electronic spin susceptibility $\chi_s(T)$

$$^{17}K(T) = {}^{17}K_l + {}^{17}K_s(T). \tag{6.5}$$

To undoubtedly assign the peaks in fig. 6.3 to the different oxygen sites, a simulated powder spectrum based on earlier data shall be compared to the ambient pressure spectrum. For that purpose, the small second order quadrupole shift $\delta\nu^{(2)}_{1/2}$ will be neglected, in which case eqn. (6.2) simplifies to $\nu_0 = \left[1+{}^{17}K\right]\nu_L$. Mangelschots et al. [105] determined the ^{17}K-tensor components, i.e. the value of ^{17}K along the different crystal axis, at ambient pressure for all four oxygen sites. Their values at 100 K are included in tab. 6.1. Note that ^{17}K has smaller than axial symmetry for all oxygen sites and that the ^{17}K-components of the two planar oxygen sites O(2) and O(3) differ only in their direction-dependency.

Knowledge of the ^{17}K-tensors allows one to simulate the shape of the spectrum in the unaligned powder. For that purpose it is first necessary to determine the spectral intensity function $\mathscr{I}(\nu)$, i.e. the density of spins in the frequency range ν to $\nu+\delta\nu$, for each oxygen site. Denoting the resonance frequencies along the three crystal axis by $\nu_\alpha = \left[1+{}^{17}K_\alpha\right]\nu_L$ ($\alpha = 1,\ 2,\ 3$) with $\nu_1<\nu_2<\nu_3$, $\mathscr{I}(\nu)$ is given by [84]

$$\mathscr{I}(\nu) \propto \sqrt{\frac{(\nu_3-\nu_1)(\nu_3-\nu_2)}{(\nu_3-\nu)(\nu_2-\nu_1)}} \int_0^{\frac{\pi}{2}} \left[1 - \frac{(\nu-\nu_1)(\nu_3-\nu_2)}{(\nu_3-\nu)(\nu_2-\nu_1)}\sin^2\gamma\right]^{-\frac{1}{2}} d\gamma \tag{6.6}$$

for the frequency range $\nu_1<\nu<\nu_2$,

$$\mathscr{I}(\nu) \propto \sqrt{\frac{\nu_2-\nu_1}{\nu-\nu_1}} \int_0^{\frac{\pi}{2}} \left[1 - \frac{(\nu_2-\nu_1)(\nu_3-\nu)}{(\nu_3-\nu_2)(\nu-\nu_1)}\sin^2\gamma\right]^{-\frac{1}{2}} d\gamma \tag{6.7}$$

for $\nu_2<\nu<\nu_3$ and zero elsewhere. Furthermore, one has to take into account that line broadening occurs because of spin-spin interactions and more importantly that the data was smoothed by multiplicating the FIDs with an exponential decay $\exp\{\text{-}lb\times t\}$. Therefore, $\mathscr{I}(\nu)$ additionally has to be folded with a lorentzian function $f(\nu)$

$$f(\nu) = \frac{1}{\pi}\frac{\frac{\sigma}{2}}{(\nu-\nu_0)^2+\frac{\sigma^2}{4}}, \tag{6.8}$$

where the linebroadening factor σ of $\sigma = lb = 5$ kHz is used.

A python program that is included in app. 9.4 was used to simulate the powder spectrum

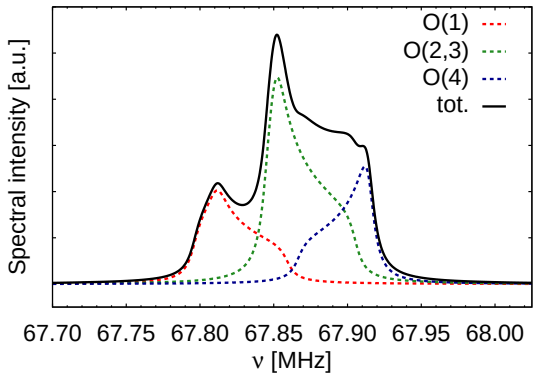

Figure 6.4: Simulated ambient pressure powder spectra at $T = 100$ K of the central transition -1/2↔1/2 of the different oxygen sites O(1), O(2)+O(3) summarized as O(2,3) and O(4) (dashed lines) and the resulting combined spectrum (solid line). Note that it is not possible to distinguish between the two different planar oxygen sites O(2) and O(3) in the powder spectrum as their sets of $^{17}K_\alpha$ differ only in the direction-dependency and that they are therefore combined into one spectrum labeled O(2,3). The small second order quadrupole shifts $\delta\nu^{(2)}_{1/2}$ are neglected.

of a particular oxygen site for a given set of $^{17}K_\alpha$ according to the previous discussion. The resulting combined powder spectrum (and individual contributions of the different oxygen sites) at 100 K using the data from [105] is shown in fig. 6.4: it agrees very well with the shape of the ambient pressure spectrum in fig. 6.3 that was recorded at a slightly higher temperature of 106 K. Note that the intensities of the individual O(1), O(2,3) and O(4) spectra have been normalized according to their stoichiometry to 1:2:1. Furthermore, it is pointed out that one cannot distinguish between the two planar oxygen sites O(2) and O(3) in the powder spectrum as their components of ^{17}K only differ in the orientation-dependency. Based on the simulated powder spectrum, it is also clear that the peaks in fig. 6.3 may be attributed to the different oxygen sites.

6.2.3 Effect of pressure on $^{17}K(T)$

The temperature dependence of the magnetic shift $^{17}K(T)$ for the O(1) and especially the O(2,3) peak at the various pressures shall be discussed next[d]. Most notably, it will be shown that the characteristic pseudogap feature in $^{17}K_s(T)$ for O(2,3) is suppressed upon application of pressure indicating a closing of the pseudogap.

For a particular spectrum recorded at the pressure p and temperature T, the resonance frequency $\nu_0(p,T)$ of the O(2,3) peak was determined by fitting a Lorentzian function (eqn. (6.8)) to it in the vicinity of the peak. For O(1), $\nu_0(p,T)$ was simply graphically estimated from the corresponding local spectral maximum. For both peaks, the second order quadrupole shift $\delta\nu^{(2)}_{1/2}$

[d] As it was not possible to resolve the O(4) peak at higher pressure it is excluded in the following discussion. It should be noted however that ^{17}K for the chain oxygen is dominated by the hyperfine coupling to the metal like spin susceptibility in the CuO-chains and that it hence is T-independent above T_c at ambient pressure [105,106]. It thus yields no direct information about the pseudogap.

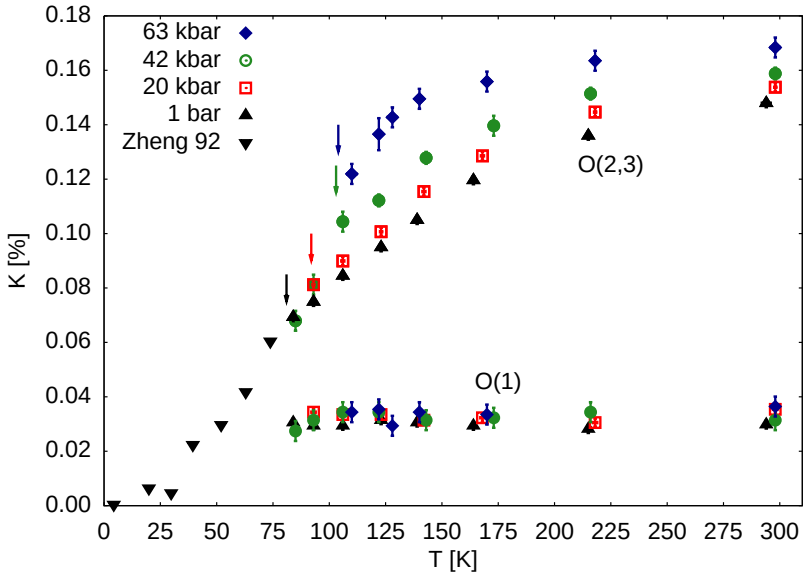

Figure 6.5: Temperature and pressure dependence of the ^{17}O NMR shift $^{17}K(p,T)$ for apical oxygen O(1) and plane oxygen O(2,3) at ambient pressure and high pressures of 20, 42 and 63 kbar. Due to a limited SNR, shifts were measured mostly at temperatures above T_c. The ambient pressure data for O(2,3) below 75 K (Zheng 92 ▼) is taken from [123]. Arrows indicate the measured T_c. In the (p,T)-range investigated, $^{17}K(p,T)$ remains nearly constant for O(1) while varying strongly with pressure and temperature for O(2,3). With increasing pressure, $^{17}K(p,T)$ of O(2,3) increases for all temperatures $T > T_c$ such that the pseudogap feature begins to vanish.

can be estimated to be about +6 kHz as they arise from orientations for which B_0 is perpendicular to the principal axis of the local electric field gradient ($\theta \approx 90°$). According to eqn. (6.2), the p- and T-dependent magnetic shift $^{17}K(p,T)$ is then given by

$$^{17}K(p,T) = \frac{\nu_0(p,T) - \delta\nu_{1/2}^{(2)} - \nu_L}{\nu_L}, \tag{6.9}$$

where ν_L is approximately given by ν_{ref}.

In fig. 6.5, the resulting temperature dependencies of ^{17}K for O(1) and O(2,3) are shown at ambient pressure (1 bar) and high pressures of 20, 42 and 63 kbar; T_c values from fig. 6.2 are indicated by arrows. Due to limitations in the SNR in the superconducting state, measurements were carried out mostly in the normal state above T_c. For the purpose of illustration, ambient pressure data of $^{17}K(T)$ for O(2,3) ($c \| B_0$) at temperatures below 75 K (Zheng 92 ▼) from [123] is also included. The ambient pressure data for both sites O(1) and O(2,3) are in good agreement with the literature [105, 106, 123] and ^{17}K(1 bar) for O(2,3) seamlessly connects to the low-T data from [123].

For O(1), ^{17}K is found to vary only little with pressure and temperature which indicates that these nuclei couple only weakly to the spin susceptibility in the CuO_2-plane. However,

for the O(2,3) signal, ^{17}K is found to vary significantly with both parameters. At ambient pressure, $^{17}K(T)$ of O(2,3) decreases with decreasing temperature already in the normal state above T_c which is the manifestation of the pseudogap. As the data from [123] shows, this trend smoothly continues through T_c and ^{17}K eventually almost vanishes approaching $T=0$ K (small $^{17}K_l$ remains). With increasing pressure, $^{17}K(T)$ for O(2,3) in the normal state is found to (a) increase for all temperatures and (b) decrease less with decreasing temperature (c.f. for example ΔK of -0.053% from RT down to 123 K at 1 bar and a ΔK of -0.032% from RT down to 122 K at 63 kbar). In addition, it is pointed out that some of the low temperature data points at high pressure (42 and 63 kbar) show the influence of T_c as the drop precipitously.

Since the orbital shift $^{17}K_l$ for O(2,3) is small (about 0.007% at ambient pressure [123]) and one does not expect it to vary considerably with pressure, these changes must be related to the spin shift $^{17}K_s(p,T)$. The data in fig. 6.5 then show that at higher pressure, $^{17}K_s(T)$ becomes increasingly T-independent and hence Fermi liquid like above T_c; a behavior that signals the closing of the pseudogap.

It is pointed out that ambient pressure ^{63}Cu measurements on planar copper Cu(2) show $^{63}K_s(T)$ to become T-independent above 300 K [124]. Since $^{63}K_s(T)$ of Cu(2) originates from the hyperfine coupling to the same spin susceptibility, it is reasonable to assume that $^{17}K_s(p,T)$ of O(2,3) is T-dependent only in the temperature range shown[e].

6.2.4 Scaling behavior of $^{17}K_s(p,T)$ of planar oxygen

In this section, it will be demonstrated that at temperatures above T_c the T-dependence of $^{17}K_s(p,T)$ scales with pressure. Additionally, the question will be addressed wether the observed changes in $^{17}K_s(p,T)$ can be understood in terms of a single or two component spin susceptibility in the CuO_2 plane.

For the following discussion, the small orbital contribution to $^{17}K(p,T)$ for O(2,3) will be neglected, i.e. $^{17}K(p,T) \approx {}^{17}K_s(p,T)$. Inspired by earlier findings on the cuprate $HgBa_2CuO_{4+x}$ [111, 112], a plot of $^{17}K(p,T)$ at high pressures $p>1$ bar vs. $^{17}K(1\text{ bar},T)$ is shown in the main panel of fig. 6.6. Note that in this rather unusual plot, the temperature T is an implicit parameter (since not all experiments were carried out at the same temperature, T was parametrized via a 4^{th} order polynomial fit to $^{17}K(1\text{ bar},T)$ which is shown in the inset of fig. 6.6). Interestingly, it is found that at temperatures above T_c, $^{17}K(p,T)$ is well described by a linear relation

$$^{17}K(p,T) = \kappa_p \times {}^{17}K(1\text{ bar},T) + C_p, \tag{6.10}$$

where the constants κ_p and C_p depend only on the applied pressure and decrease and increase with pressure respectively (their values determined via a least square fit to the data may be found in tab. 6.2). A deviation from this linear relation is only observed at the high pressures

[e]The argument is weaker for the high pressure data. However, given the decreased T-dependence of $^{17}K_s(p,T)$ at higher pressure, it is unlikely that $^{17}K_s(p,T)$ changes significantly above room temperature even at those pressures.

p [kbar]	20	42	63
κ_p	1.02	0.87	0.56
C_p [%]	0.004	0.033	0.089

Table 6.2: Pressure dependent values of κ_p and C_p.

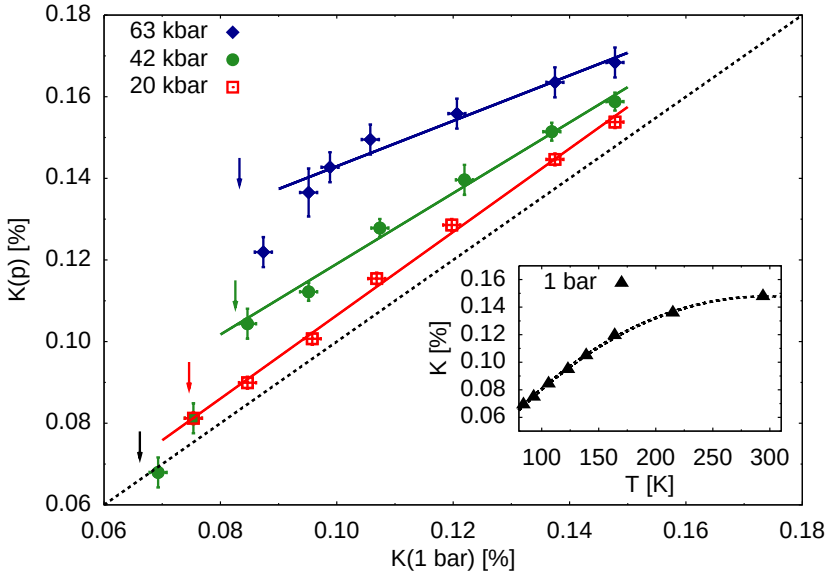

Figure 6.6: (Main panel) $^{17}K(p,T)$ vs. $^{17}K(1\text{ bar},T)$ of O(2,3) using temperature as an implicit parameter. In the normal state, $^{17}K(p,T)$ is found to be linear in $^{17}K(1\text{ bar},T)$ at all investigated pressures. A deviation from this behavior is only observed at 42 and 63 kbar close to T_c and below. The solid lines indicate the least square fits (according to eqn. (6.10)) that were used to extract the constants κ_p and C_p whereas the dashed diagonal line represents $^{17}K(1\text{ bar},T)$. Arrows indicate the measured T_c values. (Inset) The shown 4$^{\text{th}}$ order polynomial fit (dashed line) was used to parametrize T via $^{17}K(1\text{ bar},T)$.

of 42 and 63 kbar in the vicinity of T_c and below. There, $^{17}K(p,T)$ drops considerably and approaches the dashed line that represents $^{17}K(1\text{ bar},T)$.

$^{17}K_s(p,T)$: single or two component?

It is quite remarkable that even though $^{17}K(p,T) \approx {}^{17}K_s(p,T)$ varies strongly with temperature, the ratio

$$\kappa_p = \frac{\Delta^{17}K(p)}{\Delta^{17}K(1\text{ bar})} = \frac{{}^{17}K(p,T_1) - {}^{17}K(p,T_2)}{{}^{17}K(1\text{ bar},T_1) - {}^{17}K(1\text{ bar},T_2)} \tag{6.11}$$

is found to be independent of the temperatures $T_1, T_2 > T_c$. Assuming the hyperfine coupling to be unaffected by pressure, eqn. (6.11) then indicates that $^{17}K_s(p,T)$ contains a term $^{17}A_{hf}\chi_s^1(p,T)$ which arises from the coupling to a T-dependent spin susceptibility $\chi_s^1(p,T)$ which scales with

pressure according to

$$\chi_{\rm s}^1(p,T) = \kappa_p \chi_{\rm s}^1(1\ {\rm bar},T). \tag{6.12}$$

However, this T-dependent term $^{17}A_{\rm hf}\chi_{\rm s}^1(p,T)$ cannot account for the T-independent constant C_p nor can an increase of $\delta\nu_{1/2}^{(2)}$ or $^{17}K_{\rm l}$ as C_p becomes quite large at high pressure. Instead, it shows that $^{17}K_{\rm s}(p,T)$ additionally contains a second term $^{17}B_{\rm hf}\chi_s^2(p)$ which arises from the coupling to a second spin susceptibility $\chi_{\rm s}^2(p)$. This second term appears to be T-independent above $T_{\rm c}$ and increases with pressure. Thus, one is led to a two component spin shift $^{17}K_{\rm s}(p,T)$ $(T>T_{\rm c})$ given by[f]

$$^{17}K_{\rm s}(p,T) = {}^{17}A_{\rm hf}\chi_s^1(p,T) + {}^{17}B_{\rm hf}\chi_s^2(p). \tag{6.13}$$

In eqn. (6.13), only $^{17}A_{\rm hf}\chi_s^1(p,T)$ displays the characteristic T-dependence of the pseudogap and is progressively suppressed with pressure while $^{17}B_{\rm hf}\chi_s^2(p)$ must be small at ambient pressure and becomes increasingly significant at higher pressure. It is pointed out that (a) $\chi_{\rm s}^2(p)$ must originate from the CuO_2 plane and cannot be the spin susceptibility of the CuO chains since the shift of O(1) reveals no significant changes under pressure and (b) similar observations were made in the two component systems $La_{1.85}Sr_{0.15}CuO_4$ [108] and $HgBa_2CuO_{4+x}$ [111, 112].

$^{17}K_{\rm s}(p,T)$ and hence $^{17}K(p,T)$ eventually have to vanish or at least become very small below $T_{\rm c}$ because of the opening of the superconducting gap. Although it was not possible to follow this behavior properly via the shift measurements presented here (the SNR in the superconducting state was insufficient), the onset of a drop of $^{17}K(p,T)$ in the vicinity of $T_{\rm c}$ is clearly observed in fig. 6.6 at the high pressures of 42 and 63 kbar. Given the scaling of the pseudogap component $^{17}A_{\rm hf}\chi_{\rm s}^1(p,T)$ with pressure and its smooth T-dependence, c.f. the 1 bar data in fig. 6.5, it is likely that the drop of $^{17}K(p,T)$ near $T_{\rm c}$ represents a rapid decrease of the second component $^{17}B_{\rm hf}\chi_{\rm s}^2(p)$ only. This component then has the T-dependence of the Fermi liquid like spin susceptibility observed in optimally doped $YBa_2Cu_3O_{6+x}$ shown in fig. 5.2 [125, 126]. That at 63 kbar, the drop appears to occur already slightly above $T_{\rm c}$ could be due to an inhomogeneity of the pressure across the sample or be caused by superconducting fluctuations [127].

Pressure evolution of the two components

The values of the pseudogap component $^{17}A_{\rm hf}\chi_{\rm s}^1(p,T\approx 300\ {\rm K})$ and the Fermi liquid like component $^{17}B_{\rm hf}\chi_{\rm s}^2(p)$ at the various pressures shall be estimated next. Note that $^{17}A_{\rm hf}\chi_{\rm s}^1(p,T\approx 300\ {\rm K})$ approximately represents the "ungapped" value of the pseudogap component since it is not expected to change significantly at higher temperatures.

Using eqn. (6.10), (6.12) and (6.13), one can derive the following expressions for $^{17}A_{\rm hf}\chi_{\rm s}^1(p,T\approx$

[f] In the notation of eqn. (5.6), $^{17}A_{\rm hf}\chi_{\rm s}^1(p,T) = {}^{17}A'_{\rm hf}\chi_{\rm s}^{\rm A}$ and $^{17}B_{\rm hf}\chi_{\rm s}^2(p) = ({}^{17}A'_{\rm hf} + {}^{17}B'_{\rm hf})\chi_{\rm s}^{\rm AB} + {}^{17}B'_{\rm hf}\chi_{\rm s}^{\rm B}$ with $^{17}A'_{\rm hf}$ and $^{17}B'_{\rm hf}$ denoting the two different hyperfine couplings in eqn. (5.6). If either $^{17}B'_{\rm hf}$, $\chi_{\rm s}^{\rm AB}$ or $\chi_{\rm s}^{\rm B}$ is small, it is not possible to distinguish between eqn. (6.12) and eqn. (5.6) experimentally.

p [kbar]	0.001	20	42	63
$^{17}A_{\rm hf}\chi_{\rm s}^1(p,{\rm RT})$ [%]	0.14	0.14	0.12	0.08
$^{17}B_{\rm hf}\chi_{\rm s}^2(p)$ [%]	0.01	0.01	0.04	0.09

Table 6.3: Pressure dependent values of $^{17}A_{\rm hf}\chi_{\rm s}^1(p,T)$ at room temperature and $^{17}B_{\rm hf}\chi_{\rm s}^2(p)$.

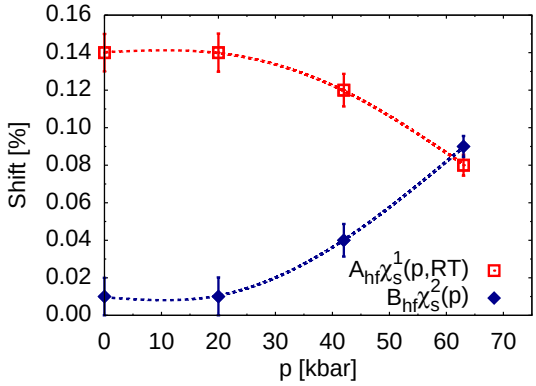

Figure 6.7: Pressure dependence of the two components $^{17}A_{\rm hf}\chi_{\rm s}^1(p,T)$ and $^{17}B_{\rm hf}\chi_{\rm s}^2(p)$ that contribute to the spin shift $^{17}K_{\rm s}(p,T)$ at room temperature. Error bars correspond to an uncertainty in $^{17}B_{\rm hf}\chi_{\rm s}^2(p{=}1$ bar) of $\pm 0.01\%$; dashed lines are a guide to the eye.

300 K) and $^{17}B_{\rm hf}\chi_{\rm s}^2(p)$

$$^{17}A_{\rm hf}\chi_{\rm s}^1(p,T{\approx}300\text{ K}) \approx {}^{17}K_{\rm s}(p,T{\approx}300\text{ K}) - {}^{17}B_{\rm hf}\chi_{\rm s}^2(p) \quad (6.14)$$

$$^{17}B_{\rm hf}\chi_{\rm s}^2(p) = C_p + \kappa_p \times {}^{17}B_{\rm hf}\chi_s^2(1\text{ bar}). \quad (6.15)$$

The drop in the 42 kbar data of almost 0.04% below $T_{\rm c}$, c.f. fig. 6.6, indicates that at this pressure $^{17}B_{\rm hf}\chi_{\rm s}^2(p){\approx}0.04\%$ which allows one to estimate the other values. They can be found in tab. 6.3 and are displayed graphically in fig. 6.7.

It is found that $^{17}B_{\rm hf}\chi_{\rm s}^2(p)$ increases by about a factor of 9 from 0.01% at ambient pressure to about 0.09% at 63 kbar while $^{17}A_{\rm hf}\chi_{\rm s}^1(p,T{\approx}300$ K) decreases by about a factor of 2. These are substantial changes. Furthermore, it is evident that $^{17}B_{\rm hf}\chi_{\rm s}^2(p){\approx}0.01\%$ is small at ambient pressure which may explain why this Fermi liquid like component has not been observed in earlier studies, leading to a single component description of Y1248 previously [105, 106, 128]. In the present work, the presence of this Fermi liquid like component is only revealed due to the scaling of the pseudogap component and application of sufficiently high pressures.

The results of the ^{63}Cu NMR experiments on Y1248 single crystals shall be discussed next in chap. 7 and the combined conclusions of the ^{17}O and ^{63}Cu high pressure NMR experiments will be presented at the end of that chapter.

7 High pressure ^{63}Cu NMR on $YBa_2Cu_4O_8$

In this chapter, the ^{63}Cu NMR shift measurement on $YBa_2Cu_4O_8$ (Y1248) single crystals up to a pressure of 42 kbar will be described. It will be shown that, similar to the spin shift $^{17}K_s(T)$ of planar oxygen, the pseudogap feature in $^{63}K_s(T)$ of planar copper is suppressed with pressure and that a two component description applies. Furthermore, the implications of an observed increase of the quadrupole frequency of planar copper with pressure will be discussed.

7.1 Experimental conditions

In this section, the experimental conditions of the high pressure ^{63}Cu NMR experiments on the Y1248 single crystals will be briefly summarized.

The experiments were performed on pieces of a Y1248 single crystal of initial size $600\times600\times300$ μm^3 and a superconducting transition temperature of $T_c = 82$ K. A batch of such crystals was gratefully provided to our group by Dr. Chengtian Lin from the Max Planck Institute for Solid State Research in Stuttgart, Germany (the sample preparation is described in [121]). It is worth mentioning, that a ^{17}O enrichment of crystals from the batch was attempted as it would allow simultaneous NMR measurements on oxygen and copper. However, for a yet unknown reason these attempts failed and the ^{17}O enrichment was therefore not further pursued[a].

For the experiments at high pressure, two Moissanite anvil cells (MAC) were prepared according to sec. 3.1. The first cell, equipped with anvils of 1.0 mm culet diameter and containing a microcoil of 300 μm diameter and 10 turns, was pressurized to 16 kbar; the second cell, equipped with anvils of 0.8 mm culet diameter and containing a microcoil of 200 μm diameter and 9 turns, was pressurized to 42 kbar. At these pressures, the superconducting transition is expected to occur at a T_c of 90 K (16 kbar) and 100 K (42 kbar)[b]. In each pressure cell, the gasket hole was loaded with a small piece of about $100\times100\times50$ μm^3 from the same crystal and a ruby chip for pressure determination. A 4:1 mixture of methanol:ethanol was used as a pressure transmitting medium at 16 kbar while glycerin was used at 42 kbar. Fig. 7.1, shows the center of the gasket of the pressure cell prepared for the experiments at 42 kbar before filling with glycerin and successive closing.

[a] The attempts to ^{17}O exchange the crystals were carried out under the same conditions as for the Y1248 powder in sec. 6.1, albeit at an increased duration of 2 weeks. After the exchange, the crystals showed a white coating on the surface and no ^{17}O or ^{63}Cu signal could be detected rendering the crystals useless.

[b] The $T_c(p)$ values for 16 and 42 kbar are inferred from high pressure ac-susceptibility data on Y1248 single crystals of a different batch but same source [129] that was gratefully provided to me by Dr. Swee K. Goh from the Shoenberg-Laboratory for Quantum Matter at the Cavendish Laborator, University of Cambridge.

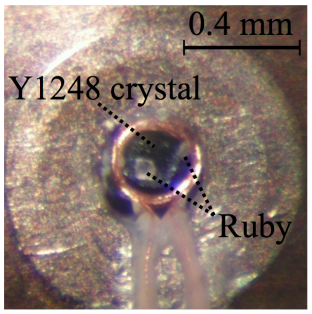

Figure 7.1: Top view, along the axis of the solenoidal microcoil, showing the center of the gasket of the open 42 kbar MAC. The microcoil contains a piece of a Y1248 single crystal and two small ruby chips. The microcoil has an inner diameter of approximately 200 µm.

Copper has two naturally occurring isotopes, i.e. ^{63}Cu and ^{65}Cu. Both have a spin of $I=3/2$ and similar gyromagnetic ratios. Due to the higher natural abundance of ^{63}Cu it is generally favorable to perform the NMR experiments on this isotope. Ambient pressure measurements on a Y1248 single crystal from the same batch were carried out earlier in our group [130, 131] and data from these studies will be used for reference. The high pressure ^{63}Cu-NMR experiments were conducted mostly in a magnetic field of $B_0=17.6$ T in the temperature range from room temperature (297 K) down to about 75 K with the c-axis of the crystal oriented perpendicular to B_0. At 16 kbar, further measurements were carried out at 11.7 T. Spectra were acquired by Fourier transforming the accumulated echo-signal (typically 10^6 scans) following the Hahn echo sequence $\pi/2-\tau-\pi$ with a $\pi/2$-pulse duration (π) of 1 µs (2 µs) and a pulse separation of $\tau=20$ µs at a repetition time of 5 ms. The $\pi/2$- and π-pulse conditions were determined at each temperature by variation of the pulse power P (for example, at 42 kbar and room temperature, the maximum signal was found for $P_{\mathrm{opt}}=1$ W at a measured quality factor of $Q\approx 17$). As a reference for the ^{63}Cu-shifts, the resonance frequency ν_{ref} of ^{63}Cu in metallic copper (powder in epoxy) was used which has a magnetic shift of $^{63}K_{\mathrm{ref}}=3820$ ppm [132]. The Larmor frequency ν_L was then calculated from

$$\nu_L = \frac{\nu_{\mathrm{ref}}}{1+{}^{63}K_{\mathrm{ref}}}. \tag{7.1}$$

7.2 Alignment of the crystals

While placing a crystal inside the microcoil, it was not possible to accurately orient it because of its small size and irregular shape. Furthermore, it could not be ruled out that it moved during application of pressure. To be able to perform the experiments at a well defined orientation with respect to B_0, i.e. $c\perp B_0$, it was therefore necessary to align the crystal after closing of the MAC by changing the orientation of the pressure cell on the probehead. In this section, it will be described how the orientation dependence of the ^{63}Cu NMR resonance frequencies of the planar copper signals were used to determine the alignment of the crystal.

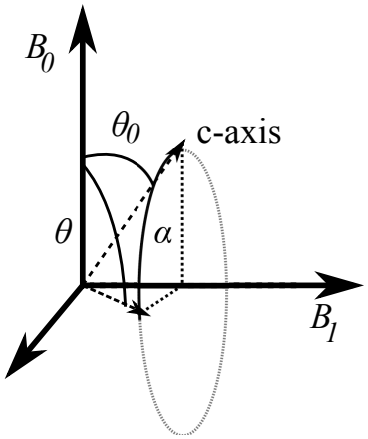

Figure 7.2: Illustration of the change in the angle θ between the c-axis of the crystal and the external magnetic field B_0 upon rotation of the MAC by an angle α. θ_0 is the minimum value of θ that occurs if the c-axis is in the plane generated by B_0B_1.

To ensure that the magnetic field B_1 of the microcoil would remain perpendicular to B_0 while aligning the crystal, the MAC was rotated about the axis that coincides with the direction of B_1; note that this did not require an additional goniometer due to the cylindrical shape of the pressure cell although marks were added to the bottom plate of the MAC to indicate the angle of rotation. In order to demonstrate that the c-axis could indeed be aligned perpendicular to B_0 by this approach, fig. 7.2 illustrates how the angle θ between the c-axis and the direction of B_0 changes if the MAC is rotated around the axis that coincides with the direction of B_1. While rotating, the c-axis moves in a cone around the direction of B_1. Denoting the minimum value of θ during a full revolution by θ_0 (occurs if the c-axis is in the B_0B_1 plane) and the angle of rotation of the MAC away from this minimum by α, the angle θ is given by

$$\cos\theta = \cos\theta_0 \cos\alpha, \tag{7.2}$$

which shows that, regardless of the value of θ_0, the c-axis will be in the plane perpendicular to B_0 and hence $c \perp B_0$ for $\alpha = 90°$.

7.2.1 Angular dependence of the ^{63}Cu resonance frequencies

Next, it will be shown that the resonance frequencies of the planar copper signals display local extrema for $c \perp B_0$ at 17.6 T which was taken advantage of while determining this orientation.

As pointed out in sec. 5.2, the resonance frequencies of the ^{63}Cu signals are influenced by hyperfine and quadrupole effects and one expects $2I = 3$ resonance lines for planar copper at 17.6 T. In the following, the resonance frequency of the ^{63}Cu central transition -1/2 $\leftrightarrow$ 1/2 shall be denoted by ν_0 and those of the two satellite transitions $(m-1) \leftrightarrow m$ with m = -1/2, 3/2 by ν_0^m. Note that up to second order perturbation theory, ν_0 is only affected in second order by quadrupole effects whereas ν_0^m is effected only in first order.

At ambient pressure, the magnetic shift ^{63}K and the electric field gradient for planar copper are known to have axial or nearly axial ($\eta_Q = 0.015$) symmetry with their largest component along the c-axis of the crystal [106]. Thus, up to second order ν_0 and ν_0^m are given by

$$\nu_0(\theta) = [1 + {}^{63}K(\theta)]\nu_L + \delta\nu^{(2)}_{\frac{1}{2}}(\theta) \tag{7.3}$$

$$\nu_0^m(\theta) = [1 + {}^{63}K(\theta)]\nu_L + \delta\nu^{(1)}_m(\theta), \tag{7.4}$$

where θ indicates the angle between the c-axis and B_0, ν_L is the Larmor frequency and $\delta\nu_m^{(1)}$ and $\delta\nu_{1/2}^{(2)}$ denote the first and second order quadrupole shifts. Since the shift terms ^{63}K, $\delta\nu_m^{(1)}$ and $\delta\nu_{1/2}^{(2)}$ depend on the angle θ, so do the resonance frequencies ν_0 and ν_0^m.

Angular dependencies of ^{63}K, $\delta\nu_m^{(1)}$ and $\delta\nu_{1/2}^{(2)}$

First, the angular dependence of $^{63}K(\theta)$ is considered. The isotropic (iso) and anisotropic (ani) magnetic shifts shall be defined as

$${}^{63}K_{\text{iso}} = \frac{1}{3}\left({}^{63}K_{\parallel} + 2 \times {}^{63}K_{\perp}\right) \tag{7.5}$$

$${}^{63}K_{\text{ani}} = \frac{2}{3}\left({}^{63}K_{\parallel} - {}^{63}K_{\perp}\right), \tag{7.6}$$

where $^{63}K_{\parallel}$ and $^{63}K_{\perp}$ are the values of the magnetic shift for an orientation of the c-axis parallel ($\parallel$) and perpendicular ($\perp$) to B_0. $^{63}K(\theta)$ is then given by [15]

$${}^{63}K(\theta) = {}^{63}K_{\text{iso}} + {}^{63}K_{\text{ani}}\frac{(3\cos^2\theta - 1)}{2}. \tag{7.7}$$

The angular dependencies of $\delta\nu_{1/2}^{(2)}$ and $\delta\nu_m^{(1)}$ on the other hand are given by [15]

$$\delta\nu^{(2)}_{\frac{1}{2}}(\theta) = -\frac{\nu_Q^2}{16\nu_L}\left[I(I+1) - \frac{3}{4}\right]\sin^2\theta\left(9\cos^2\theta - 1\right) \tag{7.8}$$

$$\delta\nu_m^{(1)}(\theta) = -\nu_Q\left(m - \frac{1}{2}\right)\frac{3\cos^2\theta - 1}{2}, \tag{7.9}$$

where ν_Q denotes the quadrupole frequency.

In fig. 7.3(a) and 7.3(b), the resulting angular dependencies of the resonance frequencies of the central transition and the satellite transition $1/2 \leftrightarrow 3/2$ are displayed for the ambient pressure and room temperature conditions of $^{63}K_{\parallel} = 1.44\%$, $^{63}K_{\perp} = 0.65\%$ and $\nu_Q = 29.7$ MHz [130, 131] for $\nu_L = 198.303$ MHz, the Larmor frequency of ^{63}Cu in our 17.6 T magnet. A local maximum is observed for the resonance frequency of the central transition (at $\sim$200.4 MHz) and the satellite (at $\sim$ 215.0 MHz) for $\theta = 90°$, i.e. $c \perp B_0$. Note that the -3/2 $\leftrightarrow$ -1/2 satellite transition (not shown) has a minimum for this orientation.

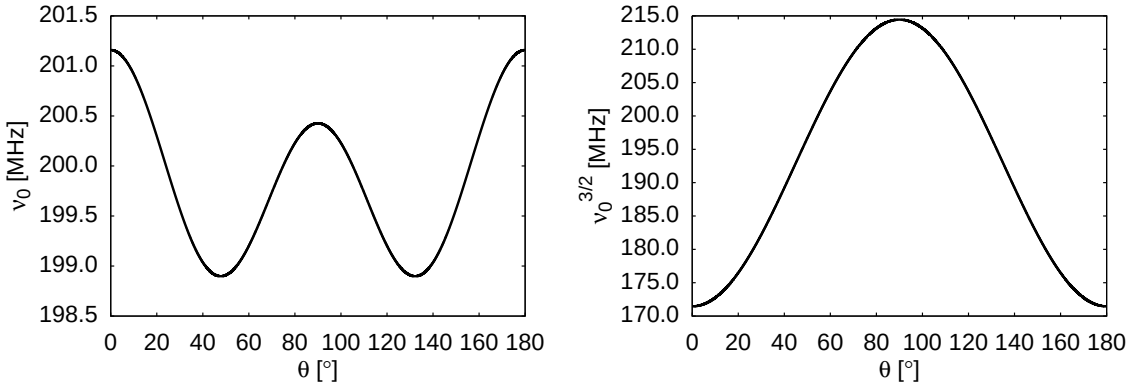

(a) central transition -1/2↔1/2 (b) satellite transition 1/2↔3/2

Figure 7.3: The resonance frequencies of the central transition (a) and the satellite transition $1/2 \leftrightarrow 3/2$ as a function of the angle θ between the c-axis of the crystal and the magnetic field B_0 under ambient pressure conditions and at room temperature for a Larmor frequency of $\nu_L = 198.303$ MHz ($B_0 = 17.6$ T). Both display a local maximum at $\theta = 90°$, which corresponds to an orientation of $c \perp B_0$.

7.2.2 Aligning a crystal at high pressure

As long as the magnetic shift ^{63}K and the quadrupole frequency ν_Q vary within reasonable limits and their corresponding tensors remain (nearly) axially symmetric with their largest component along the c-axis, the ^{63}Cu resonance frequencies of planar copper will display local extrema for an orientation of the c-axis perpendicular to B_0. Because of the absence of a structural phase transition in the investigated pressure range [122] one does not expect the direction of the electric field gradient at planar copper to change significantly and a variation of the charge distribution in the copper oxide plane will cause only relatively small changes of ν_Q [99]. Furthermore, the changes of ^{63}K are expected to be within such reasonable limits as indicated by the ^{17}O NMR experiments of chap. 5. Thus, it is reasonable to assume that at $c \perp B_0$, the resonance frequencies of planar copper also display local extrema in their angular dependence at high pressures up to 42 kbar.

For the purpose of aligning the crystal, it was more convenient to initially use the resonance frequency ν_0 of the central transition as it varies in a smaller frequency range depending on θ (the resonance frequency of the central transition varies within ~ 2 MHz whereas the resonance frequencies of the satellite transitions potentially vary by ~ 45 MHz). The following procedure was therefore carried out at room temperature while aligning the crystal to $c \perp B_0$: first, a rough "scan" was made by rotating the pressure cell about its axis from an initial angle $\alpha' = 0°$ to $\alpha' = 180°$ in steps of 45° and recording ν_0 at each orientation ($\alpha' = \alpha + \alpha_0$ where α is the angle in fig. 7.2 and α_0 is an offset). For both crystals, this already yielded a good indication for the orientation of $c \perp B_0$ as the resonance frequency was found to be around 200.4 MHz for two successive rotations; according to eqn. (7.2) this indicates that θ_0 of fig. 7.2 was relatively close to 90°. Close to these orientations, the local maximum of $\nu_0(\alpha')$ was then searched for

with increasingly higher precision in the rotation angle α' until no significant changes could be detected even after minor rotations. With a linewidth of the central transition of less than 75 kHz, it is estimated that the maximum in the resonance frequency was found within a precision of $\sim$10 kHz which corresponds to an uncertainty in the alignment of the crystal to $c \perp B_0$ of less than 2°. This was deemed sufficient for the temperature dependent shift measurements.

In the case of the crystal at 42 kbar, the precision of the alignment was further improved by applying the same approach to the resonance frequency of the $1/2 \leftrightarrow 3/2$ satellite transition that shows stronger angular dependence (a high precision of the alignment is necessary for an accurate determination of the quadrupole frequency ν_Q). Note however that this is very time consuming due to the low spectral intensity and broader linewidth of this satellite ($\sim$ 200 kHz). It is estimated that this crystal was aligned to $c \perp B_0$ within 1°.

In addition, it is pointed out that after this procedure, the chain copper site Cu(1) is only insufficiently aligned with respect to B_0 since the tensors describing its magnetic shift ^{63}K and the electric field gradient at this site are not axially symmetric around the c-axis [106]. As the NMR parameters of chain copper were of minor interest for the present thesis, it was therefore not attempted to record signal from this copper site.

7.3 Results and discussion

The results of the ^{63}Cu NMR measurements on planar copper will be presented and analyzed next. It will be shown that the characteristic pseudogap temperature dependence of $^{63}K_s(T)$ of planar copper decreases with increasing pressure similar to $^{17}K_s(T)$ of planar oxygen, independently indicating the closing of the pseudogap. Furthermore, an observed increase of the quadrupole frequency with pressure will be discussed in terms of a change of hole concentration in the planar oxygen and planar copper orbitals.

7.3.1 Sample spectra

Typical ^{63}Cu NMR spectra at ambient pressure (1 bar) and high pressures of 16 and 42 kbar of the planar copper Cu(2) central transition for $c \perp B_0$ are shown in fig. 7.4. They were recorded in a magnetic field of $B_0 = 17.6$ T at a temperature of about 250 K. Note that in the 42 kbar spectrum, an additional broad background is observed which is likely caused by a ^{63}Cu satellite from chain copper[c]; the background signal is of minor interest here and will not be further discussed. With increasing pressure, an increase in the resonance frequency and the linewidth of the planar copper signal is observed.

Fig. 7.5 shows room temperature spectra of the two ^{63}Cu satellites and the ^{63}Cu central transition of planar copper recorded at 42 kbar for $c \perp B_0$. The "lower" satellite around 184.6 MHz is caused by the transition -3/2 $\leftrightarrow$ -1/2 and the "upper" satellite at about 214.8 MHz is caused

[c]Compared to the planar copper central transition, this background strongly varies with the orientation of the crystal which indicates that it is a satellite transition.

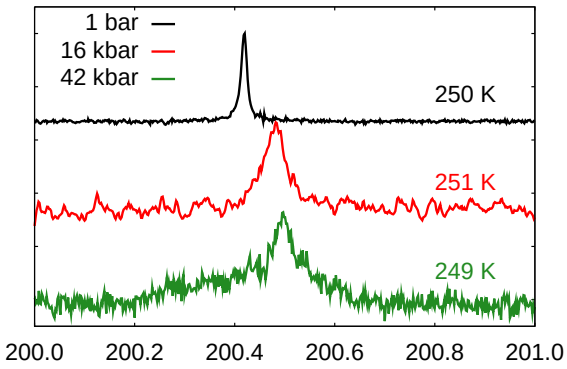

Figure 7.4: Selected ^{63}Cu NMR spectra of the planar copper central transition at ambient pressure (1 bar) and high pressures of 16 kbar and 42 kbar. The data was recorded for $c \perp B_0$ in a magnetic field of 17.6 T at the temperatures indicated in the figure ($\sim$250 K). With increasing pressure, a shift to higher resonance frequencies and an increase in linewidth is observed. The broad background at 42 kbar likely originates from a chain copper satellite.

by the transition $1/2 \leftrightarrow 3/2$. An additional signal in the frequency range of the upper satellite is due to the ^{65}Cu central transition of planar copper which coincidentally has a similar resonance frequency at 17.6 T; it could be distinguished from the ^{63}Cu satellite based on its orientation dependence[d]. It is worth mentioning that the satellites had a linewidth of $\sim$200 kHz at 42 kbar which is small compared to other cuprates and indicates a relatively homogeneous charge distribution in the CuO_2 planes compared to other cuprates [133].

According to eqn. (7.3) and (7.4), the resonance frequencies of the central transition ν_0 and the two satellites ν_0^m for the orientation $c \perp B_0$ are given by

$$\nu_0 = [1 + {}^{63}K_\perp(T)]\nu_L + \frac{3\nu_Q^2}{16\nu_L} \tag{7.10}$$

$$\nu_0^m = [1 + {}^{63}K_\perp(T)]\nu_L \pm \frac{\nu_Q}{2}, \tag{7.11}$$

where $^{63}K_\perp(T)$ denotes the temperature dependent magnetic shift for $c \perp B_0$, ν_L is the Larmor frequency of 198.303 MHz and ν_Q indicates the quadrupole frequency. Note that in eqn. (7.11), the '+' applies to the upper satellite ($m = 3/2$) while the '-' applies to the lower satellite ($m = -1/2$). In the following discussion, the pressure dependence of the quadrupole frequency will be analyzed first in sec. 7.3.2. Then, the effect of pressure on $^{63}K_\perp(T)$ will be investigated in sec. 7.3.4. The observed increase of the linewidth of the central transition will not be addressed as the available data is deemed insufficient to draw rigid conclusions. It is however pointed out that it cannot be caused only by a distribution of the second order quadrupole shift which at 42 kbar and 17.6 T is smaller than $\Delta\delta\nu_{1/2}^{(2)} < 20$ kHz. Furthermore, it appeared to be field independent at 16 kbar (not shown).

[d] Compared to the ^{63}Cu satellite, the resonance frequency of the ^{65}Cu central transition varies only weakly as a function of the angle between the crystal c-axis and B_0

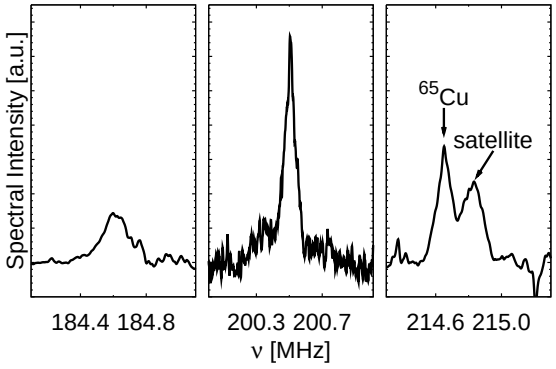

Figure 7.5: ^{63}Cu lower (left) and upper (right) satellite of planar copper at 42 kbar for $c \perp B_0$. The ^{63}Cu central transition (center) is also shown for reference. Note that the upper satellite partly overlaps with the ^{65}Cu central transition of planar copper. All spectra were recorded at 17.6 T at room temperature and normalized according to the number of scans; the data showing the lower/upper satellite were smoothed by apodization with a 10 kHz Gaussian function.

7.3.2 Pressure dependence of the quadrupole frequency

The pressure dependence of the quadrupole frequency ν_Q of planar copper up to ~ 22 kbar[e] is known from earlier NQR measurements [12, 14]. Therefore, we were primarily interested in accurately determining the value of ν_Q at the high pressure of 42 kbar. According to eqn. (7.11), ν_Q at 42 kbar can be calculated directly from the difference in the resonance frequencies of the two satellites. Their values of $\nu_0^{3/2} = 214.81$ MHz (upper satellite) and $\nu_0^{-1/2} = 214.65$ MHz (lower satellite) were determined via Gauss fits resulting in a quadrupole frequency of

$$\nu_Q(42 \text{ kbar}) = \nu_0^{3/2} - \nu_0^{-1/2} = 30.15 \pm 0.05 \text{ MHz}. \tag{7.12}$$

Note that $\nu_0^{3/2}$ and $\nu_0^{-1/2}$ vary considerably as a function of the angle between the c-axis and B_0 even close to $c \perp B_0$ which is the reason why it was necessary to align the crystal within the high precision of 1°.

At 16 kbar, the two satellites were not recorded and the quadrupole frequency was determined via the field dependence of the second order quadrupole shift of the central transition. For this, the resonance frequency of the central transition ν_0 and the Larmor frequency ν_L were measured at room temperature in the magnetic fields of 11.7 T and 17.6 T. According to eqn. (7.10) and with $S = (\nu_0 - \nu_L)/\nu_L$, the quadrupole frequency can then be calculated via (see sec. 7.3.4 for

[e]Note that the authors in [14] give rather crude values for their applied pressures, i.e. 1, 2, and 3 GPa (1 GPa = 10 kbar). Based on the observed superconducting transition temperatures by the authors in [14] (82 K at ambient pressure and 86, 91 and 93 K at high pressure), it is estimated here that their applied pressures are more accurately given by 8, 18 and 22 kbar. This assumption should be justified since T_c in Y1248 increases nearly linear up to about 30 kbar with a slope of ~ 0.5 K/kbar, c.f. for example [119, 120, 134]. The resulting estimated pressures are in a reasonably good agreement with the values given by the authors in [14] except for the highest pressure point at supposedly 3 GPa. I cannot account for the difference but will assume the pressure of 22 kbar to be more realistic.

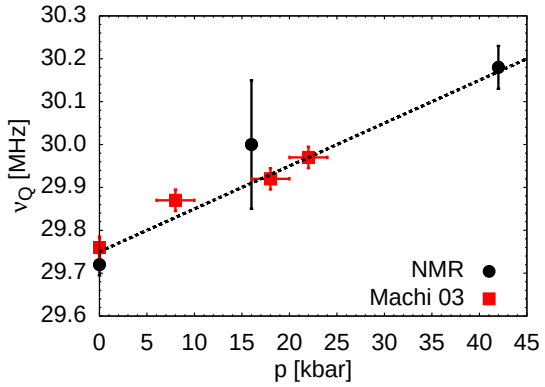

Figure 7.6: Pressure dependence of the quadrupole frequency ν_Q at the planar copper site. Data indicated by '●' are from the present NMR study on the Y1248 single crystals (1 bar from [130] and 16 and 42 kbar determined during the present work) while '■' is from an earlier NQR study by Machi and Koshizuka [14]. The dashed line is a guide to the eye and has a slope of 10 kHz/kbar.

information on how ν_0 was determined)

$$\nu_Q(16\text{ kbar}) = \frac{4}{\sqrt{3}}\sqrt{\frac{S(11.7\text{ T}) - S(17.6\text{ T})}{\frac{1}{\nu_L^2(11.7\text{ T})} - \frac{1}{\nu_L^2(17.6\text{ T})}}} = 30.0 \pm 0.15\text{ MHz}. \tag{7.13}$$

The relatively large uncertainty of ν_Q at 16 kbar reflects the fact that eqn. (7.13) is very sensitive to uncertainties of the different resonance frequencies ν_0 and ν_L.

Including the NQR data from [14] (pressure values according to footnote 'e' on page 90), the pressure dependence of ν_Q of planar copper up to a pressure of 42 kbar is shown in fig. 7.6. Note that the data in [14] was recorded at 100 K while the values for ν_Q from the present NMR experiments were recorded at room temperature. Nevertheless, ν_Q can be assumed to be more or less temperature independent as it changes by less than 20 kHz from room temperature down to 100 K at ambient pressure [135]. Within the uncertainty of the experiments, a linear increase of the quadrupole frequency with a slope of $\sim$10 kHz/kbar is observed up to 42 kbar.

7.3.3 Implications for the hole doping of the copper oxide plane

The origin of this pressure induced increase of ν_Q shall be discussed next. I will follow the argumentation of Haase et al. in [99] and therefore assume that the following effects contribute to the electric field gradient at planar copper: (a) there is a substantial concentration of holes in the $3d_{x^2-y^2}$ orbital of Cu(2); (b) electrons in $2p$ orbitals of neighboring planar oxygen virtually hop to unoccupied $4p$ orbitals of Cu(2); (c) electric fields of distant ions have a non-zero gradient at Cu(2); (d) electric fields of distant ions deform the orbitals of Cu(2).

Based on these contributions, the following expression was derived in [99] for the doping dependence of the quadrupole frequency of planar copper in $YBa_2Cu_3O_{6+x}$ (Y1236:x) and

$La_{1-x}Sr_xCuO_4$

$$\nu_Q = 94.3 \text{ MHz} \times n_d - 5.68 \text{ MHz} \times (8 - 4n_p) + C. \tag{7.14}$$

The term 94.3 MHz$\times n_d$ accounts for effect (a), the term 5.68 MHz$\times(8-4n_p)$ accounts for effect (b) and effects (c) and (d) are summarized in the constant C. The two variables n_d and n_p in eqn. (7.14) denote the hole concentration in the $3d_{x^2-y^2}$ orbital of planar copper and in the $2p$ orbitals of planar oxygen respectively. They are linked to the hole concentration δ (per CuO_2) in the copper oxide plane via

$$\delta = n_d + 2n_p - 1. \tag{7.15}$$

Hereinafter, it will be assumed that eqn. (7.14) holds also true for Y1248 since its structure and electronic properties are very similar to that of Y1236:x[f].

In the investigated pressure range, no structural phase transition occurs in Y1248 and the lattice constants decrease by less than 1% [122] which is comparable to the observed changes in Y1236:x upon variation of the oxygen content [136]. Therefore, one does not expect a significant variation of C in which case the change of the quadrupole frequency is given by

$$\begin{aligned} \Delta\nu_Q(p) &= \nu_Q(p) - \nu_Q(1 \text{ bar}) \\ &\approx 94.3 \text{ MHz} \times [n_d(p) - n_d(1 \text{ bar})] + 22.7 \text{ MHz} \times [n_p(p) - n_p(1 \text{ bar})]. \end{aligned} \tag{7.16}$$

Assuming only a single effect to be relevant, the increase of the quadrupole frequency with increasing pressure then suggests that one of the following two scenarios occurs: (1) holes from the oxygen $2p$ transfer to the copper $3d_{x^2-y^2}$ orbitals or (2) additional holes transfer into the CuO_2 plane and the hole concentration in at least one of the orbitals increases as a result. A transfer of holes from copper to oxygen can be ruled out since it would result in a decrease of ν_Q.

In the case of (1), the hole concentration δ in the CuO_2 planes remains unchanged and a net transfer of Δn_d=-2$\Delta n_p \approx$0.005 holes from oxygen to copper occurs in the pressure range from 1 bar to 42 kbar. Scenario (2) on the other hand implies an increase of δ that would "push" the system closer to optimally doping. The smallest increase in hole concentration would then occur if the additional holes go to the copper only while the maximum increase occurs if they go to the oxygen exclusively. In the latter case, the hole concentration in the CuO_2 plane increases at a rate of $\partial\delta_{\max}(p)/\partial p \approx 0.001$ holes/kbar. Tab. 7.1 (includes the data from [14]) lists the estimated min/max hole concentrations for scenario (2) with a presumed ambient pressure hole concentration of δ=0.136 [99].

Ultimately, without knowledge of the quadrupole frequencies at the planar oxygen sites under pressure, it is not possible to determine the hole concentration in the $2p$ oxygen and the $3d_{x^2-y^2}$

[f]The major difference is that Y1248 contains fully oxygenated double CuO chains while Y1236:x contains only a single CuO chain whose oxygen content may be varied.

p [kbar]	0.001	8	16	18	22	42
$\delta_{\min}(p)$	0.136	0.137	0139	0.138	0.138	0.141
$\delta_{\max}(p)$	0.136	0.146	0.161	0.150	0.155	0.174

Table 7.1: Minimum and maximum increase of the in-plane hole concentration δ upon application of pressure if the increase in quadrupole frequency of planar copper is caused by a charge transfer into the planes (see text for details.)

copper orbitals explicitly and hence distinguish between scenario (1) and (2) [99]. Scenario (2) may be more likely though since there is evidence for a pressure induced hole transfer from the CuO chains to the CuO_2 planes at least up to 16 kbar [137,138] (the decrease of the quadrupole frequency of chain copper under pressure has also been interpreted as evidence for a charge transfer [14, 139]).

If indeed a pressure induced charge transfer into the CuO_2 plane occurs and the holes behave as if chemically doped, one expects the additional holes to more likely reside on the oxygen site [99]. Consequently, one would expect the in-plane hole concentration to be close to the values of $\delta_{\max}(p)$ in tab. 7.1. Such an increase of the hole concentration would certainly affect the in-plane spin susceptibility $\chi_s(T)$ and hence $^{17,63}K_s(T)$ as well. Interestingly though, at 42 kbar the pseudogap feature in $^{63}K_s(T)$ is still present, see sec. 7.3.4, while in Y1236:x for hole concentrations similar to $\delta_{\max}(p)$ at 42 kbar, the spin shift is found to be T-independent above T_c.

Comparison of the effect of chemical doping and pressure on T_c

An additional comparison of chemical doping and application of pressure in Y1248 shall be made via their effect on the superconducting transition temperature.

Unlike Y1236:x, Y1248 cannot be chemically doped by changing the oxygen content in the CuO chains. Instead, its hole content in the CuO_2 plane is typically increased by replacing the Y^{3+} between the CuO_2 planes (see fig. 5.3) with Ca^{2+} [121]. However, there is evidence that at high Ca-doping, Ca^{2+} also partially replaces Ba^{2+} which may result in an effectively lower hole concentration [135]. Furthermore, it should be noted that substituting ions of different ionic radii will also cause chemical pressure. Thus, chemical doping is certainly not as "clean" as the application of pressure.

Fig. 7.7 shows the T_c vs. Ca-content 'x' (top x-scale) data for nominally $Y_{1-x}Ca_xBa_2Cu_4O_8$ from [121]. If the Ca^{2+} replaces Y^{3+} only, the top x-scale is equivalent to the bottom x-scale which represents the in-plane hole concentration (note that there is one Y/Ca per two CuO_2 in the planes). Indicated by the shaded green area is the potential hole concentration under pressures of up to 42 kbar assuming that either an in-plane transfer of holes from oxygen to copper occurs and/or a hole transfer into the plane takes place (except for the 16 kbar data points which are excluded due to the large uncertainty, the values of $\delta_{\min}(p)$ (●) and $\delta_{\max}(p)$ (■) from tab. 7.1 are also included). It appears that, regardless of wether scenario (1) or (2)

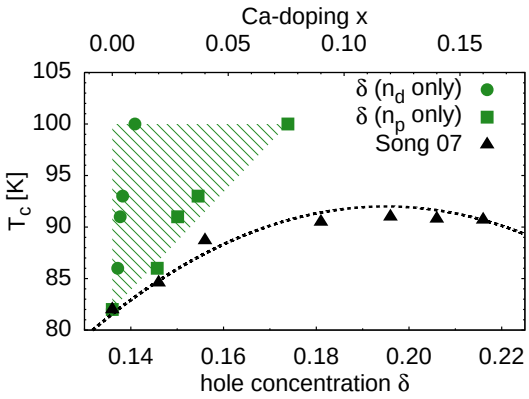

Figure 7.7: Comparison of the effect of chemical doping and pressure on the superconducting transition temperature T_c in Y1248. The shaded green area indicates the potential hole concentration under pressure up to 42 kbar according to the analysis of the increase of the planar copper quadrupole frequency (corresponding values of $\delta_{min}(p)$ (●) and $\delta_{max}(p)$ (■) from tab. 7.1 are also indicated). The increase of T_c upon Ca-doping (top x-scale) is indicated by (Song 07 ▲) and represents data from [121]. The dashed line is intended as a guide to the eye for the Ca-doping data.

applies, higher values of T_c are achieved under pressure for similar in-plane hole concentrations even at low Ca-doping. This in turn indicates that applying pressure to Y1248 is more effective in increasing T_c than chemically doping and that the increase of T_c under pressure is not simply related to a charge transfer as suggested earlier [134, 140]. However, it is beyond the scope of this thesis to speculate on the origin of the additional increase in T_c under pressure.

7.3.4 Effect of pressure on $^{63}K_\perp(T)$

The effect of pressure on the temperature dependence of the spin component $^{63}K_s(T)$ of the magnetic shift $^{63}K_\perp(T)$ for planar copper will be investigated next. It will be shown that, similar to the ^{17}O NMR experiments discussed in sec. 6.2.3, $^{63}K_s(p,T)$ signals the closing of the pseudogap under pressure.

First, it is pointed out that in the investigated temperature range the effect of diamagnetic shielding is expected to be negligible [125]. Hence, $^{63}K_\perp(T)$ should contain only the T-independent orbital term $^{63}K_l$ and the T-dependent spin term $^{63}K_s(T)$ that arises from the coupling of the planar copper nuclei to the spin susceptibility $\chi_s(T)$

$$^{63}K_\perp(T) = {}^{63}K_l + {}^{63}K_s(T). \tag{7.17}$$

To determine the effect of pressure on $^{63}K_\perp(T)$, the temperature dependence of the resonance frequency ν_0 of the ^{63}Cu central transition was measured at the high pressures of 16 kbar and 42 kbar (as the 1 bar reference, data from an earlier NMR investigation carried out in our group [131] on a Y1248 single crystal from the same batch is used). The central transition resonance line of planar copper in Y1248 has a Lorentzian shape [106]. Thus, the p- and T-

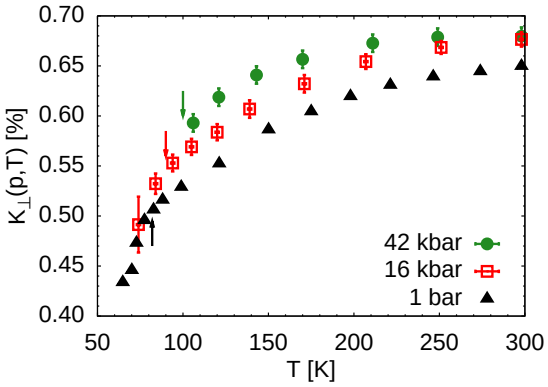

Figure 7.8: Temperature dependence of the magnetic shift $^{63}K_\perp(T)$ of planar copper Cu(2) at 1 bar (data from [131]) and high pressures of 16 and 42 kbar. Error bars represent the linewidth of the Cu(2) signal and T_c values are indicated by the arrows.

dependent resonance frequency ν_0 was extracted by fitting a Lorentzian function

$$f(\nu) = \frac{A}{\pi} \frac{\frac{\sigma}{2}}{(\nu - \nu_0)^2 + \frac{\sigma^2}{4}} \tag{7.18}$$

to a particular spectrum (A is a normalization factor and σ denotes the linewidth factor). According to eqn. (7.10), $^{63}K_\perp(p,T)$ is then given by

$$^{63}K_\perp(p,T) = \frac{\nu_0(p,T)}{\nu_L} - \frac{3\nu_Q^2(p)}{16\nu_L^2} - 1. \tag{7.19}$$

In fig. 7.8, the temperature dependence of the magnetic shift $^{63}K_\perp(p,T)$ at the various pressures are shown (T_c values indicated by arrows). Due to limitations in the SNR in the superconducting state, measurements were carried out mostly in the normal state above T_c. It is pointed out that the ambient pressure data is in excellent agreement with earlier studies on aligned Y1248 powder samples [106, 141] except for an offset of 0.15%. This offset is likely attributable to the use of a different reference compound[g].

At ambient pressure, $^{63}K_\perp(T)$ shows the characteristic pseudogap behavior similar to $^{17}K(T)$ of O(2,3), c.f. fig. 6.5, and decreases with decreasing temperature already above T_c. Below T_c, a distinct drop in $^{63}K_\perp(T)$ by about 0.05% is observed; It is pointed out that this drop is also present in the ambient pressure ^{63}Cu NMR data of Bankay et al. [106] and that in [106] $^{63}K_\perp(T)$ smoothly decreases again at lower temperatures. With increasing pressure, $^{63}K_\perp(T)$ increases for all temperatures above T_c and becomes less T-dependent in the normal state. At 16 kbar, the onset of a drop in $^{63}K_\perp(T)$ below T_c is also apparent (for 42 kbar, no data was taken below T_c).

The orbital shift of $^{63}K_l = 0.4\%$ at ambient pressure [106] is quite large and cannot be simply

[g] In earlier studies, CuCl was typically used as a reference for the Larmor frequency. However, CuCl is paramagnetic and has a magnetic shift of $^{63}K = 0.15\%$ [132].

neglected as was the case for planar oxygen. Unfortunately, its value at higher pressure could not be determined in our experiments due to the low SNR in the superconducting state. Nevertheless, since the lattice parameters change only slightly in the investigated pressure range [122], it should be reasonable to assume that $^{63}K_{\parallel}$ changes insignificantly from its ambient pressure value up to 42 kbar. In that case, the observed changes of $^{63}K_{\perp}(T)$ with pressure must be related to the spin shift $^{63}K_{\rm s}(T)$

$$^{63}K_{\rm s}(p,T) \approx \ ^{63}K_{\perp}(p,T) - 0.4\%. \tag{7.20}$$

Fig. 7.8 then shows that $^{63}K_{\rm s}(T)$ becomes increasingly T-independent and hence Fermi liquid like above $T_{\rm c}$ (note that the range of the y-scale in fig. 7.8 was chosen so that it only displays the presumed spin shift contribution of $^{63}K_{\perp}(T)$). Thus, similar to the ^{17}O NMR shifts in chap. 6, the pressure evolution of $^{63}K_{\perp}(T)$ indicates the closing of the pseudogap under pressure.

Scaling behavior and two component description of $^{63}K_{\rm s}(p,T)$ of planar copper

Next, it will be checked wether the high pressure $^{63}K_{\rm s}(p,T)$ data of planar copper also display a scaling behavior in $^{63}K_{\rm s}(1\text{ bar},T)$ as was the case for planar oxygen (see sec. 6.2.4) and consequently wether a two component description of $^{63}K_{\rm s}(p,T)$ is required.

Fig. 7.9 shows a plot of the planar copper $^{63}K_{\rm s}(p,T)$ at high pressures vs. $^{63}K_{\rm s}(1\text{ bar},T)$ using temperature as an implicit parameter (T was parametrized via a polynomial fit to the $^{63}K_{\rm s}(1\text{ bar},T)$ data). Like in sec. 6.2.4 for planar oxygen, it is found that at temperatures above $T_{\rm c}$ the high pressure data are well described by a linear relation in $^{63}K_{\rm s}(1\text{ bar},T)$

$$^{63}K_{\rm s}(p,T) = \kappa_p \times {}^{63}K_{\rm s}(1\text{ bar},T) + C_p, \tag{7.21}$$

where the pressure dependent constants κ_p decreases with p while C_p increases (their values determined via a least square fit can be found in tab. 7.2). A deviation from the linearity is again observed almost only in the vicinity of $T_{\rm c}$ and below where $^{63}K_{\rm s}(p,T)$ drops considerably and approaches the dashed line representing the 1 bar data. However, at 42 kbar a deviation is also apparent at high temperatures where $^{63}K_{\rm s}(p,T)$ appears to be constant above ~ 250 K. This may indicate that the temperature below which $^{63}K_{\rm s}(T)$ becomes T-dependent and therefore displays the pseudogap behavior decreases with pressure (at ambient pressure, $^{63}K_{\rm s}(T)$ becomes T-independent slightly above room temperature [124]). It is further pointed out that the values of κ_p for planar copper are somewhat smaller than for planar oxygen at comparable pressures. A potential explanation may be the different sample preparation which could influence the electronic properties of the material somewhat.

In sec. 6.2.4 it was shown that a behavior of $^{63}K_{\rm s}(p,T)$ according to eqn. (7.21) implies a two component spin shift of the form

$$^{63}K_{\rm s}(p,T) = \ ^{63}A_{\rm hf}\chi_{\rm s}^{1}(p,T) + \ ^{63}B_{\rm hf}\chi_{\rm s}^{2}(p), \tag{7.22}$$

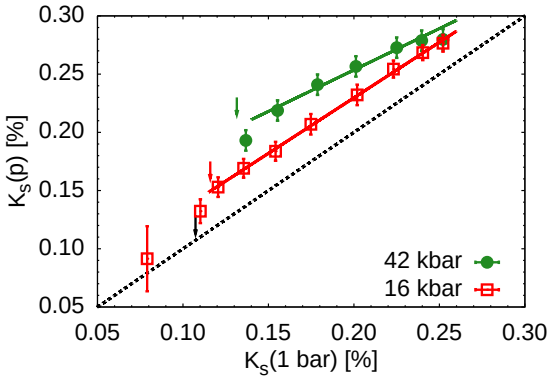

Figure 7.9: $^{63}K_s(p,T)$ vs. $^{63}K_s(1\text{ bar},T)$ of planar copper using temperature as an implicit parameter. As indicated by the solid lines, $^{63}K_s(p,T)$ is found to be well described by a linear relation in $^{63}K_s(1\text{ bar},T)$ above the superconducting state. The dashed diagonal line of slope 1 represents $^{63}K_s(1\text{ bar},T)$. T_c values are indicated by the arrows.

p [kbar]	16	42
κ_p	0.95	0.71
C_p [%]	0.04	0.11

Table 7.2: Pressure dependent values of κ_p and C_p.

where only $^{63}A_{hf}\chi_s^1(p,T)$ displays the characteristic pseudogap T-dependence while $^{63}B_{hf}\chi_s^2(p)$ remains T-independent above T_c ($^{63}A_{hf}$ and $^{63}B_{hf}$ are the two hyperfine coupling constants). Thus it can be concluded that a two component description also applies to $^{63}K_s(p,T)$ of planar copper. Just like in the case of planar oxygen, the first component $^{63}A_{hf}\chi_s^1(p,T)$ is suppressed with pressure whereas $^{63}B_{hf}\chi_s^2(p)$ becomes increasingly significant with pressure.

Since the spin shifts of planar oxygen and planar copper behave similar under pressure, it is reasonable to assume that both sites couple to the same two spin susceptibilities $\chi_s^1(p,T)$ and $\chi_s^2(p)$ in the CuO_2 plane. In that case, $^{63}A_{hf}\chi_s^2(p,T)$ should display a smooth T-dependence through T_c while $^{63}B_{hf}\chi_s^2(p)$ is Fermi liquid like and rapidly decreases below (both components are expected to vanish or at least become very small approaching $T = 0$ K). The drop in $^{63}K_s(T)$ at ambient pressure below T_c, c.f. fig. 7.8, and the deviation from the linearity in fig. 7.9 at higher pressure in the vicinity of T_c then likely represent this rapid decrease of $^{63}B_{hf}\chi_s(p,T)$. That at 42 kbar, the drop appears to occur already slightly above T_c could again be due to an inhomogeneity of the pressure across the sample or be caused by superconducting fluctuations [127].

Pressure evolution of the two components and comparison with oxygen

Finally, the pressure dependent values of $^{63}A_{hf}\chi_s^2(p,T)$ at room temperature and $^{63}B_{hf}\chi_s^2(p)$ for planar copper will be determined and compared to their corresponding counterparts for planar oxygen. From the rapid drop of $^{63}K_s(T)$ of 0.05% below T_c at ambient pressure, c.f. fig. 7.8,

p [kbar]	0.001	16	42
$^{63}A_{\rm hf}\chi_{\rm s}^1(p,{\rm RT})$ [%]	0.20	0.17	0.13
$^{63}B_{\rm hf}\chi_{\rm s}^2(p)$ [%]	0.05	0.09	0.15

Table 7.3: Pressure dependent values of $^{63}A_{\rm hf}\chi_{\rm s}^1(p,T)$ at room temperature and $^{63}B_{\rm hf}\chi_{\rm s}^2(p)$.

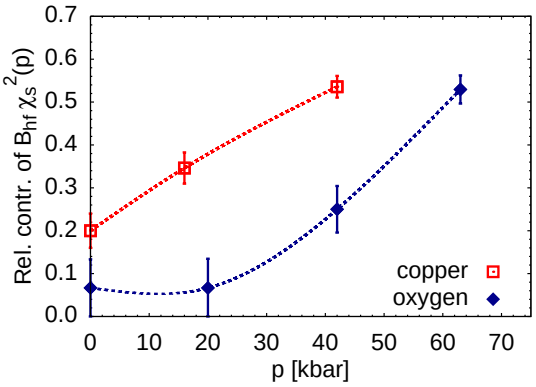

Figure 7.10: Comparison of the relative shift contribution $^nB_{\rm hf}\chi_{\rm s}^2(p)/^nK_{\rm s}(p,{\rm RT})$ ($n=17,\ 63$) of the Fermi liquid like component at planar oxygen and planar copper. Dashed lines are a guide to the eye.

it is estimated that $^{63}B_{\rm hf}\chi_{\rm s}^2(p)\approx 0.05\%$ at 1 bar. Using eqn. (6.14) and eqn. (6.15) from the previous chapter, the remaining values of $^{63}A_{\rm hf}\chi_{\rm s}^1(p,{\rm RT})$ and $^{63}B_{\rm hf}\chi_{\rm s}^2(p)$ are calculated; they can be found in tab. 7.3.

Up to 42 kbar it is found that $^{63}B_{\rm hf}\chi_{\rm s}^2(p)$ increases by about a factor of 3 from 0.05% to 0.15% whereas $^{63}A_{\rm hf}\chi_{\rm s}^1(p,{\rm RT})$ decreases by about a factor of 1.5. This is more or less comparable to the relative changes of the two components observed in the spin shift of planar oxygen, c.f. tab. 6.3 on page 82. As shown in fig. 7.10, the contribution of the Fermi liquid like component $^nB_{\rm hf}\chi_{\rm s}^2(p)$ ($n=17,\ 63$) to the total spin shift appears to be larger for planar copper than for planar oxygen at comparable pressures. Wether this is related to the different sample preparation of the two samples investigated or due to a stronger coupling of the copper nuclei to $\chi_{\rm s}^2(p)$ than the oxygen nuclei cannot be determined free of doubt.

7.4 Conclusions

To conclude, ^{17}O and ^{63}Cu NMR shift measurements on the high temperature superconductor $YBa_2Cu_4O_8$ up to a pressure of 63 kbar were performed. With increasing pressure the spin shifts $^{17}K_{\rm s}(p,T)$ of planar oxygen and $^{63}K_{\rm s}(p,T)$ of planar copper are found to increase and become less temperature dependent above $T_{\rm c}$. This behavior indicates the suppression of the pseudogap with pressure and is similar to the effect of doping in other cuprates [9, 142].

Furthermore, the observation of a scaling of the spin shifts with pressure is ascribed to the presence of a two component spin susceptibility in the CuO_2 plane. One component displays the

pseudogap temperature dependence and decreases with pressure while the second component is Fermi liquid like and increases with pressure. This is in agreement with earlier ambient pressure studies on $La_{1.85}Sr_{0.15}CuO_4$ [108] and $HgBa_2CuO_{4+\delta}$ [111, 112] and suggests that a two component description of the in-plane spin susceptibility is a common feature in cuprates. However, the individual components may be small under certain conditions which in fact lead to a single component description of $YBa_2Cu_4O_8$ earlier [106, 128]. In the present work, the presence of the Fermi liquid like component is only revealed due to the application of sufficiently high pressures.

Finally, an almost linear increase of the ^{63}Cu quadrupole frequency of planar copper up to 42 kbar is observed. It can be understood either by an in-plane hole transfer from oxygen $2p$ orbitals to the copper $3d_{x^2-y^2}$ orbitals or an increase of the hole concentration in the CuO_2 plane due to a charge transfer as indicated earlier [137,138]. In the latter case, the increase of the hole concentration in the CuO_2 plane is unlikely to exceed a rate of $\Delta\delta/\Delta p \approx 0.001$ holes/kbar which is insufficient in explaining the rapid increase of T_c under pressure. Further experiments are required to clarify the role of the hole transfer in the closing of the pseudogap at high pressure.

8 Summary, conclusions and outlook

In the present work, a novel probe design for high pressure NMR experiments in gem anvil cells (GAC) was used which places a small microcoil inside the high pressure volume as the detection coil. Based on tests carried out at ambient pressure and high pressure of 42 kbar it is demonstrated that this approach is indeed feasible and results in an increase of sensitivity by two orders of magnitude compared to previous GAC-NMR designs. The design was then successfully employed in the investigation of the electronic properties of metallic aluminum and the high temperature superconductor $YBa_2Cu_4O_8$ at pressures of up to 101 kbar. Because of its improved sensitivity and the potential to achieve even higher pressures, the microcoil GAC-NMR setup should prove useful in the investigation of materials under high pressure conditions in the future.

In the case of metallic aluminum, the effect of pressure on the electronic density of states at the Fermi level was probed via the Knight-shift K and the spin-lattice relaxation time T_1 at room temperature up to a pressure of 101 kbar, extending the pressure range of previous NMR measurements by a factor of 14 [72]. Most notably, a decrease of $K(p)$ by 11% is detected in the investigated pressure range that is inconsistent with a free electron behavior of the density of states. Numerical band structure calculations that are in excellent agreement with the experimental data suggest that the observed changes of K and T_1 are due to a kink in the electronic states at a Lifshitz-transition at about 75 kbar which has not been observed previously. A further decrease of K by a factor of 2 is predicted to occur in the pressure range up to 300 kbar.

In addition, an increase of the NMR linewidths of the metallic aluminum signal was observed above about 42 kbar that is inconsistent with a pure dipolar linewidth. Based on an analysis of the field dependence of this effect it was ascribed to a small additional quadrupolar broadening which is rather unexpected given the cubic symmetry of the lattice. Wether this quadrupolar broadening is caused by strain in the sample or is the manifestation of a charge density variation that breaks the cubic symmetry remains unclear.

To investigate the effect of pressure on the pseudogap of high temperature superconductors, temperature dependent ^{17}O and ^{63}Cu NMR shift measurements were carried out on $YBa_2Cu_4O_8$ up to 63 kbar for the first time. These experiments reveal that with increasing pressure the spin shift $^{17}K_s(p,T)$ of planar oxygen and the spin shift $^{63}K_s(p,T)$ of planar copper increase and become more Fermi liquid like above the superconducting transition temperature T_c. At first glance this seems similar to the effect of doping in other high temperature superconductors [9,142] and indicates the closing of the pseudogap with pressure. Wether or not this represents a general

behavior of cuprates under pressure remains to be determined in the future by investigating other high temperature superconductors under comparable conditions.

Furthermore, based on a scaling behavior of the spin shifts with pressure it is concluded that a two component spin susceptibility is present in the copper-oxide plane. One component displays the pseudogap temperature dependence and decreases with pressure while the other component is Fermi liquid like and increases strongly with pressure. However, the Fermi liquid like component is small at ambient pressure which may explain why earlier shift data of $YBa_2Cu_4O_8$ have been interpreted in terms of a single component spin susceptibility [106, 128]. In the present work, its presence is only revealed due to the application of sufficiently high pressures. The two components in $YBa_2Cu_4O_8$ are similar to those observed in recent ambient pressure studies on $La_{1.85}Sr_{0.15}CuO_4$ [108] and $HgBa_2CuO_{4+x}$ [111, 112], indicating that a two component spin susceptibility in the copper-oxide plane is a common feature of cuprates.

Finally, an almost linear increase of the ^{63}Cu quadrupole frequency of planar copper in $YBa_2Cu_4O_8$ up to 42 kbar is observed. It is attributable either to a pressure induced hole transfer from the planar oxygen $2p$ orbitals to the planar copper $3d_{x^2-y^2}$ orbitals or to a pressure induced hole transfer into the copper-oxide plane. The latter may be more likely since earlier transport measurements up to 16 kbar identified a pressure induced hole transfer from the copper-oxide chains to the copper-oxide plane in this material [137, 138]. However, such a hole transfer into the copper-oxide plane is found to be insufficient to explain the rapid increase of T_c in $YBa_2Cu_4O_8$ under pressure as was suggested earlier [134]. Further experiments are required to determine the hole distribution in the copper-oxide plane and to clarify the role of the hole transfer in the closing of the pseudogap in $YBa_2Cu_4O_8$ at high pressure.

In conclusion it can be said that research at very high pressure gives a unique insight into the physics of materials that is also pivotal for their understanding at ambient pressure. However, up until now many physical properties were inaccessible under such extreme conditions due to a lack of suitable experimental probes. In this regard, NMR at very high pressure offers new information and will therefore prove to be an important tool in the future.

9 Appendix

9.1 Properties of a capacitively coupled resonant circuit

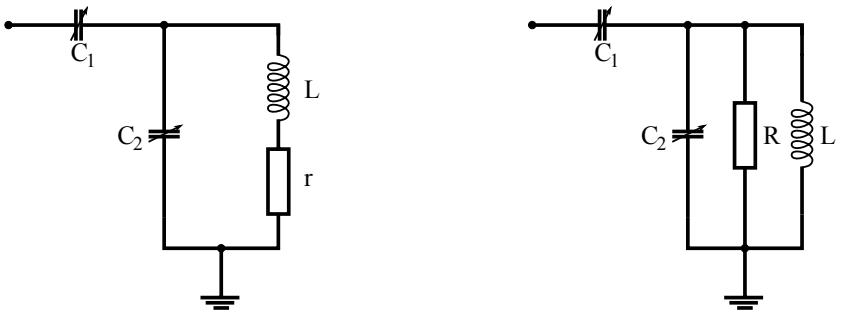

(a) Resonant circuit (b) Equivalent circuit

Figure 9.1: (a) Circuit diagram of a resonant circuit commonly used in NMR experiments from fig. 2.2 shown here again for convenience. (b) Equivalent circuit diagram of the resonant circuit with $R=(\omega L)^2/r$ under the assumption $\omega L \gg r$ [21] typically realized in NMR experiments.

Fig. 9.1(b) shows an equivalent circuit diagram of the capacitively coupled resonant circuit of fig. 2.2 used in the NMR experiments under the condition $\omega L \gg r$ with $R=(\omega L)^2/r$. Starting point is the impedance $\underline{Z}$ of the equivalent circuit diagram given by

$$\begin{aligned} \underline{Z} &= \frac{1}{i\omega C_1} + \frac{1}{\frac{1}{R} + i\left\{\omega C_2 - \frac{1}{\omega L}\right\}} \\ &= \frac{R}{1+R^2B^2} - i\left\{\frac{1}{\omega C_1} + \frac{R^2 B}{1+R^2B^2}\right\} \end{aligned} \tag{9.1}$$

with B defined as

$$B = \omega C_2 - \frac{1}{\omega L}. \tag{9.2}$$

In resonance, the imaginary part of eqn. (9.1) vanishes, i.e. $\mathrm{Im}\{\underline{Z}\}=0$. Furthermore, the real part of eqn. (9.1) must be matched to the 50 Ω of the spectrometer, hence $Z_w = Re\{\underline{Z}(\omega=\omega_0)\} = 50\ \Omega$ is required. Thus the conditions are

$$0 = \frac{1}{\omega_0 C_1} + \frac{R^2 B}{1+R^2B^2} \tag{9.3}$$

$$Z_w = \frac{R}{1+R^2B^2}, \tag{9.4}$$

where ω_0 in eqn. (9.3) denotes the angular resonance frequency. From eqn. (9.4) B can be expressed as

$$B = -\frac{1}{R}\left(\frac{R}{Z_w} - 1\right)^{\frac{1}{2}}. \tag{9.5}$$

Inserting this expression in eqn. (9.3) for the case of $R/Z_w \gg 1$[a] yields

$$\begin{aligned} \frac{1}{\omega_0 C_1} &= \frac{R^2 \frac{1}{R}\sqrt{\frac{R}{Z_w} - 1}}{1 + \frac{R}{Z_w} - 1} = Z_w \sqrt{\frac{R}{Z_w} - 1} \\ &\approx \sqrt{R Z_w}. \end{aligned} \tag{9.6}$$

Hence for B follows with $R/Z_w \gg 1$

$$B \approx -\frac{1}{\sqrt{R Z_w}} = -\omega_0 C_1. \tag{9.7}$$

With the original definition of B in eqn. (9.2) it follows that

$$\begin{aligned} \frac{1}{\omega_0 L} &\approx \omega_0 \left(C_1 + C_2\right) \\ \omega_0^2 &\approx \frac{1}{L\left(C_1 + C_2\right)}, \end{aligned} \tag{9.8}$$

which readily gives the term for the resonance frequency $f_0 = \omega_0/2\pi$. Using eqn. (9.8), eqn. (9.6) and $R = \omega_0^2 L^2/r$ one obtains for the input impedance Z_w in the case of resonance

$$Z_w \approx r\left(\frac{C_1 + C_2}{C_1}\right)^2. \tag{9.9}$$

From eqn. (9.9) it is obvious that the capacitor C_1 primarily affects the matching of the resonant circuit while C_2 can be used to adjust the resonance frequency according to eqn. (9.8).

[a] With the microcoils used, the ratio $R/Z_w \approx 10$.

9.2 Calculation of the $\pi/2$-pulse length

As discussed in sec. 2.1 knowledge of the $\pi/2$- and π-pulse length are important for the NMR experiment and should be predictable by knowing the properties of the rf-coil. Here a derivation for an estimate of $\tau_{\pi/2}$ will be presented.

The pulse length $\tau_{\pi/2}$ is defined as the pulse length for which $\gamma B_1 \tau_{\pi/2} = \pi/2$. Hence B_1 has to be estimated first. The energy stored in the magnetic field of the solenoid coil of inductance L is given by

$$\frac{1}{2} L i^2 = \frac{1}{2\mu_0} B_{\mathrm{rf},0}^2 V_{\mathrm{c}}, \tag{9.10}$$

where i denotes the current running through the coil while $B_{\mathrm{rf},0}$ and V_{c} denote the amplitude of the magnetic field and the volume of the coil respectively. The power consumed in the coil is given by

$$P = \frac{1}{2} r i^2, \tag{9.11}$$

where r denotes the ohmic resistance of the coil. Rearranging eqn. (9.11) for i^2 and inserting into eqn. (9.10) results in

$$\frac{LP}{r} = \frac{1}{2\mu_0} B_{\mathrm{rf},0}^2 V_{\mathrm{c}}. \tag{9.12}$$

Since $2B_1 = B_{\mathrm{rf},0}$, rearrangement yields

$$B_1 = \sqrt{\frac{\mu_0 LP}{2rV_{\mathrm{c}}}}. \tag{9.13}$$

Using the definition of $\gamma B_1 \tau_{\pi/2} = \pi/2$ one gets for $\tau_{\pi/2}$

$$\tau_{\pi/2} = \sqrt{\frac{\pi^2 r V_{\mathrm{c}}}{2\gamma^2 \mu_0 LP}} \tag{9.14}$$

which, using $Q = L\omega_0/r$, is equivalent to

$$\tau_{\pi/2} = \sqrt{\frac{\pi^2 \omega_0 V}{2\gamma^2 \mu_0 QP}}. \tag{9.15}$$

9.3 Titanium alloy pressure cell

During the course of this thesis, piston-cylinder type moissanite anvil cells (MAC) based on the design by Dunstan and Spain [32] and similar to the MACs from Cambridge were build. While not used in the experiments described in this thesis, they have been successfully employed in NMR-experiments up to 97 kbar [53]. The cell will be briefly described in this section.

Material

The MACs are made out of the titanium alloy Ti-6Al-4V (6% aluminum, 4% vanadium and titanium balance) which has a tensile strength of 950 N/mm^2 in the annealed state. In principle the copper alloy beryllium-copper (BeCu) C17200 (1.8% beryllium, 0.2% cobalt and nickel, copper balance) would be a better choice due to the higher tensile strength 1300 N/mm^2 in the fully hardened state. However, as BeCu contains small amounts of highly toxic beryllium that might escape during machining, special safety precautions are required while handling in the work shop. In addition, BeCu has to be machine worked in the annealed state, as it is too hard otherwise. In order to be able to achieve the precision required in a piston-cylinder GAC, further machining of the parts is necessary after hardening due to the change in dimensions of the parts following the hardening via heating to high temperatures followed by quenching. These problems can be avoided by using Ti-6Al-4V in the annealed state. Furthermore, Ti-6Al-4V is considerably cheaper and contains no copper, yielding the prospect of a completely copper free setup that might be advantageous in the study of some cuprates.

Components

A blow-up sketch of the MAC is shown in fig. 9.2, the blue-prints of the different parts can be found on page 107 through 112. The exterior of the cell is composed of the top plate, the cylinder and the bottom plate while the interior is composed of the piston, the xy-plate, two anvils and a gasket. In addition, a variety of screws, i.e. two clamping screws, a piston screw, three xy-screws, a guiding pin and three bottom screws are included.

The cell works on the principle of the piston-cylinder DAC explained in sec. 2.3.1. The piston fits tightly into the cylinder in order to guarantee proper parallel alignement of the culets of the anvils and the guiding pin, a simple screw with a conic top, in conjunction with the indentation on the piston prevents it from rotating in the cylinder. A hole in the center of the piston allows optical access of the high pressure region while the three holes on the outer rim act as feedthroughs for wires.

With the exception of the clamping screws, all screws were made of simple brass as no large force is applied to them. The clamping screws are made from the same Ti-6Al-4V and are used to clamp the applied pressure (pressure is applied via a hydraulic press). The three bottom screws are used to connect the bottom plate to the cylinder while the piston screw connects the piston to the top plate, simplifying extraction of the piston from the cylinder during preparation. The

three xy-screws are used to align the xy-plate. Three holes above the xy-screws allow optical access while aligning the anvils.

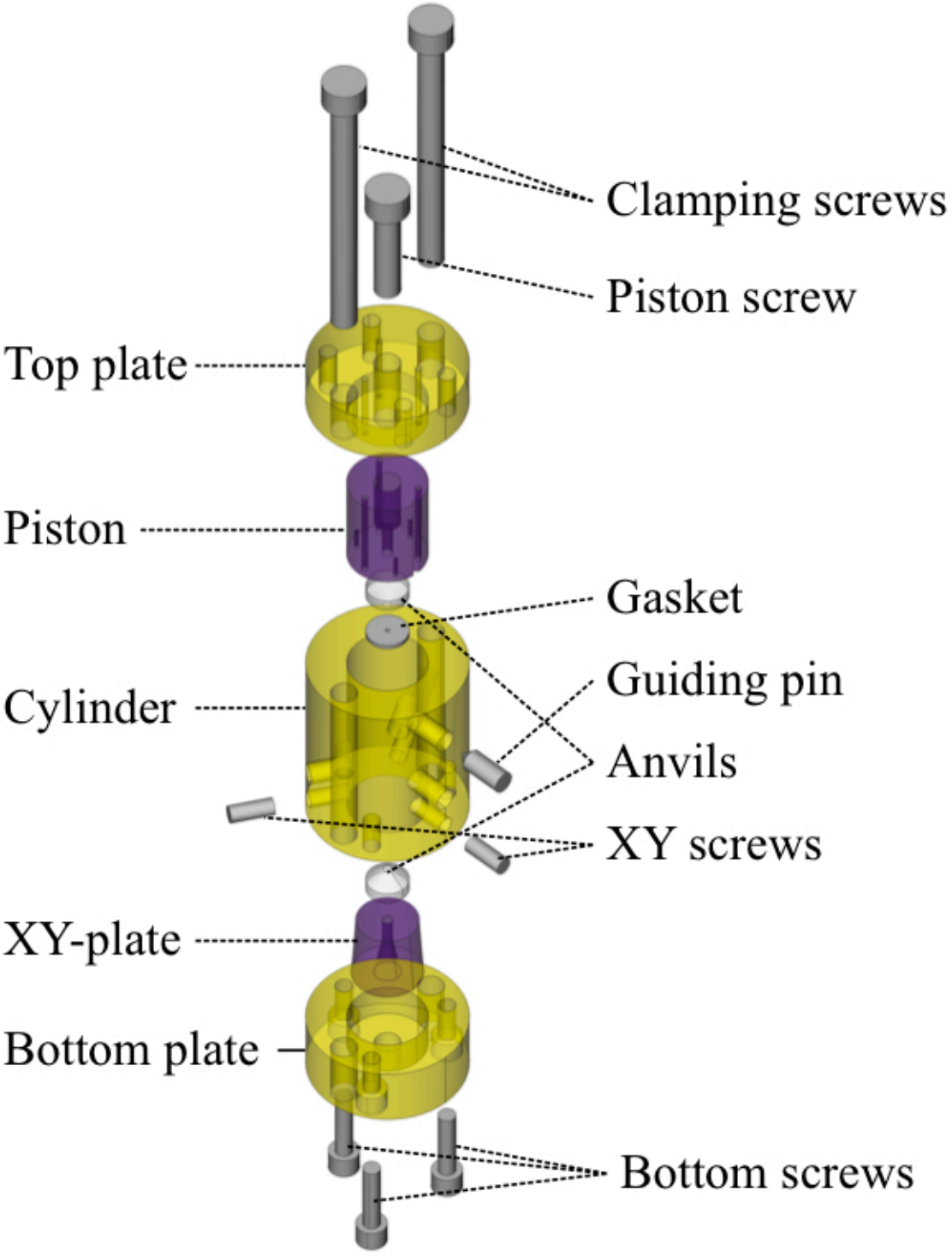

Figure 9.2: Blow-up sketch of the MAC build during the thesis. See text for details.

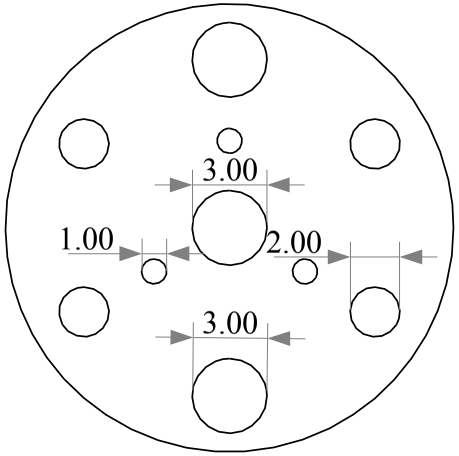

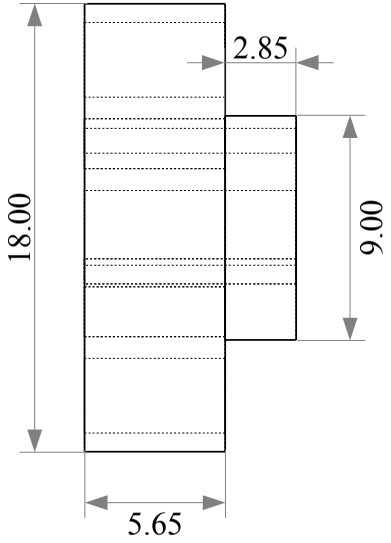

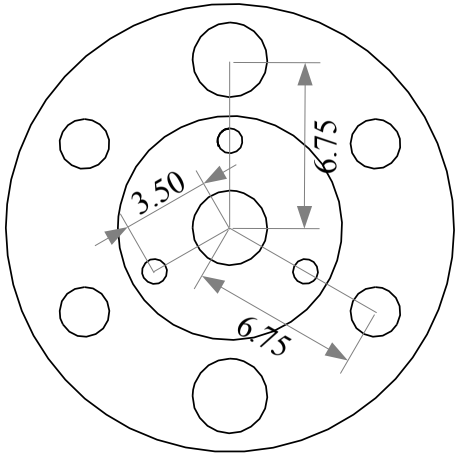

DESIGNED BY: TM		Top plate	
DATE:			
CHECKED BY:			
DATE:			
SIZE			
SCALE	WEIGHT (kg)	DRAWING NUMBER	SHEET

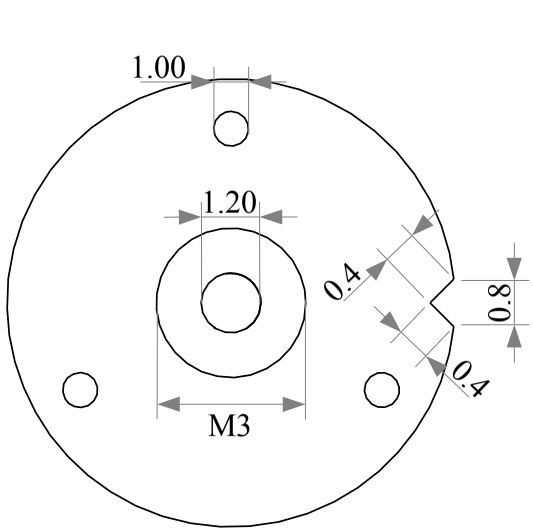

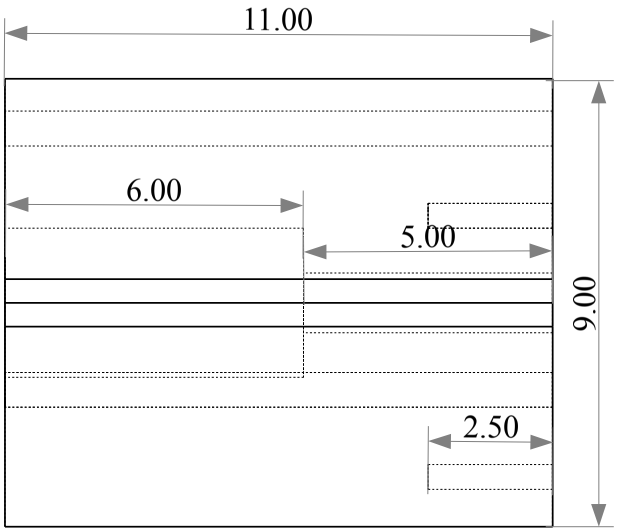

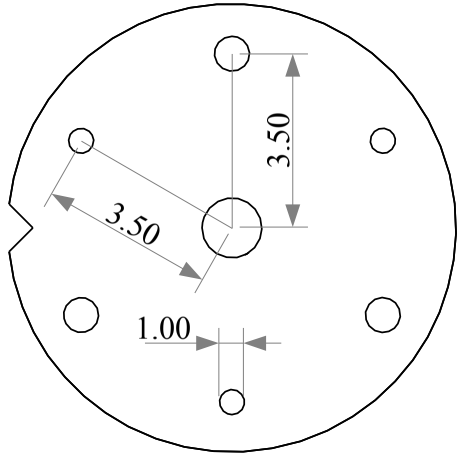

DESIGNED BY: TM		Piston	
DATE:			
CHECKED BY:			
DATE:			
SIZE			
SCALE	WEIGHT (kg)	DRAWING NUMBER	SHEET

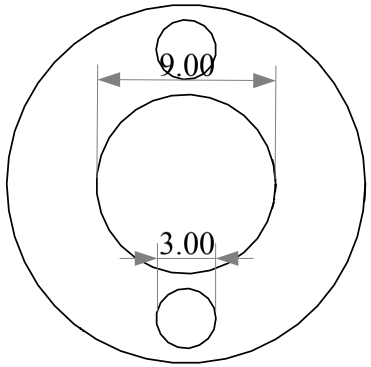

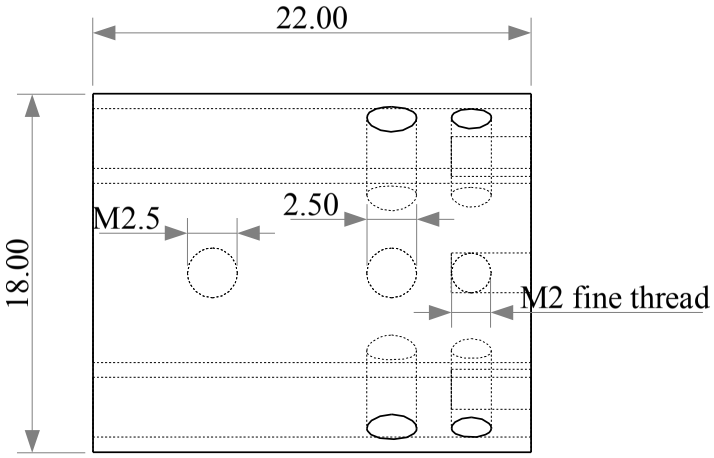

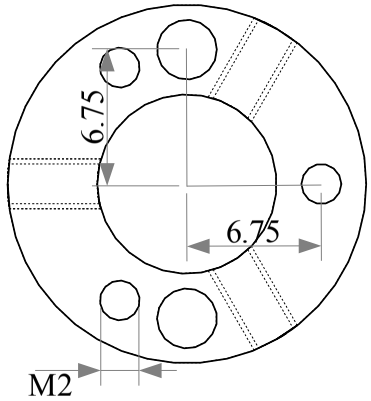

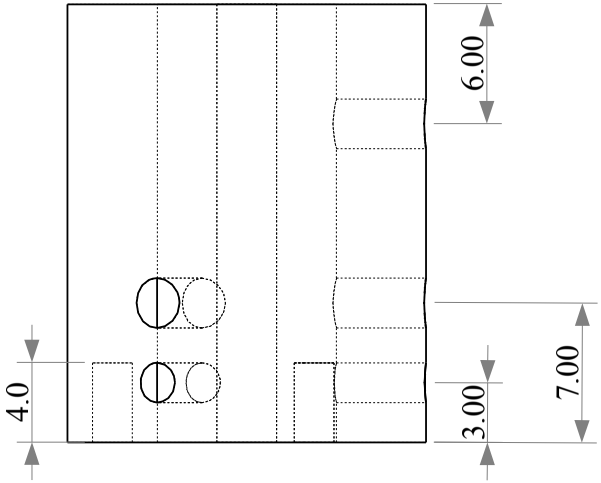

DESIGNED BY: TM	Cylinder		
DATE:			
CHECKED BY:			
DATE:			
SIZE			
SCALE	WEIGHT (kg)	DRAWING NUMBER	SHEET

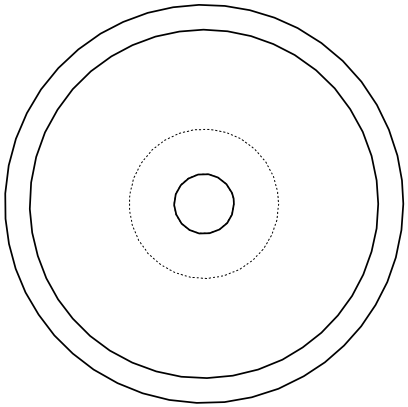

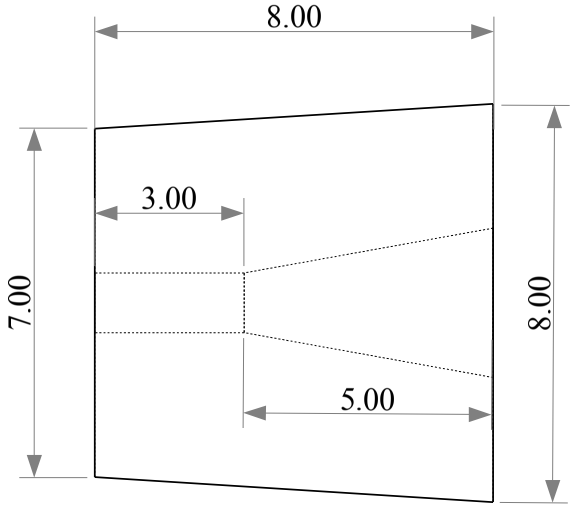

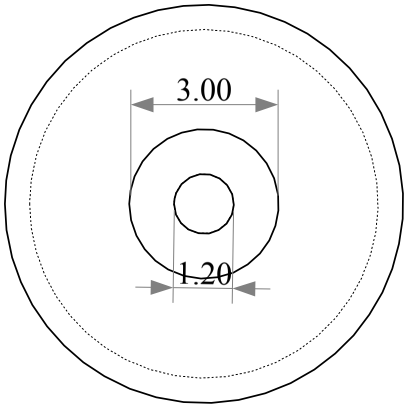

DESIGNED BY: TM DATE:		XY-plate	
CHECKED BY: DATE:			
SIZE			
SCALE	WEIGHT (kg)	DRAWING NUMBER	SHEET

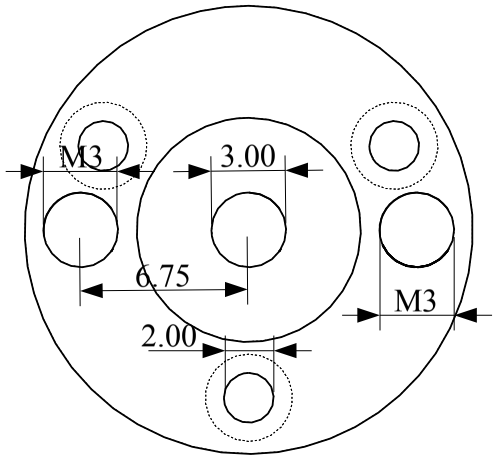

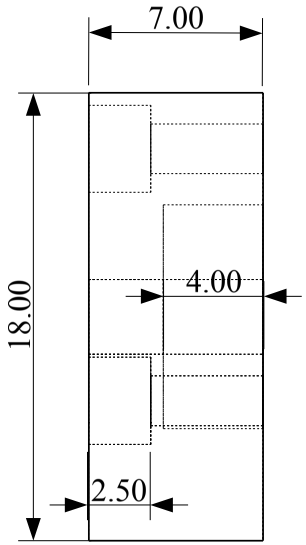

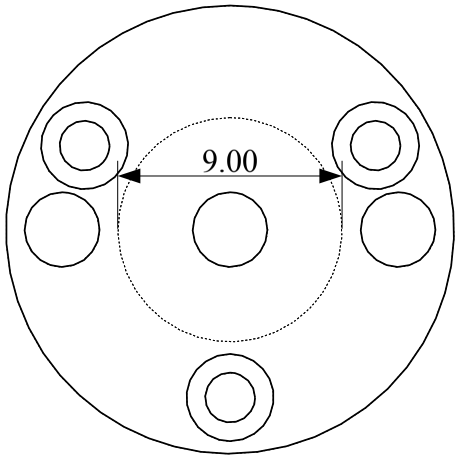

DESIGNED BY: TM	Bottom plate		I _
DATE:			H _
CHECKED BY:			G _
DATE:			F _
SIZE			E _
			D _
SCALE	WEIGHT (kg)	DRAWING NUMBER	SHEET C _
			B _
			A _

9.4 Simulation of powder spectrum

The following python 2.7 program was used to simulate the ^{17}O powder spectra in sec. 6.2.2. It uses the "mpmath" package from [143] and the "numpy" package from [144]. The program code is attached for reference.

Python code

```
import mpmath
import numpy

K1 = 0.098
K2 = 0.168
K3 = 0.170
Kmin = -0.206
Kmax = +0.370

larmorFrequency = 67.80
lbFactor = 5000

numberSteps = 2000

def lorentzian(x,x0,lb):
    return (0.5*lb/mpmath.pi)/((x-x0)**2+(0.5*lb)**2)

linebroadening = 2*100*lbFactor*1e-6/larmorFrequency
KStepsSize = (Kmax-Kmin)/numberSteps

Kcenter = Kmin+0.5*(Kmax-Kmin)

KRange = []
lineshapeFunction = []
IntegralG = []
forExport = []

K = Kmin
while K < Kmax:
    KRange += [K]
    lineshapeFunction += [lorentzian(K,Kcenter,linebroadening)]
    if K < K1:
```

```
            IntegralG += [0]
        elif K < K2:
            preFactor = mpmath.sqrt((K3-K1)*(K3-K2)/((K3-K)*(K2-K1)))
            mElement = (K-K1)*(K3-K2)/((K3-K)*(K2-K1))
            IntegralG += [preFactor*mpmath.ellipk(mElement)]
        elif K < K3:
            preFactor = mpmath.sqrt((K3-K1)/(K-K1))
            mElement = (K2-K1)*(K3-K)/((K3-K2)*(K-K1))
            IntegralG += [preFactor*mpmath.ellipk(mElement)]
        else:
            IntegralG += [0]
        K += KStepsSize

combined = numpy.convolve(lineshapeFunction,IntegralG,mode='same')
sumUp = numpy.trapz(combined)
combined = combined/sumUp

file=open("data.txt",'w')
for i in range(0,len(KRange)):
    file.write(str(larmorFrequency*(1.0+0.01*KRange[i])) + "␣" + str(
        combined[i]) + "\n")
```

10 Bibliography

[1] N. W. Ashcroft, "Condensed-matter physics: Pressure for change in metals," *Nature*, vol. 458, pp. 158–159, 2009.

[2] C. P. Slichter, *Principles of magnetic resonance*. Springer, 1990.

[3] S. H. Lee, M. S. Conradi, and R. E. Norberg, "Molecular motion in solid h_2 at high pressures," *Physical Review B*, vol. 40, pp. 12492–12498, 1989.

[4] S. H. Lee, M. S. Conradi, and R. E. Norberg, "Improved NMR resonator for diamond anvil cells," *Review of Scientific Instruments*, vol. 63, pp. 3674–3676, 1992.

[5] R. Bertani, M. Mali, J. Roos, and D. Brinkmann, "A diamond anvil cell for high-pressure NMR investigations," *Review of Scientific Instruments*, vol. 63, pp. 3303–3306, 1992.

[6] M. G. Pravica and I. F. Silvera, "Nuclear magnetic resonance in a diamond anvil cell at very high pressures," *Review of Scientific Instruments*, vol. 69, pp. 479–484, 1998.

[7] T. Okuchi, R. J. Hemley, and H. K. Mao, "Radio frequency probe with improved sensitivity for diamond anvil cell nuclear magnetic resonance," *Review of Scientific Instruments*, vol. 76, pp. 026111–026111–4, 2005.

[8] T. Meissner, "Ein neuartiger ansatz zur beobachtung von kernmagnetresonanz unter hohem druck," Master's thesis, University of Leipzig, 2009.

[9] H. Alloul, T. Ohno, and P. Mendels, "^{89}Y NMR evidence for a fermi-liquid behavior in $YBa_2Cu_3O_{6+x}$," *Physical Review Letters*, vol. 63, p. 1700, 1989.

[10] W. W. Warren, R. E. Walstedt, G. F. Brennert, R. J. Cava, R. Tycko, R. F. Bell, and G. Dabbagh, "Cu spin dynamics and superconducting precursor effects in planes above t_c in $YBa_2Cu_3O_{6.7}$," *Physical Review Letters*, vol. 62, p. 1193, 1989.

[11] J. S. Schilling, "High-pressure effects," in *Handbook of High-Temperature Superconductivity: Theory and Experiment* (J. R. Schrieffer, ed.), Springer, 1 ed., 2007.

[12] H. Zimmermann, M. Mali, I. Mangelschots, J. Roos, D. Brinkmann, J. Karpinski, S. Rusiecki, and E. Kaldis, "Cu nuclear quadrupole resonance study of $YBa_2Cu_4O_8$ at high pressure," *Journal of the Less Common Metals*, vol. 164-165, pp. 132–137, 1990.

[13] G.-Q. Zheng, T. Mito, Y. Kitaoka, K. Asayama, and Y. Kodama, "^{63}Cu NMR and NQR studies of high-t_c cuprates under pressure," *Physica C: Superconductivity*, vol. 243, pp. 337–341, 1995.

[14] T. Machi and N. Koshizuka, "NQR study of $YBa_2Cu_4O_8$ under high pressure," *Review of High Pressure Science and Technology*, vol. 13, pp. 335–340, 2003.

[15] A. Abragam, *The principles of nuclear magnetism.* Oxford University Press, 1983.

[16] B. V. Fine, "Long-time behavior of spin echo," *Physical Review Letters*, vol. 94, p. 247601, 2005.

[17] J. H. van Vleck, "The dipolar broadening of magnetic resonance lines in crystals," *Physical Review*, vol. 74, pp. 1168–1183, 1948.

[18] T. Moriya, "The effect of electron-electron interaction on the nuclear spin relaxation in metals," *Journal of the Physical Society of Japan*, vol. 18, pp. 516–520, 1963.

[19] T. L. Peck, R. L. Magin, and P. C. Lauterbur, "Design and analysis of microcoils for NMR microscopy," *Journal of Magnetic Resonance, Series B*, vol. 108, pp. 114–124, 1995.

[20] A. G. Webb, "Radiofrequency microcoils in magnetic resonance," *Progress in Nuclear Magnetic Resonance Spectroscopy*, vol. 31, pp. 1–42, 1997.

[21] H. Meinke and F. W. Grundlach, *Taschenbuch der Hochfrequenztechnik.* Springer, 1962.

[22] D. I. Hoult and R. E. Richards, "The signal-to-noise ratio of the nuclear magnetic resonance experiment," *Journal of Magnetic Resonance*, vol. 24, pp. 71–85, 1976.

[23] F. Doty, T. Connick, X. Ni, and M. Clingan, "Noise in high-power, high-frequency double-tuned probes," *Journal of Magnetic Resonance (1969)*, vol. 77, pp. 536–549, 1988.

[24] B. P. Cowan, *Nuclear magnetic resonance and relaxation.* Cambridge University Press, 1997.

[25] W. B. Holzapfel and N. S. Isaacs, *High pressure techniques in chemistry and physics.* Oxford University Press, 1997.

[26] J. A. Xu, H. K. Mao, and P. M. Bell, "High-pressure ruby and diamond fluorescence: Observations at 0.21 to 0.55 terapascal," *Science*, vol. 232, no. 4756, pp. 1404–1406, 1986.

[27] A. L. Ruoff, H. Xia, H. Luo, and Y. K. Vohra, "Miniaturization techniques for obtaining static pressures comparable to the pressure at the center of the earth: X-ray diffraction at 416 gpa," *Review of Scientific Instruments*, vol. 61, pp. 3830–3833, 19990.

[28] J. A. Xu, J. Yen, Y. Wang, and E. Huang, "Ultrahigh pressures in gem anvil cells," *High Pressure Research*, vol. 15, pp. 127–134, 1996.

[29] J. A. Xu, H. K. Mao, R. J. Hemley, and E. Hines, "The moissanite anvil cell: a new tool for high-pressure research," *Journal of Physics: Condensed Matter*, vol. 14, pp. 11543–11548, 2002.

[30] A. Jayaraman, "Diamond anvil cell and high-pressure physical investigations," *Reviews of Modern Physics*, vol. 55, pp. 65–108, 1983.

[31] A. Jayaraman, "Ultrahigh pressures," *Review of Scientific Instruments*, vol. 57, pp. 1013–1031, 1986.

[32] D. J. Dunstan and I. L. Spain, "Technology of diamond anvil high-pressure cells: I. principles, design and construction," *Journal of Physics E: Scientific Instruments*, vol. 22, pp. 913–923, 1989.

[33] I. L. Spain and D. J. Dunstan, "The technology of diamond anvil high-pressure cells: II. operation and use," *Journal of Physics E: Scientific Instruments*, vol. 22, pp. 933–936, 1989.

[34] S. H. Lee, K. Luszczynski, R. E. Norberg, and M. S. Conradi, "NMR in a diamond anvil cell," *Review of Scientific Instruments*, vol. 58, pp. 415–417, 1987.

[35] K. E. Halvorson, D. P. Raffaelle, G. H. Wolf, and R. F. Marzke, "Proton NMR chemical shifts in organic liquids measured at high pressure using the diamond anvil cell," in *Frontiers of High Pressure Research* (H. D. Hocheheimer and R. D. Etters, eds.), pp. 217–226, Plenum Press, 1992.

[36] R. F. Marzke, D. P. Raffaelle, K. E. Halvorson, and G. H. Wolf, "A ^{1}H NMR study of glycerol at high pressure," *Journal of Non-Crystalline Solids*, vol. 172-174, pp. 401–407, 1994.

[37] J. L. Yarger, R. A. Nieman, G. H. Wolf, and R. F. Marzke, "High-Pressure ^{1}H and ^{13}C nuclear magnetic resonance in a diamond anvil cell," *Journal of Magnetic Resonance, Series A*, vol. 114, pp. 255–257, 1995.

[38] H. N. Bachman and I. F. Silvera, "Impurity proton NMR signals from common proton-free laboratory materials," *Journal of Magnetic Resonance*, vol. 162, pp. 417–422, 2003.

[39] M. G. Pravica and I. F. Silvera, "NMR study of ortho-para conversion at high pressure in hydrogen," *Physical Review Letters*, vol. 81, pp. 4180–4183, 1998.

[40] R. Bertani, M. Mali, J. Roos, and D. Brinkmann, "The Knight shift and diffusion in solid lithium and sodium at pressures up to 8 GPa studied by NMR," *Journal of Physics: Condensed Matter*, vol. 2, pp. 7911–7923, 1990.

[41] S. Kluthe, R. Markendorf, M. Mali, J. Roos, and D. Brinkmann, "Pressure-dependent Knight shift in na and cs metal," *Physical Review B*, vol. 53, pp. 11369–11375, 1996.

[42] T. Okuchi, "Collision and diffusion dynamics of dense molecular hydrogen by diamond anvil cell nuclear magnetic resonance," *Journal of Physical Chemistry C*, 2011.

[43] T. Okuchi, G. D. Cody, H. K. Mao, and R. J. Hemley, "Hydrogen bonding and dynamics of methanol by high-pressure diamond-anvil cell NMR," *The Journal of Chemical Physics*, vol. 122, pp. 244509–244509–5, 2005.

[44] T. Okuchi, M. Takigawa, J. Shu, H. K. Mao, R. J. Hemley, and T. Yagi, "High pressure nmr of hydrogen-filled ices by diamond anvil cell," in *Physics and Chemistry of Ice* (W. F. Kuhs, ed.), pp. 469–473, Royal Society of Chemistry, 2007.

[45] T. Okuchi, M. Takigawa, J. Shu, H. K. Mao, R. J. Hemley, and T. Yagi, "Fast molecular transport in hydrogen hydrates by high-pressure diamond anvil cell NMR," *Physical Review B*, vol. 75, p. 144104, 2007.

[46] T. Okuchi, H. K. Mao, and R. J. Hemley, "A new gasket material for higher resolution NMR in diamond anvil cells," in *Advances in High-Pressure Technology for Geophysical Applications* (J. Chen, Y. Wang, T. S. Duffy, G. Shen, and L. F. Dobrzhinetskaya, eds.), ch. 26, pp. 503–509, Elsevier, 2005.

[47] T. Nakanishi, N. Takeshita, and N. Mori, "A newly developed high-pressure cell by using modified bridgman anvils for precise measurements in magnetic fields at low temperatures," *Review of Scientific Instruments*, vol. 73, pp. 1828–1831, 2002.

[48] T. Suzuki, I. Yamauchi, Y. Shimizu, M. Itoh, N. Takeshita, C. Terakura, H. Takagi, Y. Tokura, T. Yamauchi, and Y. Ueda, "High-pressure ^{51}V NMR study of the magnetic phase diagram and metal-insulator transition in quasi-one-dimensional β-$Na_{0.33}V_2O_5$," *Physical Review B*, vol. 79, p. 081101, 2009.

[49] K. Kitagawa, H. Gotou, T. Yagi, A. Yamada, T. Matsumoto, Y. Uwatoko, and M. Takigawa, "Space efficient opposed-anvil high-pressure cell and its application to optical and NMR measurements up to 9 GPa," *Journal of the Physical Society of Japan*, vol. 79, pp. 024001–024008, 2010.

[50] R. Kobayashi, Y. Uchida, K. Hirayama, T. Yamazaki, H. Fukazawa, Y. Kohori, and N. Takeshita, "Development of nuclear magnetic and quadrupole resonance spectroscopy under 10 GPa class pressure," *Journal of Physics: Conference Series*, vol. 215, pp. 012183–4, 2010.

[51] J. Haase, S. K. Goh, T. Meissner, P. L. Alireza, and D. Rybicki, "High sensitivity nuclear magnetic resonance probe for anvil cell pressure experiments," *Review of Scientific Instruments*, vol. 80, pp. 073905–073908, 2009.

[52] T. Meissner, S. Goh, J. Haase, B. Meier, D. Rybicki, and P. Alireza, "New approach to high-pressure nuclear magnetic resonance with anvil cells," *Journal of Low Temperature Physics*, vol. 159, pp. 284–287, 2010.

[53] T. Meier, "Giga-pascal NMR in solids," Master's thesis, University of Leipzig, Germany, 2012.

[54] J. D. Barnett, S. Block, and G. J. Piermarini, "An optical fluorescence system for quantitative pressure measurement in the diamond-anvil cell," *Review of Scientific Instruments*, vol. 44, pp. 1–9, 1973.

[55] T. Osakabe and K. Kakurai, "Feasibility tests on pressure-transmitting media for single-crystal magnetic neutron diffraction under high pressure," *Japanese Journal of Applied Physics*, vol. 47, pp. 6544–6547, 2008.

[56] "IZA structure commission." http://www.iza-structure.org/.

[57] J. Haase and E. Oldfield, "Quantitative determination of nonintegral spin quadrupolar nuclei in solids using nuclear magnetic resonance spin-echo techniques," *Journal of Magnetic Resonance, Series A*, vol. 104, pp. 1–9, 1993.

[58] T. Meissner, S. K. Goh, J. Haase, M. Richter, K. Koepernik, and H. Eschrig, "Nuclear magnetic resonance at up to 10.1 giga-pascal pressure detects an electronic topological transition in aluminum metal," *arXiv:1207.3702*, 2012.

[59] K. Kitagawa, N. Katayama, H. Gotou, T. Yagi, K. Ohgushi, T. Matsumoto, Y. Uwatoko, and M. Takigawa, "Spontaneous formation of a superconducting and antiferromagnetic hybrid state in $SrFe_2As_2$ under high pressure," *Physical Review Letters*, vol. 103, pp. 257002–257005, 2009.

[60] J. Kohlrautz, "Zeitentwicklung stark korrelierter Kernspinzustände," Master's thesis, University of Leipzig, 2011.

[61] N. W. Ashcroft and N. D. Mermin, *Solid State Physics*. Cengage Learning Emea, 1976.

[62] A. Varlamov, V. Egorov, and A. Pantsulaya, "Kinetic properties of metals near electronic topological transitions (2 1/2-order transitions)," *Advances in Physics*, vol. 38, pp. 469–564, 1989.

[63] N. Kozlova, J. Hagel, M. Doerr, J. Wosnitza, D. Eckert, K.-H. Müller, L. Schultz, I. Opahle, S. Elgazzar, M. Richter, G. Goll, H. v. Löhneysen, G. Zwicknagl, T. Yoshino, and T. Takabatake, "Magnetic-field-induced band-structure change in CeBiPt," *Physical Review Letters*, vol. 95, p. 086403, 2005.

[64] I. M. Lifshitz, "Anomalies of electron characteristics of a metal in the high pressure region," *Soviet Physics-JETP*, vol. 11, pp. 113–1135, 1960.

[65] H. Eschrig, *The Fundamentals of Densitiy Functional Theory.* Teubner Verlag, 1996.

[66] Y. Akahama, M. Nishimura, K. Kinoshita, H. Kawamura, and Y. Ohishi, "Evidence of a fcc-hcp transition in aluminum at multimegabar pressure," *Physical Review Letters*, vol. 96, pp. 045505–4, 2006.

[67] K. Syassen and W. B. Holzapfel, "Isothermal compression of Al and Ag to 120 kbar," *Journal of Applied Physics*, vol. 49, pp. 4427–4430, 1978.

[68] W. A. Harrison, "Fermi surface in aluminum," *Physical Review*, vol. 116, pp. 555–561, 1959.

[69] P. J. Melz, "Effect of high pressure on the fermi surface of aluminum," *Physical Review*, vol. 152, pp. 540–547, 1966.

[70] J. J. Burton and G. Jura, "Fermi momentum of aluminum from 0 to 100 kbar," *Physical Review*, vol. 171, pp. 699–701, 1968.

[71] D. R. Overcash, T. Davis, J. W. Cook, and M. J. Skove, "Stress-induced electronic transition (2.5 order) in al," *Physical Review Letters*, vol. 46, pp. 287–290, 1981.

[72] T. Kushida and J. C. Murphy, "Pressure dependence of the Knight shift in al and nb metal," *Physical Review B*, vol. 3, pp. 1574–1588, 1971.

[73] W. D. Knight, "Nuclear magnetic resonance shift in metals," *Physical Review*, vol. 76, pp. 1259–1260, 1949.

[74] W.-M. Shyu, T. P. Das, and G. D. Gaspari, "Direct and core-polarization contributions to the knight shift in metallic aluminum," *Physical Review*, vol. 152, pp. 270–278, 1966.

[75] J. Korringa, "Nuclear magnetic relaxation and resonnance line shift in metals," *Physica*, vol. 16, pp. 601–610, 1950.

[76] D. Pines, "Paramagnetic susceptibility of conduction electrons," *Physical Review*, vol. 95, pp. 1090–1091, 1954.

[77] J. J. Spokas and C. P. Slichter, "Nuclear relaxation in aluminum," *Physical Review*, vol. 113, pp. 1462–1472, 1959.

[78] E. Andrew, W. Hinshaw, and R. Tiffen, "More precise determination of the knight shift of aluminium," *Physics Letters A*, vol. 46, pp. 57–58, 1973.

[79] I. J. Lowe and R. E. Norberg, "Free-induction decays in solids," *Physical Review*, vol. 107, pp. 46–61, 1957.

[80] S. W. Morgan, B. V. Fine, and B. Saam, "Universal long-time behavior of nuclear spin decays in a solid," *Physical Review Letters*, vol. 101, pp. 067601–4, 2008.

[81] P. Borckmans and D. Walgraef, "Long-time behavior of the free-induction decay in paramagnetic spin systems," *Physical Review Letters*, vol. 21, pp. 1516–1517, 1968.

[82] B. Meier, J. Kohlrautz, and J. Haase, "Eigenmodes in the long-time behavior of a coupled spin system measured with nuclear magnetic resonance," *Physical Review Letters*, vol. 108, p. 177602, 2012.

[83] J. Haase and E. Oldfield, "Spin-echo behavior of nonintegral-spin quadrupolar nuclei in inorganic solids," *Journal of Magnetic Resonance, Series A*, vol. 101, pp. 30–40, 1993.

[84] N. Bloembergen and T. Rowland, "On the nuclear magnetic resonance in metals and alloys," *Acta Metallurgica*, vol. 1, pp. 731–746, 1953.

[85] A. Overhauser, "Charge-density waves and isotropic metals," *Advances in Physics*, vol. 27, pp. 343–363, 1978.

[86] F. Birch, "Finite elastic strain of cubic crystals," *Physical Review*, vol. 71, p. 809, 1947.

[87] K. Koepernik and H. Eschrig, "Full-potential nonorthogonal local-orbital minimum-basis band-structure scheme," *Physical Review B*, vol. 59, pp. 1743–1757, 1999.

[88] J. P. Perdew and Y. Wang, "Accurate and simple analytic representation of the electron-gas correlation energy," *Physical Review B*, vol. 45, pp. 13244–13249, 1992.

[89] P. E. Blöchl, O. Jepsen, and O. K. Andersen, "Improved tetrahedron method for Brillouin-zone integrations," *Physical Review B*, vol. 49, pp. 16223–16233, 1994.

[90] W. Joss and R. Monnier, "Fermi surface of aluminium under homogeneous strain," *Journal of Physics F: Metal Physics*, vol. 10, pp. 9–31, 1980.

[91] H. Bross, "LDA and GGA investigations of some ground state properties of aluminium with the all electron MAPW method," *The European Physical Journal B*, vol. 37, pp. 405–411, 2003.

[92] J. G. Bednorz and K. A. Müller, "Possible high t_c superconductivity in the Ba-La-Cu-O system," *Zeitschrift für Physik B: Condensed Matter*, vol. 64, pp. 189–193, 1986.

[93] L. Gao, Y. Y. Xue, F. Chen, Q. Xiong, R. L. Meng, D. Ramirez, C. W. Chu, J. H. Eggert, and H. K. Mao, "Superconductivity up to 164 K in $HgBa_2Ca_{m-1}Cu_mO_{2m+2+delta}$ (m =1, 2, and 3) under quasihydrostatic pressures," *Physical Review B*, vol. 50, p. 4260, 1994.

[94] Y. Kamihara, H. Hiramatsu, M. Hirano, R. Kawamura, H. Yanagi, T. Kamiya, and H. Hosono, "Iron-based layered superconductor: LaOFeP," *Journal of the American Chemical Society*, vol. 128, pp. 10012–10013, 2006.

[95] O. Fischer, M. Kugler, I. Maggio-Aprile, C. Berthod, and C. Renner, "Scanning tunneling spectroscopy of high-temperature superconductors," *Reviews of Modern Physics*, vol. 79, pp. 353–419, 2007.

[96] P. A. Lee, N. Nagaosa, and X.-G. Wen, "Doping a Mott insulator: Physics of high-temperature superconductivity," *Reviews of Modern Physics*, vol. 78, pp. 17–85, 2006.

[97] R. E. Walstedt, *The NMR Probe of High-T_c Materials*. Springer, 1 ed., 2007.

[98] C. P. Slichter, "Magnetic resonance studies of high temperature superconductors," in *Handbook of High-Temperature Superconductivity: Theory and Experiment* (J. R. Schrieffer, ed.), Springer, 1 ed., 2007.

[99] J. Haase, O. P. Sushkov, P. Horsch, and G. V. M. Williams, "Planar Cu and O hole densities in high-T_c cuprates determined with NMR," *Physical Review B*, vol. 69, p. 094504, 2004.

[100] N. J. Curro, B.-L. Young, J. Schmalian, and D. Pines, "Scaling in the emergent behavior of heavy-electron materials," *Physical Review B*, vol. 70, p. 235117, 2004.

[101] M. K. Wu, J. R. Ashburn, C. J. Torng, P. H. Hor, R. L. Meng, L. Gao, Z. J. Huang, Y. Q. Wang, and C. W. Chu, "Superconductivity at 93 k in a new mixed-phase y-ba-cu-o compound system at ambient pressure," *Physical Review Letters*, vol. 58, pp. 908–910, 1987.

[102] M. Takigawa, A. P. Reyes, P. C. Hammel, J. D. Thompson, R. H. Heffner, Z. Fisk, and K. C. Ott, "Cu and O NMR studies of the magnetic properties of $YBa_2Cu_3O_{6.63}$ ($T_c = 62$ K)," *Physical Review B*, vol. 43, p. 247, 1991.

[103] F. C. Zhang and T. M. Rice, "Effective hamiltonian for the superconducting cu oxides," *Physical Review B*, vol. 37, p. 3759, 1988.

[104] V. Barzykin and D. Pines, "Phenomenological model of protected behavior in the pseudogap state of underdoped cuprate superconductors," *Physical Review Letters*, vol. 96, p. 247002, 2006.

[105] I. Mangelschots, M. Mali, J. Roos, D. Brinkmann, S. Rusiecki, J. Karpinski, and E. Kaldis, "^{17}O NMR study in aligned $YBa_2Cu_4O_8$ powder," *Physica C: Superconductivity*, vol. 194, pp. 277–286, 1992.

[106] M. Bankay, M. Mali, J. Roos, and D. Brinkmann, "Single-spin fluid, spin gap, and d-wave pairing in $YBa_2Cu_4O_8$: A NMR and NQR study," *Physical Review B*, vol. 50, p. 6416, 1994.

[107] T. Machi, N. Koshizuka, and H. Yasuoka, "^{17}O NMR study on $YBa_2Cu_4O_8$," *Physica B: Condensed Matter*, vol. 284-288, pp. 943–944, 2000.

[108] J. Haase, C. P. Slichter, and G. V. M. Williams, "Evidence for two electronic components in high-temperature superconductivity from NMR," *Journal of Physics: Condensed Matter*, vol. 21, p. 455702, 2009.

[109] D. C. Johnston, "Magnetic susceptibility scaling in $la2-xsr_xcuo_{4-y}$," *Physical Review Letters*, vol. 62, p. 957, 1989.

[110] T. Nakano, M. Oda, C. Manabe, N. Momono, Y. Miura, and M. Ido, "Magnetic properties and electronic conduction of superconducting $la_{2-x}sr_xCuO_4$," *Physical Review B*, vol. 49, pp. 16000–16008, 1994.

[111] J. Haase, D. Rybicki, C. P. Slichter, M. Greven, G. Yu, Y. Li, and X. Zhao, "Two-component uniform spin susceptibility of superconducting $HgBa_2CuO_{4+\delta}$ single crystals measured using ^{63}Cu and ^{199}Hg nuclear magnetic resonance," *Physical Review B*, vol. 85, p. 104517, 2012.

[112] D. Rybicki, J. Haase, M. Lux, M. Jurkutat, M. Greven, G. Yu, Y. Li, and X. Zhao, "^{63}Cu and ^{199}Hg NMR study of $HgBa_2CuO_{4+\delta}$ single crystals," *arXiv:1208.4690*, 2012.

[113] R. E. Walstedt, B. S. Shastry, and S.-W. Cheong, "NMR, neutron scattering, and the one-band model of $la_{2-x}sr_xCuO_4$," *Physical Review Letters*, vol. 72, p. 3610, 1994.

[114] J. Karpinski, E. Kaldis, E. Jilek, S. Rusiecki, and B. Bucher, "Bulk synthesis of the 81 K superconductor $YBa_2Cu_4O_8$ at high oxygen pressure," *Nature*, vol. 336, pp. 660–662, 1988.

[115] J. Karpinski, E. Kaldis, S. Rusiecki, E. Jilek, P. Fischer, P. Bordet, C. Chaillout, J. Chenavas, J. Hodeau, and M. Marezio, "Two new bulk superconducting phases in the y-ba-cu-o system: $YBa_2Cu_{3.5}O_{7+x}$ ($t_c \approx 40$ k) and $YBa_2Cu_4O_{8+x}$ ($t_c \approx 80$ k)," *Journal of the Less Common Metals*, vol. 150, pp. 129–137, 1989.

[116] T. Meissner, S. K. Goh, J. Haase, G. V. M. Williams, and P. B. Littlewood, "High-pressure spin shifts in the pseudogap regime of superconducting $YBa_2Cu_4O_8$ as revealed by ^{17}O NMR," *Physical Review B: Rapid Communications*, vol. 83, p. 220517, 2011.

[117] D. Rybicki, M. Greven, J. Haase, T. Meissner, S. K. Goh, and G. V. M. Williams, "Two-component behavior of cuprate superconductors from NMR shifts," *Materials Science Forum*, vol. 700, pp. 1–6, 2011.

[118] G. V. M. Williams, J. L. Tallon, and R. Dupree, "NMR study of magnetic and nonmagnetic impurities in $YBa_2Cu_4O_8$," *Physical Review B*, vol. 61, p. 4319, 2000.

[119] E. V. Eenige, R. Griessen, R. Wijngaarden, J. Karpinski, E. Kaldis, S. Rusiecki, and E. Jilek, "Superconductivity at 108 K in $YBa_2Cu_4O_8$ at pressures up to 12 GPa," *Physica C: Superconductivity*, vol. 168, pp. 482–488, 1990.

[120] D. Braithwaite, G. Chouteau, G. Martinez, J. Hodeau, M. Marezio, J. Karpinski, E. Kaldis, S. Rusiecki, and E. Jilek, "The superconducting properties of $YBa_2Cu_4O_8$ single crystals under hydrostatic pressure (up to 9.5 GPa)," *Physica C: Superconductivity*, vol. 178, pp. 75–80, 1991.

[121] Y. Song, J. Peng, X. Wang, G. Sun, and C. Lin, "Ambient-condition growth of superconducting $YBa_2Cu_4O_8$ single crystals using KOH flux," *Journal of Crystal Growth*, vol. 300, pp. 263–266, 2007.

[122] M. Calamiotou, A. Gantis, E. Siranidi, D. Lampakis, J. Karpinski, and E. Liarokapis, "Pressure-induced lattice instabilities and superconductivity in $YBa_2Cu_4O_8$ and optimally doped $YBa_2Cu_3O_{7-\delta}$," *Physical Review B*, vol. 80, pp. 214517–7, 2009.

[123] G.-Q. Zheng, Y. Kitaoka, K. Asayama, Y. Kodama, and Y. Yamada, "^{17}O NMR study of local hole density and spin dynamics in $YBa_2Cu_4O_8$," *Physica C: Superconductivity*, vol. 193, pp. 154–162, 1992.

[124] N. J. Curro, T. Imai, C. P. Slichter, and B. Dabrowski, "High-temperature ^{63}Cu(2) nuclear quadrupole and magnetic resonance measurements of $YBa_2Cu_4O_8$," *Physical Review B*, vol. 56, pp. 877–885, 1997.

[125] M. Takigawa, P. C. Hammel, R. H. Heffner, and Z. Fisk, "Spin susceptibility in superconducting $YBa_2Cu_3O_7$ from ^{63}Cu Knight shift," *Physical Review B: Rapid Communications*, vol. 39, pp. 7371–7374, 1989.

[126] M. Takigawa, P. C. Hammel, R. H. Heffner, Z. Fisk, K. C. Ott, and J. D. Thompson, "^{17}O NMR study of local spin susceptibility in aligned $YBa_2Cu_3O_7$ powder," *Physical Review Letters*, vol. 63, p. 1865, 1989.

[127] M. S. Grbic, M. Pozek, D. Paar, V. Hinkov, M. Raichle, D. Haug, B. Keimer, N. Barisic, and A. Dulcic, "Temperature range of superconducting fluctuations above T_c in $YBa_2Cu_3O_{7-\delta}$ single crystals," *Physical Review B*, vol. 83, p. 144508, 2011.

[128] A. Suter, M. Mali, J. Roos, and D. Brinkmann, "Charge degree of freedom and the single-spin fluid model in $YBa_2Cu_4O_8$," *Physical Review Letters*, vol. 84, p. 4938, 2000.

[129] S. K. Goh. Private communication, 2012.

[130] S. Sambale, "Einkristall-NMR am Hochtemperatursupraleiter $YBa_2Cu_4O_8$," Master's thesis, University of Leipzig, 2010.

[131] C. Scheidler, "NMR-Untersuchungen am Hochtemperatur-Supraleiter $YBa_2Cu_4O_8$," Bachelor's thesis, University of Leipzig, 2011.

[132] O. Lutz, H. Oehler, and P. Kroneck, "^{63}Cu and ^{65}Cu Fourier transform nuclear magnetic resonance studies," *Zeitschrift für Physik A: Hadrons and Nuclei*, vol. 288, pp. 17–21, 1978.

[133] P. M. Singer, A. W. Hunt, and T. Imai, "^{63}Cu NQR evidence for spatial variation of hole concentration in $La_{2-x}Sr_xCuO_4$," *Physical Review Letters*, vol. 88, p. 047602, 2002.

[134] J. J. Scholtz, E. N. van Eenige, R. J. Wijngaarden, and R. Griessen, "Pressure dependence of T_c and h_{c2} of $YBa_2Cu_4O_8$," *Physical Review B*, vol. 45, p. 3077, 1992.

[135] M. Mali, J. Roos, and D. Brinkmann, "NMR and NQR study of Ca-substituted superconducting $YBa_2Cu_4O_8$," *Physical Review B*, vol. 53, p. 3550, 1996.

[136] P. Benzi, E. Bottizzo, and N. Rizzi, "Oxygen determination from cell dimensions in YBCO superconductors," *Journal of Crystal Growth*, vol. 269, pp. 625–629, 2004.

[137] J. S. Zhou and J. B. Goodenough, "Pressure dependence of thermopower in $YBa_2Cu_3O_{6.96}$ and $YBa_2Cu_4O_8$," *Physical Review B: Rapid Communications*, vol. 53, p. 11976, 1996.

[138] J. S. Zhou, J. B. Goodenough, B. Dabrowski, and K. Rogacki, "Transport properties of a $YBa_2Cu_4O_8$ crystal under high pressure," *Physical Review Letters*, vol. 77, p. 4253, 1996.

[139] H. Zimmermann, M. Mali, D. Brinkmann, J. Karpinski, E. Kaldis, and S. Rusiecki, "Copper NQR and NMR in the superconductor $YBa_2Cu_4O_{8+x}$," *Physica C: Superconductivity*, vol. 159, pp. 681–688, 1989.

[140] J. Tallon and J. Lusk, "High-pressure studies on the 90 K superconductors $Y2Ba_4Cu_7O_{15}$ and $(Y/Ca)Ba_2Cu_4O_8$," *Physica C: Superconductivity*, vol. 167, pp. 236–242, 1990.

[141] T. Machi, I. Tomeno, T. Miyatake, N. Koshizuka, S. Tanaka, T. Imai, and H. Yasuoka, "Nuclear spin-lattice relaxation and knight shift in YBa2Cu4O8," *Physica C: Superconductivity*, vol. 173, pp. 32–36, 1991.

[142] J. Bobroff, H. Alloul, P. Mendels, V. Viallet, J.-F. Marucco, and D. Colson, "^{17}O NMR evidence for a pseudogap in the monolayer $HgBa_2CuO_{4+\delta}$," *Physical Review Letters*, vol. 78, p. 3757, 1997.

[143] F. Johansson *et al.*, *mpmath: a Python library for arbitrary-precision floating-point arithmetic (version 0.14)*, February 2010. `http://code.google.com/p/mpmath/`.

[144] E. Jones, T. Oliphant, P. Peterson, *et al.*, *SciPy: Open source scientific tools for Python*, 2001–. `http://www.scipy.org/`.

Acknowledgement

First of all I would like to express my gratitude towards Prof. Jürgen Haase for letting me work on this interesting topic and fully supporting me throughout the thesis.

I would furthermore like to express my gratitude towards Dr. Swee K. Goh for supplying and preparing the numerous pressure cells used during this thesis. Without his help, this work would not have been possible.

The late Dr. Helmut Eschrig, Dr. Klaus Koepernik and especially Dr. Manuel Richter are gratefully acknowledged for carrying out the band structure calculations on aluminum. Those are invaluable for understanding the data. I am obliged to Dr. Grant Williams and Dr. Chengtian Lin for supplying the $YBa_2Cu_4O_8$ samples. Special thanks also go to Jonas, Damian, Benno and Micha for helping me out through all those night measurements. I greatly enjoyed the working atmosphere in the MQF group. Johann, thanks for solving that angular problem of mine.

Thank you Anne for your patience with me and proof-reading my work all these countless times. Niklas and Kilian, you two have been very understanding when I had "keine Nerven mehr".

Furthermore, financial support by the DFG (International Research Training Group Diffusion in Porous Materials) and the Royal Society is gratefully acknowledged.

Bibliographische Beschreibung

Meißner, Thomas
Exploring Nuclear Magnetic Resonance at the Highest Pressures
Universität Leipzig, Dissertation
131 Seiten, 144 Zitate, 63 Abbildungen, 7 Tabellen

Referat: Die vorliegende Arbeit beschäftigt sich mit der Entwicklung und Anwendung der Kernmagnetresonanz (NMR) unter extremen Drücken bis 101 kbar. Im ersten Teil der Arbeit wird gezeigt, dass die Empfindlichkeit von NMR Experimenten unter hohen Drücken in Diamantstempel- und ähnlichen Hochdruckzellen im Vergleich zu früheren experimentellen Versuchsanordnungen durch Verwendung von Mikrospulen um mehrere Größenordnungen verbessert werden kann. Im zweiten Teil der Arbeit wird mit dieser experimentellen Versuchsanordnung die Druckabhängigkeit elektronischer Eigenschaften von metallischem Aluminium bis 101 kbar untersucht. Im dritten und letzten Teil der Arbeit wird die Versuchsanordnung zur Untersuchung des Hochtemperatursupraleiters $YBa_2Cu_4O_8$ bei Drücken bis zu 63 kbar verwendet.